

ELECTRONIC THERMAL CONDUCTIVITY MEASUREMENTS IN GRAPHENE

SERAP YİĞEN

A THESIS
IN
THE DEPARTMENT
OF
PHYSICS

PRESENTED IN PARTIAL FULFILLMENT OF THE REQUIREMENTS
FOR THE DEGREE OF DOCTOR OF PHILOSOPHY
CONCORDIA UNIVERSITY
MONTRÉAL, QUÉBEC, CANADA

JANUARY 2015

© SERAP YİĞEN, 2015

CONCORDIA UNIVERSITY
School of Graduate Studies

This is to certify that the thesis prepared

By: **Ms. Serap Yiğen**

Entitled: **Electronic Thermal Conductivity Measurements in Graphene**

and submitted in partial fulfillment of the requirements for the degree of

Doctor of Philosophy (Physics)

complies with the regulations of the University and meets the accepted standards with respect to originality and quality.

Signed by the final examining committee:

Dr. Xavier Ottenwaelder _____ Chair

Dr. Thomas Szkopek _____ External Examiner

Dr. Christine DeWolf _____ External to Program

Dr. Truong Vo-Van _____ Examiner

Dr. Valter Zazubovits _____ Examiner

Dr. Alexandre Champagne _____ Thesis Supervisor

Approved _____
Chair of Department or Graduate Program Director

_____ 20 _____
Dean of Faculty

Abstract

Electronic Thermal Conductivity Measurements in Graphene

Serap Yiğen, Ph.D.

Concordia University, 2015

The electronic thermal conductivity in graphene describes how energy is transported by the charge carriers in graphene, and how these carriers lose their energy via diffusion and interactions with phonons and impurities. Understanding these interactions can shed light on electron-phonon scatterings, thermal relaxation processes, and the electron cooling mechanisms in graphene. We developed a method to experimentally isolate the electronic thermal conductivity in suspended graphene transistors by adapting a Joule self-heating method. We extracted the electronic thermal conductivity, K_e , as a function of electron temperature and charge carrier density.

We fabricated two-point suspended graphene transistors using micro-fabrication methods. We used the electrical contacts as source and drain to apply a bias voltage and a back-gate electrode to tune the carrier density. We adapted a Joule self-heating method in which we used graphene as its own heater and thermometer. To do so, we prepared thermometry (calibration) curves by measuring low-bias resistance of the graphene devices versus temperature. As we increased the bias voltage, we could measure and control the temperature of electrons. We solved a one-dimensional heat diffusion equation and extracted the electronic thermal conductivity. We studied our samples at low bias voltages and intermediate temperatures where the electron and lattice temperatures are decoupled. This minimized the energy transfer between phonons and charge carriers. Since the suspended devices isolate the graphene crystals from the substrate, there were no interactions with the substrate phonons and no heat leakage to the substrate. Therefore, the heat was diffused only by the charge carriers.

We extracted the electronic thermal conductivity in intrinsic monolayer graphene over a temperature range of 20 to 300 K. We found that K_e has a strong temperature dependence, ranging from 0.5 to 11 W/m.K. We compared our data with a model of diffusing charged quasiparticles which have the same mean free path and velocity as graphene's charge carriers. Data from three different devices are in very good agreement with the model, supporting that the heat is carried by diffusing Dirac quasiparticles.

We doped our devices using the back-gate electrode, and extracted K_e in doped graphene over a temperature range of 50 to 160 K. We found that K_e is proportional to the charge conductivity times the temperature, and thus the Wiedemann-Franz Law is obeyed in suspended graphene. The Lorenz coefficient is estimated to be 1.1 to $1.7 \times 10^{-8} \text{ W } \Omega \text{ K}^{-2}$. We observed a strong thermal transistor effect in our devices as the charge carrier density is changed from ≈ 0.5 to $1.8 \times 10^{11} \text{ cm}^{-2}$, showing that K_e can be tuned by more than a factor of 2 by applying a few volts of gate voltage.

The methods presented here could be extended to bilayer graphene devices and other two-dimensional materials to isolate K_e to study electron-electron and electron-phonon interactions. The ability to control K_e could be useful for energy harvesting in nano and opto-electronic devices.

Acknowledgments

I would like to take this opportunity to acknowledge those who encouraged, inspired and assisted me throughout my PhD. First and foremost, I would like to express my deepest gratitude to my supervisor, Dr. Alexandre Champagne, for his guidance, support and patience. His love and enthusiasm for science inspired me and will be inspiring many more young scientists. Thanks for being a good mentor to me. I believe that I have learned a lot from you.

This work would not be possible without talented and fun colleagues around. Vahid, Joshua, Andrew, Jimi and Marc, thanks for being such amazing teammates and friends. Seeing your smiley faces and hearing your funny jokes turned even the most frustrating days in the lab into cheerful memories. I really appreciate all the support and help you provided whenever I needed. It was a great pleasure to work with you guys.

I would like to give my appreciation to microfabrication facilities at École Polytechnique de Montréal, McGill University and Université de Sherbrooke and their staff members for providing technical help and supports.

My special thanks go to Dr. Barry Frank and his wife Donnie Frank for opening their home to me and making me feel like part of their family, while I was trying to adapt to a new country. I will always be grateful for that. I would like to extend my sincere thanks and appreciation to Dr. Mariana Frank for her support and help with my arrival in Canada. I am grateful to my committee members for their helpful comments and discussions.

Last, but not the least, I would like to say a heartfelt thank to my parents for their constant support and endless love. I am grateful to you for always believing in me and I extremely appreciate your care and encouragements. I am also thankful to all my friends in Canada who have been very helpful in numerous ways and always a great boost and fun in my life.

Contents

List of Figures	ix
List of Tables	xi
1 Introduction: Graphene	1
1.1 Graphene Electronics	4
1.1.1 Electronic band structure	5
1.1.2 Density of states of charge carriers	9
1.2 Electronic Thermal Transport in Graphene	13
2 Fabrication of Suspended Graphene Transistors	17
2.1 Deposition and Characterization of Graphene Crystals	19
2.1.1 Etching the back-side oxide of wafers	19
2.1.2 Patterning of coordinate grids via photolithography	21
2.1.3 Metal deposition of coordinate grids	23
2.1.4 Mechanical exfoliation of graphene crystals	26
2.1.5 Verification of the number of atomic planes in the crystals . .	26
2.2 Making Electrical Contacts on Graphene	32
2.2.1 Patterning contacts via electron-beam lithography	32
2.2.2 Metal deposition of contacts	33
2.3 Suspension of Graphene	35
2.3.1 Wet-etching	35
2.3.2 Ellipsometry and reflectometry	36
2.3.3 Scanning electron and atomic force microscopy imaging of devices	37
2.4 Measurement Set-up and Circuits	38
2.4.1 Testing graphene devices with a probe station	38

2.4.2	Wire-bonding and handling of samples	39
2.4.3	Cooling down to low temperatures	40
2.4.4	Electronic set-up and circuits	41
2.5	Fabrication Results	42
3	Electronic Thermal Conductivity of Monolayer Graphene in Intrinsic Regime	44
3.1	Introduction	45
3.1.1	Upper bond for contact resistance	48
3.2	Electron Thermometry and Joule Heating of Electrons	50
3.2.1	Mean-free path in the nearly intrinsic regime	52
3.2.2	Joule self-heating of electrons	53
3.2.3	Electron-electron scattering length	58
3.3	Extracting Electronic Thermal Conductivity (K_e) in Intrinsic Graphene	60
3.3.1	Error analysis	61
3.4	K_e for Diffusing Dirac Quasiparticles in 2D	63
3.4.1	Electron cooling length estimate	64
3.5	Conclusion and Outlook	65
4	Wiedemann-Franz Relation and Thermal-Transistor Effect in Graphene	66
4.1	Introduction	66
4.1.1	Upper bond for contact resistance	69
4.2	Extracting Electronic Thermal Conductivity (K_e) in Doped Graphene	71
4.3	Theoretical Model: Wiedemann-Franz Law	77
4.3.1	Contact resistance effect on extracted Lorenz numbers	78
4.4	Thermal Transistor Effect in Graphene	79
4.5	Conclusion and Outlook	81
5	Conclusion and Ongoing Projects	82
5.1	Conclusion: Electronic Thermal Conductivity in Monolayer Graphene	82
5.2	Ongoing Projects: Bilayer Graphene	86
5.2.1	Electronic band structure	87
5.2.2	Suspended bilayer graphene FETs	91
5.2.3	Electronic thermal conductivity in bilayer graphene	96

5.3	Contributions to Other Projects	98
5.3.1	Ultra-short suspended single-wall carbon nanotube transistors	98
5.3.2	Tailoring 10 nm scale suspended graphene junctions and quantum dots	99
	Bibliography	101

List of Figures

1.1	SEM image of one of our two-point suspended graphene transistors	3
1.2	The hexagonal lattice of graphene.	6
1.3	Electronic dispersion of graphene	10
1.4	Diagram of conductance (G) versus gate voltage (V_G) for a graphene transistor	12
1.5	Cartoon of a device design to study thermal conductivity in graphene using a traditional heat transport measurement	14
2.1	Cartoon of a suspended graphene transistor	18
2.2	Etching of the back-side of wafers	20
2.3	Mask pattern for coordinate grids	22
2.4	Cartoon of the photolithography procedure	24
2.5	Thin film deposition of metals	25
2.6	Mechanical exfoliation of graphene crystals	27
2.7	Optical images of graphene crystals	28
2.8	Raman spectroscopy of graphene	31
2.9	Electron-beam lithography of electrical contacts	33
2.10	Metal transfer of contacts	34
2.11	SEM images of devices after BOE etching	36
2.12	Picture of an ellipsometer	37
2.13	AFM imaging of suspended graphene transistors	38
2.14	Image of our probe station	39
2.15	Wire-bonding of the samples	40
2.16	Variable temperature cryostat (VTI)	41
2.17	Electrical circuit for dc measurements	42
2.18	Suspended monolayer graphene transistor	43
3.1	SEM images of suspended graphene transistor and R vs V_G graphs	46

3.2	Sample annealing data	47
3.3	Upper bound for contact resistance	49
3.4	Electron thermometry	51
3.5	Relative conductance G/G_{11K} vs T	52
3.6	Electron heating for Sample A	55
3.7	Electron heating for Sample B	56
3.8	Electron heating for Sample C	57
3.9	Mesoscopic conductance oscillation in Sample B	59
3.10	K_e vs T_e data for Sample A, B and C	62
4.1	SEM images of suspended and annealed graphene devices	68
4.2	Electron thermometry and electron Joule heating in doped graphene.	72
4.3	Electron heating in Sample C	74
4.4	Wiedemann-Franz (WF) law	76
4.5	Contact resistance effect on extracted Lorenz numbers	79
4.6	Electronic thermal conductivity transistor effect.	80
5.1	Summary of K_e in intrinsic graphene	84
5.2	Summary of K_e in doped graphene	85
5.3	Crystal structure of bilayer graphene	88
5.4	The low-energy electronic band structure of bilayer graphene	90
5.5	Optical images of monolayer, bilayer and trilayer graphene	92
5.6	Raman spectroscopy of single layer, bilayer and trilayer graphene	93
5.7	Integrated intensities of Raman peaks of single and few layers graphene.	94
5.8	Optical images of the bilayer graphene samples	95
5.9	Expected P_{e-ph} in bilayer graphene versus electronic temperature T_e	97
5.10	Ultra-short suspended single-wall carbon nanotube transistors	99
5.11	Tailoring 10 nm scale suspended graphene junctions and quantum dots	100

List of Tables

5.1	Comparison of G/2D intensity ratios for our single-layer, bilayer and trilayer graphene devices	94
-----	---	----

List of Abbreviations

Abbreviation	Meaning
2D	two-dimensional
2DEG	two-dimensional electron gas
FET	Field-effect transistor
CNP	Charge neutrality point
DOS	Density of states
SEM	Scanning electron microscope
UV	Ultra violet
FWHM	Full width half maximum
PMMA	Polymethyl methacrylate
MIBK	Methyl isobutyl ketone
IPA	Isopropyl alcohol
EBL	Electron beam lithography
RIE	Reactive ion etching
RF	Radio frequency
BOE	Buffered oxide etch
CPD	Critical point drying
AFM	Atomic force microscope
VTI	Variable temperature cryostat
LHe	Liquid helium
DAQ	Data acquisition system
GUI	Graphical user interface
HWHM	Half width half maximum
WF	Wiedemann-Franz law
QHE	Quantum Hall effect
SWCNT	Single-wall carbon nanotube
QD	Quantum dot

Chapter 1

Introduction: Graphene

Graphene, a two-dimensional (2D) crystal made up of carbon atoms, has attracted tremendous attention owing to its exceptional electronic quality, mechanical strength and transparent optical nature. Graphene was previously assumed not to be stable in nature until 2004, when two scientists produced single-layer graphene by using a simple micro-cleaving method [1]. The isolation of single-layer graphene was a groundbreaking discovery which opened up opportunities to explore relativistic-like electrons in simple bench-top experiments, and develop real world applications in electronics [2,3] and opto-electronics [4–6].

Thermal transport in graphene has been studied extensively [7–12], since heat transport studies serve as a powerful tool to explore electronic and phononic properties of materials as well as their interactions. It was shown that graphene’s thermal conductivity can reach extremely high values in suspended devices and that heat is mostly carried by phonons [7,11,13]. Due to this phonon-dominated heat conductivity in graphene, it has been challenging to isolate and measure the electronic thermal conductivity. In this thesis we report some of the first experimental measurements of the electronic thermal conductivity in suspended graphene [14,15]

Understanding the electronic thermal conductivity, K_e , is key to assess the amount of heat carried by the charge carriers in graphene (electrons and holes). It can also identify the main cooling mechanisms through which hot electrons cool down as they diffuse through the crystal. This understanding is essential to optimize devices such as photoelectric cell designed to harvest solar energy and turn it into electrical currents [16–18]. This can be useful to explain the interactions of charge carriers

with themselves, with phonons, and with impurities in the crystal. Furthermore, understanding and controlling the energy carried by the charge carriers in materials can be helpful for the thermal management of highly doped nano scale devices. In this chapter, we will briefly review the electronic and thermal properties of graphene to give a background for the work presented in this thesis. We will derive the linear low-energy band structure of graphene and discuss its effect on the charge carriers and the density of states. We will also explain how we can tune the carrier density in graphene via electrical gating. Lastly, we will discuss the thermal properties of graphene.

In this thesis, we report the development of a method to isolate the electronic thermal conductivity in suspended graphene [14, 15]. We fabricated two-point suspended graphene devices. A scanning electron microscope (SEM) image of one of our devices is shown in Fig. 1.1. The electrical contacts serve as source and drain, as well as mechanical anchors. The back-gate electrode (substrate) is used to apply a gate voltage and tune the carrier density in the suspended channel. The suspension of graphene decouples the crystal from the substrate, preventing interactions with the substrate disorder. In addition, it allows for effective Joule self-heating annealing which results in high-mobility devices. Decoupling of the crystal from the substrate is also particularly important for heat transport studies, since any heat leakage to the substrate can greatly complicate the measurements. For instance, in one set of experiments, it has been shown that 77% of the heat is dissipated through the substrate (300 nm SiO₂ on Si) directly below the graphene channel rather than carried along the graphene to the metallic contacts [19].

To extract the electronic thermal conductivity of graphene, we adopt a self-heating method in which a bias voltage is applied to the electrical contacts creating Joule heating effect in the graphene channel. Joule self-heating has been previously applied to carbon nanotubes [20–22] and proved to be a successful method to study thermal transport. Joule heating (or Ohmic heating) generates heat in the material proportionally to the material’s resistance and the current flowing through it;

$$P = RI^2 \tag{1.1}$$

We first use Joule self-heating to anneal our samples. We flow high current through the source and drain contacts which heats up the graphene channel. The elevated

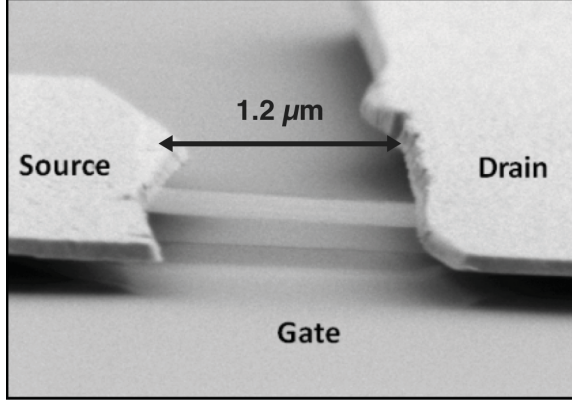


Figure 1.1: Scanning electron microscope image of one of our two-point suspended graphene transistors. The electrical contacts are used as mechanical anchors as well as to apply a bias voltage. The Si substrate is used as a back gate electrode to tune the charge carrier density in the channel. The graphene flake is suspended and completely decoupled from the substrate.

temperature expels any chemical residues from the micro-fabrication process. The annealing removes external dopants from the graphene crystal and thus reduces the interactions between the charge carriers and impurities. Annealing the samples is a critical step to minimize the energy transfer (heat loss) from hot electrons to impurities and also to phonons since impurities can mediate energy transfer from charge carriers to phonons via so called supercollison [23].

We then measured the two-point resistance of our devices at different temperatures. We used very low bias (± 1 mV) to avoid any Joule Heating effect so that the resistance is obtained exactly at the temperature of measurement. The resistance (R) versus temperature (T) dependence in our devices was well-behaved (i.e. monotonic) in the intermediate temperature range, from 20 K up to 300 K, proving that graphene's resistance can serve as an accurate secondary thermometer for electron temperature with an accuracy better than 1 K. The R vs T (calibration) curves are then used to determine the temperature of electrons from the measured resistance.

We applied higher bias voltages to heat up the graphene's charge carriers above the cryostat's (and electrical contacts') temperature. This created a temperature bias, ΔT , between the center of the graphene channel and the electronic contacts. We studied our samples at low bias and at intermediate temperatures where the

electron-phonon energy transfer is very low [16, 17, 24, 25]. We made use of this decoupling between the temperature of electrons and phonons to be able to isolate the electronic thermal conductivity. Thus, hot electrons could thermalize only through charge carriers and the heat was mainly carried by the charge carriers. To extract the electronic thermal conductivity, we solved a one-dimensional heat diffusion equation as:

$$K_e = \frac{Q L^2}{12 \Delta T} \quad (1.2)$$

where $Q = RI^2/WLh$ is the Joule heating power per unit volume, W the width, L the length, and $h = 0.335$ nm the thickness of the graphene channel.

1.1 Graphene Electronics

Graphene is being the first two-dimensional crystal that is transparent, flexible yet strong and an excellent conductor of electricity and heat, no wonder its popularity spread out so quickly across the scientific and engineering community. Graphene has a unique electronic band structure with a linear energy dispersion at low-energy, which allows its charge carriers to behave like relativistic particles. These charge carriers can reach extremely high mobilities. This section will introduce the basic concepts to understand the electronic properties of graphene.

Graphene is a monolayer of graphite, a two-atom basis hexagonal lattice of carbon atoms. A carbon atom has six electrons which occupy the orbitals $1s^2 2s^2 2p^2$. The two electrons in the inner shell ($1s$) remain inert and the four electrons in the outer shells ($2s$ and $2p$) are available for chemical bonding. In graphene, each carbon atom is connected to three adjacent carbon atoms on the two-dimensional plane with σ bonds, leaving one $2p_z$ electron freely available. These highly-mobile fourth electrons on the outer shell occupy a π -orbital and thus are called π electrons. These π orbitals overlap with the adjacent π orbitals, forming a band which allows easy movement of electrons across the plane of graphene. This is why graphene can have a high electrical conductivity. This type of hybridization of orbitals is called sp^2 hybridization in which the sp^2 orbitals are arranged in a hexagonal (honeycomb) lattice structure and form strong three σ -bonds with the neighboring carbon atoms [26–28]. The π orbitals projecting from the plane of graphene give rise to valance and conduction bands and

unique electronic properties of graphene.

In this section, we will review some basic electronic properties of graphene in order to understand the work presented in this thesis. First we will start by deriving the energy band structure of graphene and find the low energy dispersion of charge carriers. Then we will show how to calculate the density of available states for electrons as a function of energy. We will also explain how we can tune the number of charge carriers in graphene by applying a gate voltage and calculate the carrier density in our samples.

1.1.1 Electronic band structure

In this subsection, we will derive the electronic band structure of graphene using the tight-binding model [29, 30]. This will allow us to understand how the energy of the charge carriers changes with their momentum and how the density of states changes with energy. Fig. 1.2 shows the honeycomb lattice structure of graphene which can be thought as a triangular lattice with a basis of two atoms (sublattice-A and sublattice-B are shown in black and red respectively in Fig. 1.2) per unit cell with the following primitive lattice vectors,

$$\vec{a}_1 = \frac{a}{2}(3, \sqrt{3}) \quad \vec{a}_2 = \frac{a}{2}(3, -\sqrt{3}) \quad (1.3)$$

where a is the spacing between the nearest carbon atoms ($\approx 1.42 \text{ \AA}$). The reciprocal lattice vectors which are useful to map the electronic band structure of graphene can be derived from the relation $a_i \cdot b_j = 2\pi\delta_{ij}$ as

$$\vec{b}_1 = \frac{2\pi}{3a}(1, \sqrt{3}) \quad \vec{b}_2 = \frac{2\pi}{3a}(1, -\sqrt{3}) \quad (1.4)$$

The three nearest-neighbor vectors in real space are given by,

$$\vec{\delta}_1 = \frac{a}{2}(1, \sqrt{3}) \quad \vec{\delta}_2 = \frac{a}{2}(1, -\sqrt{3}) \quad \vec{\delta}_3 = a(-1, 0) \quad (1.5)$$

We can start by defining Bloch functions for a crystal with N unit cell for the M^{th} atomic orbitals,

$$\Phi_m(\mathbf{k}, \mathbf{r}) = \frac{1}{\sqrt{N}} \sum_{i=1}^N e^{i\mathbf{k} \cdot \mathbf{R}_{m,i}} \phi_m(\mathbf{r} - \mathbf{R}_{m,i}) \quad (1.6)$$

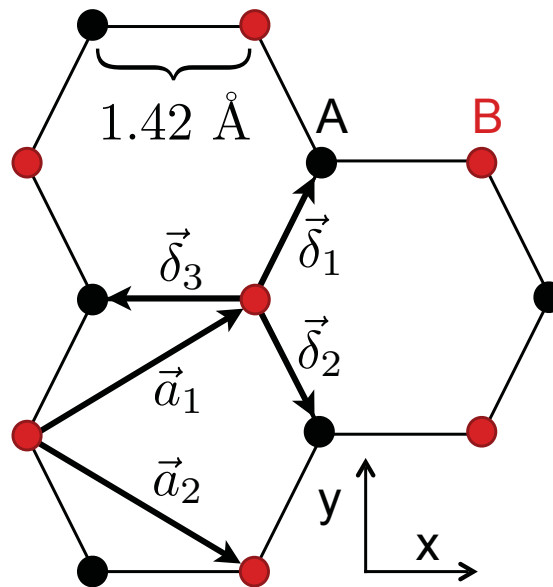


Figure 1.2: The hexagonal lattice of graphene with the lattice unit vectors, \vec{a}_1 and \vec{a}_2 . Black and red colors indicate the two triangular sublattices, labeled as A and B. The nearest-neighbour vectors $\vec{\delta}_1$, $\vec{\delta}_2$ and $\vec{\delta}_3$ connect the atoms in sublattices.

where $\mathbf{R}_{m,i}$ is the position vector of the m th orbital in the i th unit cell. Then the electronic wave function can be expressed as a superposition of Bloch functions,

$$\Psi_j(\mathbf{k}, \mathbf{r}) = \sum_{m=1}^M c_{j,m}(\mathbf{k}) \Phi_m(\mathbf{k}, \mathbf{r}) \quad (1.7)$$

The transfer integral matrix, H_m , can be formed by finding the matrix elements $H_{mm'} = \langle \Phi_m | \mathcal{H} | \Phi_{m'} \rangle$ where \mathcal{H} is the Hamiltonian. Therefore the diagonal matrix elements for graphene can be written as [29]

$$H_{AA} \approx \frac{1}{N} \sum_{i=1}^N \langle \phi_A(\mathbf{r} - \mathbf{R}_{A,i}) | \mathcal{H} | \phi_A(\mathbf{r} - \mathbf{R}_{A,i}) \rangle \quad (1.8)$$

and the off-diagonal matrix element, considering the hopping of the electrons from sublattice- A to its three nearest-neighbor B atoms, will be

$$H_{AB} \approx \frac{1}{N} \sum_{i=1}^N \sum_{l=1}^3 e^{i\mathbf{k} \cdot \delta_l} \times \langle \phi_A(\mathbf{r} - \mathbf{R}_{A,i}) | \mathcal{H} | \phi_B(\mathbf{r} - \mathbf{R}_{B,l}) \rangle \quad (1.9)$$

where $\delta_l = \mathbf{R}_{B,l} - \mathbf{R}_{A,i}$. If $\gamma_0 = -\langle \phi_A(\mathbf{r} - \mathbf{R}_{A,i}) | \mathcal{H} | \phi_B(\mathbf{r} - \mathbf{R}_{B,l}) \rangle$ is defined as a hopping parameter, the off-diagonal matrix element will reduce to

$$H_{AB} \approx -\gamma_0 f(\mathbf{k}) \quad f(\mathbf{k}) = \sum_{l=1}^3 e^{i\mathbf{k} \cdot \delta_l} \quad (1.10)$$

where $f(\mathbf{k})$ is a function which describes nearest-neighbour hopping and its conjugate gives the other off-diagonal matrix element, $H_{BA} = H_{AB}^* = -\gamma_0 f^*(\mathbf{k})$. Solving the eigenvalue equation, $H_m \Psi_j = E \Psi_j$:

$$\begin{pmatrix} 0 & -\gamma_0 f(\mathbf{k}) \\ -\gamma_0 f^*(\mathbf{k}) & 0 \end{pmatrix} \Psi_j = E(\mathbf{k}) \Psi_j \quad (1.11)$$

the eigenvalues can be found as

$$E(\mathbf{k}) = \pm \gamma_0 f(\mathbf{k}) \quad (1.12)$$

The function $f(\mathbf{k})$ can be calculated by using the primitive lattice and nearest-neighbor vectors (Eq. 1.3 - 1.5). Then, the function can be written in the explicit form [30];

$$f(\mathbf{k}) = 2 \cos(\sqrt{3}k_y a) + 4 \cos\left(\frac{\sqrt{3}}{2}k_y a\right) \cos\left(\frac{3}{2}k_x a\right) \quad (1.13)$$

When the energy dispersion $E(\mathbf{k})$ (Eq. 1.12) is plotted, it looks like in Fig. 1.3 (adapted from Ref. [30]). The energy goes to zero at six points which are the corners of Brillouin zone. The two manifolds, $+\gamma_0 f(\mathbf{k})$ and $-\gamma_0 f(\mathbf{k})$, touch each other at these points. The "+" sign refers to upper band (π^*) and the "-" sign refers to lower band (π). The vertices of Brillouin zone are divided into two inequivalent sets of three points which are labeled as K and K' (see Fig. 1.3). These points are located at [30]

$$K = \left(\frac{2\pi}{3a}, \frac{2\pi}{3\sqrt{3}a}\right) \quad , \quad K' = \left(\frac{2\pi}{3a}, -\frac{2\pi}{3\sqrt{3}a}\right) \quad (1.14)$$

and are called charge neutrality points (CNP) or Dirac Points for a reason that will be clear soon. The Dirac points are especially important for low-energy electronic properties, as the Fermi level resides at these points and the energy bands are symmetric about the point $E = 0$. When the energy band is half-filled, the density of states at the Fermi-level is exactly zero. This means that undoped graphene is a perfect semimetal. This will be further discussed in the following section.

The inset of Fig. 1.3 shows an enlarged portion of the spectrum around the CNP. The low-energy spectrum at the CNP is linear, not quadratically as in conventional semiconductors. This is already a very interesting feature, since we know that the energy of free electrons changes quadratically with their momentum. It can be clearly seen that the low-energy excitations in graphene will behave differently from free electrons.

To support this statement, we need to find a dispersion that is valid around K and K' points. We can derive an effective low-energy Hamiltonian by expanding the function $f(\mathbf{k})$ in the vicinity of CNP. By using the first two terms in the Taylor series expansion of $f(\mathbf{K} + \mathbf{k})$, we can approximate the Hamiltonian as

$$H_{eff}^K = v_F \begin{pmatrix} 0 & k_x - ik_y \\ k_x + ik_y & 0 \end{pmatrix} \quad (1.15)$$

which can be simplified to the following form

$$H_{eff}^K = v_F \boldsymbol{\sigma} \cdot \mathbf{p} \quad (1.16)$$

where v_F is the Fermi velocity and $\boldsymbol{\sigma}$ are the Pauli matrices. This is called Dirac-Weyl equation which is a usual Dirac equation in the limit of zero mass ($m \rightarrow 0$). The eigenvalues clearly show that at very low energy (near K and K'), the energy of charge carriers is linear as a function of momentum;

$$E_{\pm}(k) = \pm \hbar v_F |k| \quad (1.17)$$

The (+) and (-) signs refer to the conduction and valence bands respectively. This energy dispersion was first derived by Wallace [31–33]. The Fermi velocity of charge carriers in graphene is $v_F = c/300 = 10^6$ m/s and the k is their momentum. At the point, $k = 0$, the conduction and valence band meet at the Dirac point, and thus there is no energy gap between them [34]. The low-energy excitations in graphene mimic relativistic particles; they are governed by a Dirac-like equation, can travel with $1/300^{th}$ of the speed of light and carry zero effective mass. Therefore, these relativistic quasiparticles are called massless Dirac fermions.

1.1.2 Density of states of charge carriers

The charge carriers, Dirac fermions, in graphene behave differently than charge carriers in conventional two-dimensional (2D) semiconductors. The energy of charged quasiparticles in regular two-dimensional electron gas (2DEG) changes quadratically with momentum. Thus, they are described by the Schrödinger equation. However, graphene's charge carriers have a linear dispersion and obey Dirac's equation. In this section, we will review the distinct electronic properties of graphene's charge carriers arising from the Dirac linear dispersion.

One of the consequences of graphene's unique energy band structure can be seen in the density of states of Dirac fermions. Density of states (DOS) is defined as the number of states available for charged quasiparticles to occupy and is essential for determining the Fermi level position. The density of state for charge carriers in

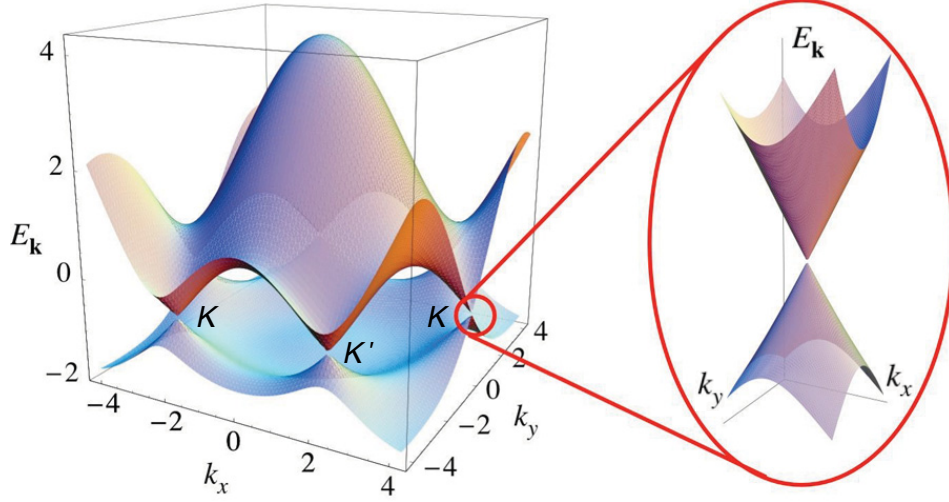


Figure 1.3: Electronic dispersion of graphene [30]. The conduction band and the valence band touch each other at six discrete points. These points are called Dirac points. The zoom shows the low-energy linear dispersion and the cone-shaped valence and conduction bands.

graphene differs from regular 2DEG's and is given by [35]

$$D(E) = \frac{g_s g_v E}{2\pi \hbar^2 v_F^2} \propto E \quad (1.18)$$

where $g_s = 2$ and $g_v = 2$, being spin and valley degeneracy respectively, and $v_F = 10^6$ m/s is the Fermi velocity. The DOS changes linearly with energy and at zero energy, Dirac point, the DOS is zero. On the other hand, the DOS of charge carriers in a conventional 2D semiconductor (or 2DEG) is given by [35, 36]:

$$D(E) = \frac{g_s g_v m^*}{2\pi \hbar^2} \propto \text{constant} \quad (1.19)$$

where $g_s = 2$ and $g_v = 1$ for 2DEG, and m^* is the effective mass of the charge carriers. Density of states for a 2DEG is constant and does not change with energy. The difference between the DOS in graphene and 2DEG affects the electronic transport properties. For example, the screening of electrons depends on the DOS. In monolayer graphene, the screened and unscreened Coulomb scatterings are same and do not change with carrier density. However in 2DEG, the effective screening becomes stronger as the carrier density decreases.

The charge carrier density can be tuned by applying a voltage to the back gate electrode. Using a parallel capacitor model, the carrier density per unit area induced by the gate, n_G , can be calculated with the following equation:

$$n_G = \frac{C_G V_G}{e} \quad (1.20)$$

where C_G is the capacitance, V_G is the gate voltage, e is the electron's electric charge. When graphene is undoped, the Fermi level, the highest energy level occupied, resides exactly at the Dirac point (see Fig. 1.4). This implies that the valence band is fully filled and the conduction band is completely empty. This is called intrinsic graphene. By applying an external voltage from a gate electrode or chemical doping, the Fermi can be shifted up or down. Graphene is then doped with electrons or holes. The system can be tuned from being electron-like (n-type) to being hole-like (p-type) [35]. In practice, there is always a small amount a doping due to thermally generated charge carriers or small amounts of surface adsorbate, thus we refer to our annealed samples at low temperature as being in the “nearly” intrinsic regime.

The charge carrier density is important for determining the mobility of the charge carriers. Mobility is a quantity which describes how easy the charge carriers can move through a crystal under the influence of an electric field. Mobility is controlled by the electron scattering processes in the crystal. These scatterings are caused by charged and neutral impurities, defects, and phonons in the crystal. Hence, the mobility can give hints about the scattering processes in the system. The mobility of charge carriers can be found from the measured electrical conductivity (σ) and the total charge carrier density (n),

$$\mu = \frac{\sigma}{ne} \quad (1.21)$$

The mobility of graphene samples on a SiO₂ substrate was measured up to be 15,000 cm²/V.s, but often much lower [37–39]. Mobility was then improved by making suspended samples eliminating impurity scattering from the substrate. Measurements on suspended samples reported that the mobility can reach up to 200,000 cm²/V.s [40, 41]. Recent experiments showed that on cleaner suspended samples, a mobility of 1,000,000 cm²/V.s [42] can be achieved.

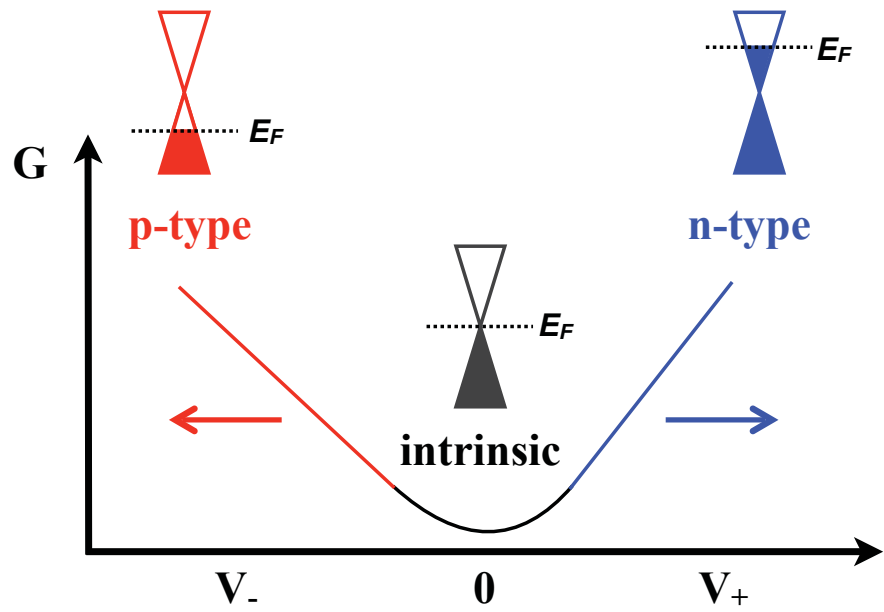


Figure 1.4: Diagram of conductance (G) versus gate voltage (V_G) for a graphene transistor. When graphene is undoped, the Fermi level resides exactly at the Dirac point. This is called the intrinsic regime. A gate voltage shifts the Fermi level down or up, doping graphene with holes (p-type) or electrons (n-type) respectively.

1.2 Electronic Thermal Transport in Graphene

In solids, heat is carried by phonons and electrons, thus the thermal conductivity is defined as $K = K_{ph} + K_e$, where K_e and K_{ph} are the electron and phonon contributions respectively. In metals, K is dominated by electrons and the K_e contribution is given by Wiedemann-Franz Law [43], $K_e = \sigma L T_e$, where σ is the electrical conductivity, T_e is the electronic temperature and L is the Lorenz number. However in carbon materials, including graphite, K is usually dominated by phonons [44]. It was shown that heat is mainly carried by phonons in graphene and the phononic thermal conductivity of graphene can reach extremely high values up to 5300 W/K.m at room temperature [7, 11, 13]. Because of the phonon-dominated thermal transport, it has been challenging to isolate K_e in graphene. There have been experimental reports of K_e in disordered graphene at very low temperatures [45, 46]. However, a detailed mapping of electronic thermal conductivity of graphene is still lacking.

Graphene has 6 phonon modes; 3 acoustic and 3 optical modes [47]. Longitudinal and transverse acoustic modes (LA and TA) have linear dispersion relations $\omega \propto k$ and are the in-plane translation and stretching modes. Since graphene is a 2-dimensional material sitting in 3-dimensional space, it can vibrate out of the plane as well, allowing for out-of-plane phonons (flexural mode, ZA). The acoustic flexural mode's energy disperses quadratically with momentum $\omega \propto k^2$. The remaining 3 branches correspond to optical modes: one out-of-plane mode (ZO) and two in-plane modes (TO) and (LO). The acoustic phonons serve as the main heat carriers in graphene, whereas the optical phonons are detected in the Raman measurements to determine the number of graphene layers.

Non-contact optical measurement is a useful technique to study thermal transport. A laser is shined on a graphene flake to heat up the crystal and the Raman spectrum is used as a thermometer to detect the change in the temperature from the shift of spectrum. The high phonon thermal conductivity of graphene has been extensively studied using Raman spectroscopy and proved to be dominated by phonons [7–11, 48–51]. Even though Raman spectroscopy provides the measurement of heat transport, it has no control over the charge carrier density, as the heat can thermally populate the charge carriers in the system, mobility etc..

Direct-contact measurements can also be used to study heat transport. The traditional way to measure thermal conductivity of a material using a micro-fabricated

device is shown in Fig. 1.5. Thin wire-contacts are made at each end of the material which serve as a solid-state heater and thermometer [52]. A large current is flowed in the heater so that the wire heats up the crystal underneath and the temperature at each end is detected from the resistance of the wires. Thermal transport measurements have been done on graphene [12, 53–56] using similar micro-fabricated devices shown in Fig. 1.5 and the total thermal conductivity was measured. However, there have been no reports of electronic contributions of thermal conductivity in graphene, as it is difficult to distinguish the temperature of electrons and phonons in the system and thus isolate the electronic thermal conductivity independently from phononic one. Furthermore, the geometry and the size of these type of devices are quite challenging to fabricate with the current nano fabrication methods. The size of graphene crystal needed for this device design would be too large to suspend it over the substrate and building the device on a substrate would cause heat leakage to the substrate.

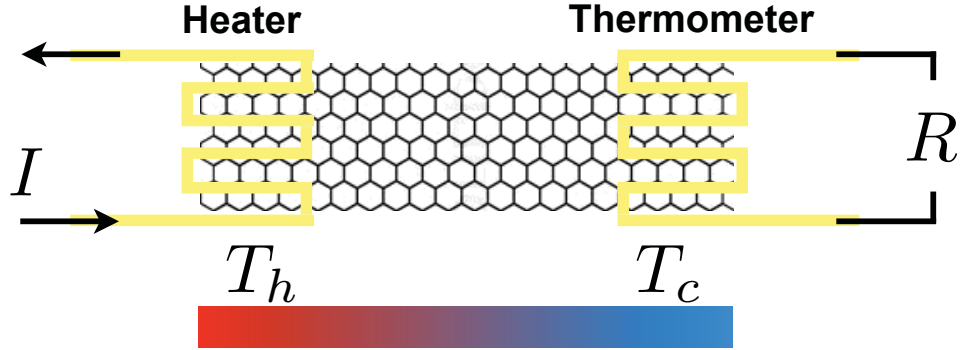


Figure 1.5: Cartoon of a device design to study thermal conductivity in graphene using a traditional heat transport measurement. The two micro-fabricated thin wires at each end of the graphene flake are used as a heater and a thermometer. A high current is flowed in the heater which heats up the crystal underneath and the temperature at each end is detected from the resistance of the wires.

In this work, we present a method to isolate the electronic thermal conductivity which makes use of a decoupling between the temperature of electrons and phonons. We designed two-point suspended graphene devices which are less challenging to fabricate, since the electrical contacts on graphene are simple large geometrical patterns. The thick and large contacts at each end of graphene channel serve as

sturdy anchors, allowing the suspension of the graphene flake above the substrate. The suspended graphene devices prevented any heat leakage to the substrate and allowed for better annealing. The Si substrate was used as a back gate electrode, thus we could control and tune the carrier density in the system. We adopted Joule self-heating method in which a current is flowed through source and drain contacts which heats up graphene channel due to graphene's resistance. We used graphene's resistance both as a heater and thermometer. We studied our samples at low bias and intermediate temperatures so that the energy transfer between charge carriers and phonons was negligible. This ensured that electrons rarely scatter with phonons, thus charge carriers do not transfer their energy to the phonons and heat is only carried by electrons. Therefore, the temperature of electrons (T_e) is decoupled from the temperature of phonons. We solved a one dimensional heat equation to extract the electronic thermal conductivity in our devices.

We studied our samples in the nearly intrinsic regime where the Fermi level resides close to the Dirac Point. We extracted K_e in the quasi-intrinsic regime, $n_{tot,T=0} \approx 1.7 - 2.1 \times 10^{10} \text{ cm}^{-2}$, from $T_e = 20 \text{ K}$ to 300 K . We find that K_e shows a strong T_e dependence ranging from 0.5 to 11 W/m.K over the studied temperature range. The data from three different samples are consistent with a model in which heat is carried by quasiparticles with the same mean free path and velocity as graphene's charge carriers. In our devices, we extract a cooling length for hot electrons [57] which ranges from $100 \text{ }\mu\text{m}$ to $10 \text{ }\mu\text{m}$ for $T_e = 20$ to 300 K . Since the electron cooling length is much longer than the length of graphene channels and we kept the bias voltage below the energy of optical phonons, we expect T_e and T to be decoupled in our devices when $V_B \neq 0$, and all of the Joule heat to be carried to the contacts by charge carriers. Our results provide an experimental evidence that the dominant electron cooling mechanism in intrinsic high-mobility ($\mu \approx 3.5 \times 10^4 \text{ cm}^2/\text{V.s}$) sub-micron graphene devices below 300 K is hot-electron diffusion.

In addition, we extracted the electronic thermal conductivity, K_e , in doped graphene. Our data show that the thermal conductivity is proportional to the charge conductivity times the temperature, $K_e \propto \sigma T$, confirming that the Wiedemann-Franz relation is obeyed in suspended graphene. In the temperature range we studied (between 150 K - 200 K), our data clearly show onsets of the electron-phonon coupling as expected from the theoretical calculations [58]. Our measurements were

recently confirmed by other experiments which measured K_e using Johnson noise thermometry [59]. We also report K_e over a broad range of carrier densities. We showed that K_e could be tuned by applying a gate voltage. Even using a modest V_G range, K_e could be changed by a factor of ≥ 2 , showing a very strong thermal-transistor effect in suspended graphene.

In this chapter, we briefly introduced our method and device design to study electronic thermal conductivity. We gave a background for some of the relevant electronic and phononic properties of graphene which is necessary to understand our work in the following chapters. In chapter 2, we will present the details of the fabrication to prepare our suspended graphene devices. In chapter 3 we provide the details of our measurement technique to extract the electronic thermal conductivity in intrinsic graphene. We will present data for electronic thermal conductivity versus temperature and show the strong temperature dependence of K_e . Chapter 4 will present the data for doped graphene. We will discuss how K_e changes with T and the carrier density in the doped graphene. We will show that K_e can be tuned by n and T and verify that the Wiedemann-Franz Law is obeyed in doped graphene at intermediate temperatures. Chapter 5 presents a conclusion and discusses ongoing and future projects.

Chapter 2

Fabrication of Suspended Graphene Transistors

Heat is propagated across a material by phonons, charge carriers and other excitations of the crystal. How easily the energy flows (conductivity) depends on the number of carriers, the interactions between the various energy carriers (mostly phonons and charge carriers), the crystal structure (dispersion relation), and the disorder (impurities). Therefore thermal properties of a disorder free material are key to understand energy carrier interactions. We focus on understanding how heat is diffused by charge carriers in graphene, also referred to as Dirac fermions. To do so, we must fabricate devices which minimize the interactions of charge carriers with phonons and impurities so that we can isolate the component of thermal conductivity due to charged quasiparticles. In our graphene devices, we work at low bias voltages and intermediate temperatures where there are almost no interactions between electrons and phonons [60]. This will be further discussed in Chapters 3 and 4 where we will explain our method to extract electronic thermal conductivity. To carry out these measurements, we designed suspended two-point graphene transistors, as shown in Fig. 2.1. We can anneal these suspended devices in order to remove adsorbed charge impurities on the graphene crystal. Cleaner devices help to reduce the electron-impurity interactions [23]. An additional challenge is to minimize contact resistance. To lower the contact resistance, we maximize the interface area between the electronic contacts and graphene by making several square micron contact areas. Suspended samples will not only enable better annealing of the channel but also prevent any

heat leakage to the substrate by removing any interactions of electrons with substrate phonons. Thus any heat generated within the graphene crystal will only spread in the plane of the graphene crystal.

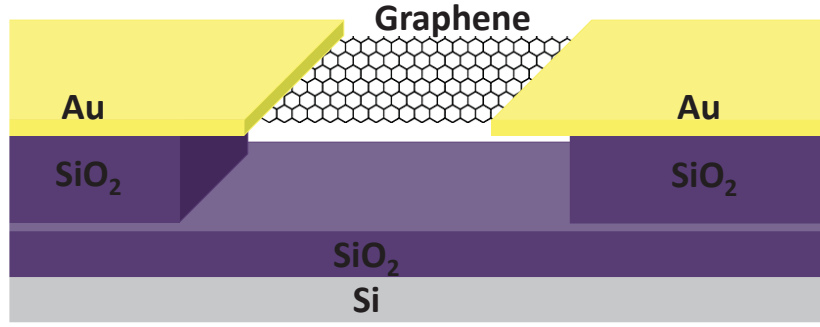


Figure 2.1: Cartoon of a suspended graphene transistor

Our fabrication aim is to make a suspended device like the one depicted in Fig. 2.1. We utilize standard micro fabrication techniques to prepare our samples. Here, we will present the fabrication procedure as well as our dc electron transport measurement setup. The chapter is organized in the same order as the fabrication steps of the samples. We will start by preparing the substrate, a 4" SiO_2 / Si wafer, on which we deposit graphene crystals. To do so, we first define an alignment grid on the wafer using photolithography. This coordinate grid will later allow us to precisely locate graphene flakes. The wafer is then diced into $6 \text{ mm} \times 6 \text{ mm}$ chips. After exfoliating graphene on these chips, an initial inspection is made under an optical microscope. Graphene flakes are sorted out based on their contrasts. The most transparent looking flakes are categorized as monolayer. As their contrast gets darker, they are grouped as bilayer and few-layer graphene. The final measurement of the number of layers is made by looking at their Raman spectra. After verifying the number of layers, we define metal electronic contacts on these graphene flakes using electron-beam lithography. Then, the oxide under the flakes is removed using a wet oxide etch which suspends the graphene channel above the substrate. Suspension of the devices thermally isolates them from the substrate, enabling us to anneal them via Joule heating. In addition, suspension removes substrate disorder. At the end of this chapter, we discuss how

the devices are packaged and handled. We also present our dc transport circuit and explain how the data acquisition is made at low and high temperatures.

2.1 Deposition and Characterization of Graphene Crystals

In this section, we will describe the first steps of our fabrication process. We will start by preparing our substrates and defining a coordinate grid on them via photolithography. We then exfoliate graphene crystals on them, and characterize the flakes using optical and Raman spectroscopy.

2.1.1 Etching the back-side oxide of wafers

We use 4" SiO_2 / Si {100} wafers as substrates. The wafers have 300 nm thick SiO_2 layers thermally grown on both faces. For our devices, the heavily doped Si substrate will serve as a back gate electrode where we can apply a voltage to change the carrier density in our graphene devices. To be able to make electrical contact to the Si, we have to remove the SiO_2 layer on the back of the wafers. We use a dry etching method called Reactive Ion Etching (RIE). In Fig. 2.2(a), a cartoon of the RIE process is shown. A reactive ion etcher has a vacuum chamber in which there are two parallel plate electrodes, one at the bottom and the other on the top. The SiO_2 / Si wafers are placed in this chamber with their back side up. After pumping the chamber, a little bit of gas is introduced and by applying a RF (radio frequency) electromagnetic field, these gas molecules can be ionized to create a plasma. The ions in the plasma are accelerated and strike the wafers to etch the SiO_2 .

Our recipe for SiO_2 etching is as follows. We first clean the chamber with O_2 plasma, with a gas flow of 20 sccm (standard cubic centimetres per minute), RF power of 300 W, and a chamber pressure of 100 mTorr for 15 min. Then we place our wafers in the RIE chamber. We introduce CHF_3 (22.5 sccm) and O_2 (2.5 sccm) gases with RF power of 300 W and chamber pressure of 100 mTorr. We etch for 15 min and then purge the chamber with N_2 gas 3 times before the wafers are taken out. Fig. 2.2(b) shows a picture of the back-sides of two wafers. The back of the first one has not been etched yet and the SiO_2 layer appears as a purple colour. The

back of the second wafer was etched using RIE and the Si surface appears as a silver color. This color difference provides a visual check of the quality of etching. However, further confirmation needs to be done by measuring the thickness of the oxide with an ellipsometer or reflectometer to make sure that the oxide is completely removed.

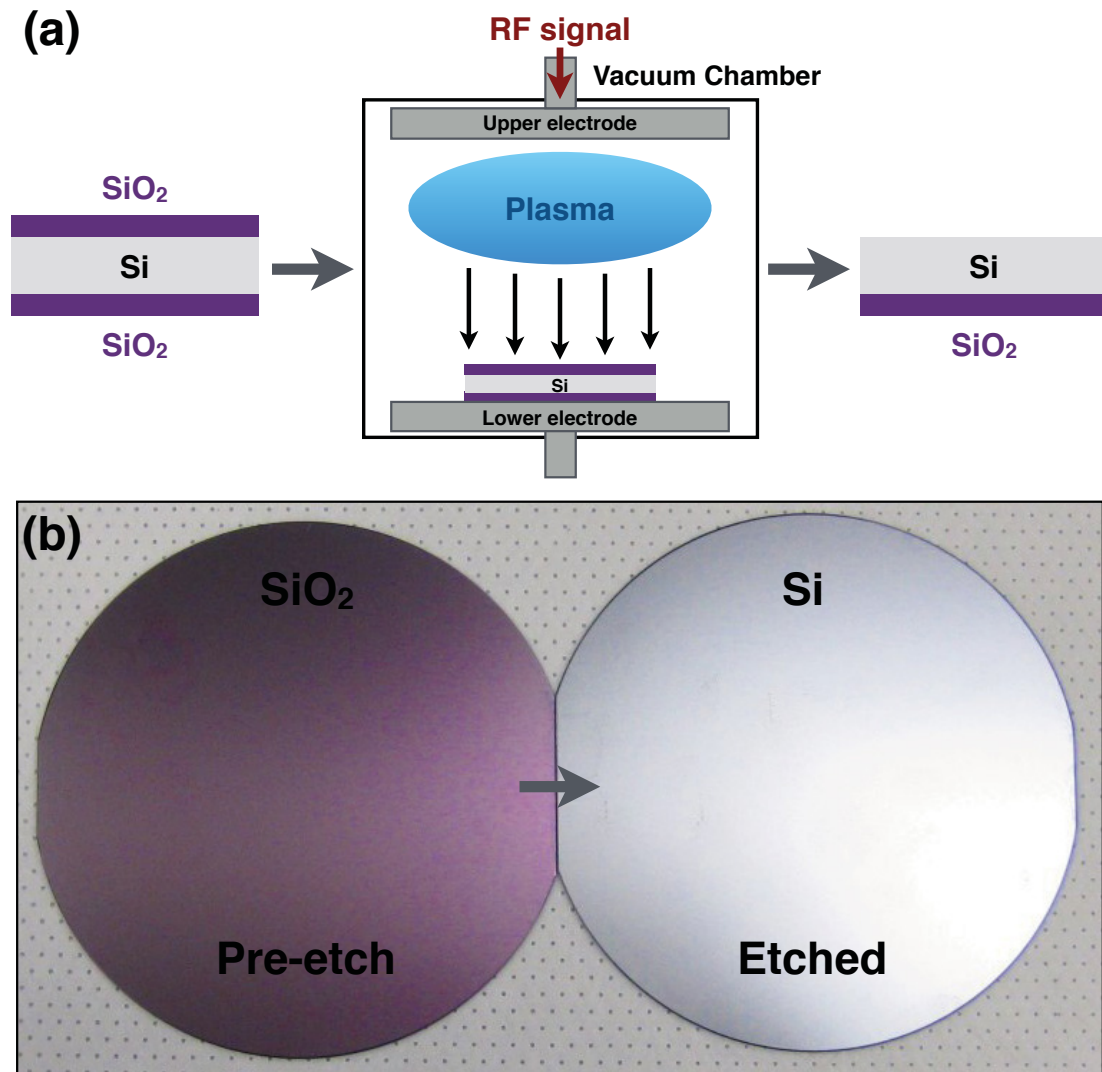


Figure 2.2: Etching SiO₂ from the back-side of wafers. (a) Cartoon of the reactive ion etching process. (b) Images of the back-side of wafers before and after the RIE.

2.1.2 Patterning of coordinate grids via photolithography

After etching the back-side of our wafers, we start preparing the front side where we will fabricate graphene devices. We dice the wafers into 6×6 mm chips and use these chips as substrate for the devices. If graphene is deposited on blank chips, it is very difficult to locate precisely the position of any flake and align electrical contacts on it. For this reason, before dicing our chips, we define a reference coordinate system on them. We designed a grid formed of letters, numbers and L-shaped markers. The alignment grid is $4 \text{ mm} \times 4 \text{ mm}$ in size, starts with A1 on the top left corner. It continues as B1, C1 so on to I1 on horizontal and goes as A2, A3 down to A9 on vertical. Each letter-number symbol is spaced $500 \mu\text{m}$ apart. In between them, we place L-shaped markers each $100 \mu\text{m}$. See Fig. 2.3 for details.

To draw this coordinate grid on the wafers, we use photolithography. Photolithography is a microfabrication process used for transferring micron size shapes on a substrate using UV light. We prepared a photolithography mask containing 15 dies where each die contains a $4 \text{ mm} \times 4 \text{ mm}$ alignment grid. These dies are arranged in a 3×5 matrix on the mask. In Fig. 2.3(a), a cartoon of a wafer with 45 dies is shown. The mask pattern is exposed at least 3 times on a wafer to maximize the number of dies. Fig. 2.3(b) is an optical image on a die where part of the coordinate grid is visible. In Fig. 2.3(c), we zoomed-in on this image to show a closer view of the symbols and the alignment marks.

To do the photolithography, we start with spin coating the substrate with a photoresist (see Fig. 2.4). The exposure to UV light changes the chemical properties of the resist and make it soluble in a developer. We first clean the substrate with acetone and IPA and then spin coat the photoresist, Shipley 1813, at 4000 rpm for 30 seconds which results in a uniform thickness of $1.4 \mu\text{m}$. We soft-bake at 115°C for 60 seconds to harden the resist. Then the wafer is aligned using a mask aligner and is brought in hard-contact with the mask. The intensity of UV light is measured prior to exposure and based on this intensity, the exposure time is calculated to achieve a dose of $40 \text{ mJ} / \text{cm}^2$ ($= \text{Exposure time} \times \text{Intensity}$). The wafer is exposed. During the exposure, light can only go through transparent parts on the mask where the patterns are. It changes the chemical properties of the resist at these locations and leaves the rest unchanged. Our resist (S1813) is a positive-type resist, therefore the exposed parts can be removed in the developer (see Fig. 2.4). The wafer is immersed in the

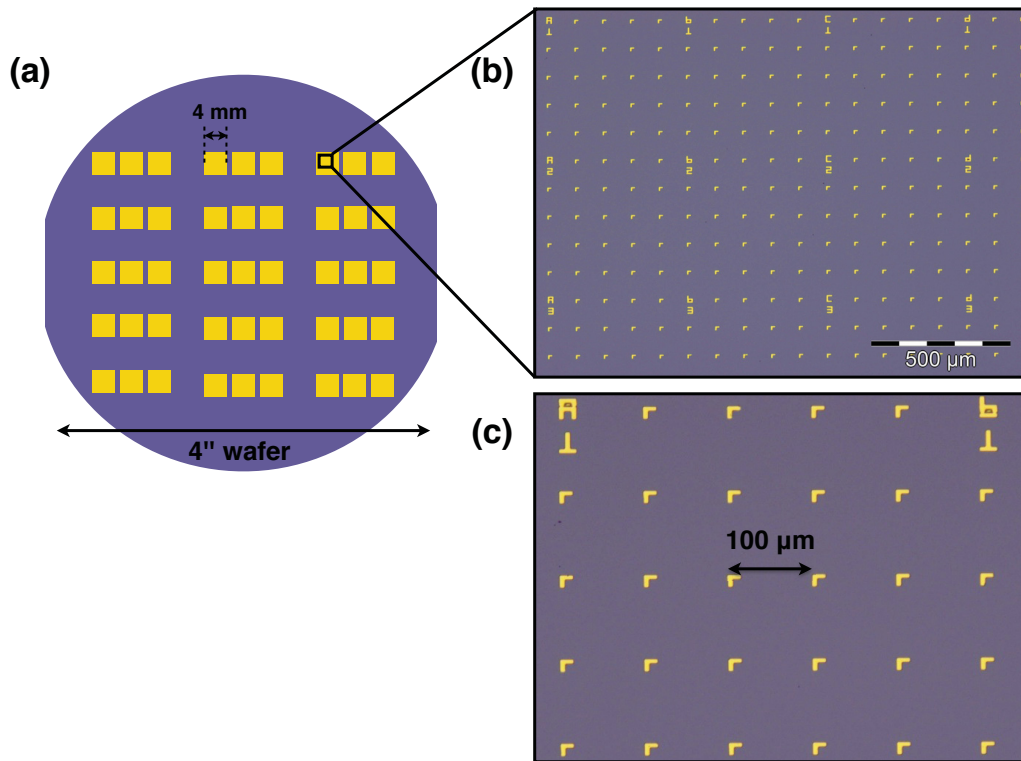


Figure 2.3: Mask pattern for coordinate grids. (a) Cartoon of a wafer showing dies of $4\text{ mm} \times 4\text{ mm}$. Each die has a coordinate grid patterned by photolithography. (b) Optical image of a die showing a part of the coordinate grid. Some of the letter-number symbols and L-shaped alignment marks of the grid pattern are visible. (c) A zoom-in on the image presented in (b). The alignment markers are spaced $100\text{ }\mu\text{m}$ apart.

developer, MF-319 for 1 minute and then rinsed with deionized (DI) water to stop the developing process. After drying with nitrogen gas, the quality of the exposed pattern can be checked under a yellow light optical microscope. If resist residues remained inside the pattern, the wafer can be soaked in the developer for short period of times and checked, until the pattern is completely developed. However, if the exposure is not good enough or can not be fixed with development, the resist should be removed completely with acetone, and the process repeated.

2.1.3 Metal deposition of coordinate grids

After the photolithography of coordinate grids, we deposit a layer of metal to transfer the pattern on the substrate. Gold (Au) is evaporated on the substrate using an electron-beam or a thermal evaporator. Fig. 2.5(a) shows an image of an electron-beam evaporator that is equipped with multiple evaporation sources (Au, Pt, Ti, Cr..). The electron-beam is accelerated to a high kinetic energy and is targeted on the source metal under a high vacuum. This evaporates the solid metal. The released metal atoms hit everything in the vacuum chamber, including the substrate. These atoms eventually loose their energy and solidify into a thin film which coats the substrate. Fig. 2.5(b) shows a picture of a thermal evaporator which can deposit Chromium (Cr) and Gold (Au). The source metal is evaporated by applying current through it and the deposition is made in a vacuum chamber like in the electron-beam evaporator.

After patterning the alignment marks on the resist (see Fig. 2.5(c) for the cartoon), we deposit metal using either an e-beam or a thermal evaporator. We first coat the substrate with a thin layer of titanium (Ti) or chromium (Cr). This layer will help the second layer, gold (Au), to stick on the substrate. We only deposit 3 to 5 nm of this adhesive layer which is sufficient to hold the Au layer. As for the Au film, we usually evaporate 50 nm for coordinate grids. Thicker than 50 nm can be used, but it would not be necessary. During deposition, the thickness of the film is monitored with a crystal thickness monitor installed in the evaporator. After evaporation, we place the samples in a solvent, acetone, for the lift-off process. Acetone dissolves the unexposed resist and lifts the metal layers on top. Thus the substrate will only be left with the coordinate grid pattern as seen in Fig. 2.5(c).

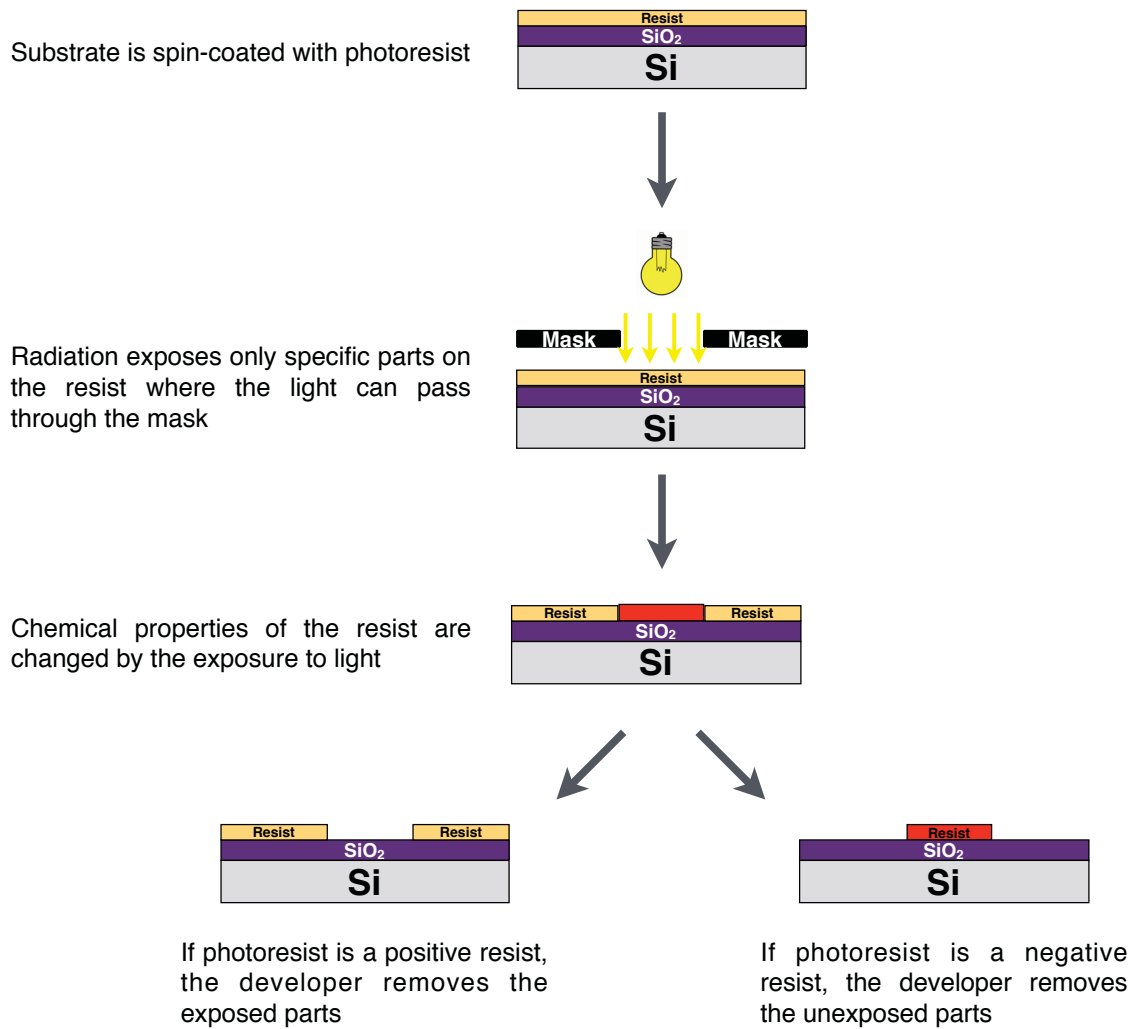


Figure 2.4: Cartoon of the photolithography procedure: spinning of photoresist, exposure and development.

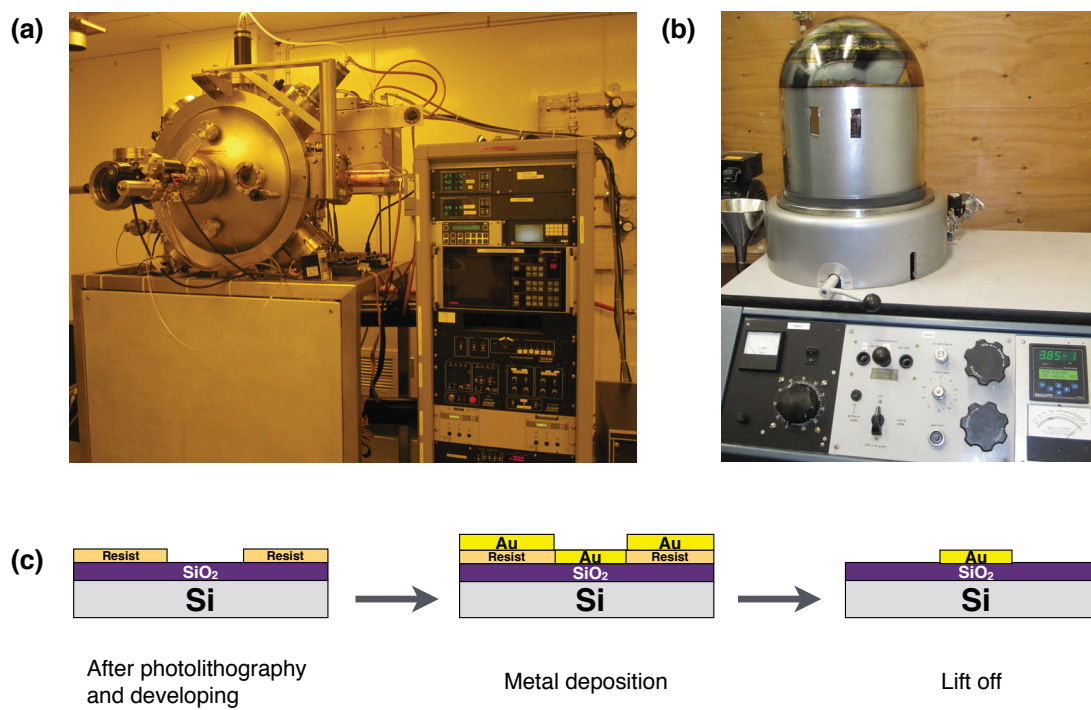


Figure 2.5: (a) Pictures of electron-beam evaporator and (b) thermal evaporator. (c) Cartoon of the metal deposition and lift-off procedure.

2.1.4 Mechanical exfoliation of graphene crystals

We use a regular scotch tape to exfoliate and deposit graphene crystals on our substrate. This, so-called “mechanical exfoliation” or simply “scotch tape method”, was invented and used by A. Geim and K. Novoselov to isolate the first single layer of graphene in 2004 [1,37,61]. Before graphene deposition, we first dice the wafer into $6\text{ mm} \times 6\text{ mm}$ chips containing a coordinate grid pattern. Then we clean the chips to ensure that their surfaces are completely clean. To do so, we soft etch SiO_2 in a solution of $\text{H}_2\text{O} : \text{H}_2\text{O}_2 : \text{HCl}$ (8 : 1 : 1) at 75°C for 5 minutes. The chips are rinse with DI water and dried with N_2 gas. Finally they are baked for 2 minutes at 150°C to remove water from the surface. The graphene deposition is done right away after cleaning to avoid any surface contamination.

For the exfoliation process (see Fig. 2.6(a)-(c)), we start with placing pieces of good quality Kish Graphite on a scotch tape. We then fold the scotch tape on itself sandwiching the graphite pieces between. As the tape is pulled apart, it cleaves the graphite into thinner crystals. Repeating this process over and over will peel off thinner graphene flakes from graphite. We do approximately 20 folds and peeling before transferring to the substrate. The tape is covered with graphite flakes as in Fig. 2.6(d). We finally stick the tape on a cleaned chip (Fig. 2.6(e)) and gently press down with plastic tweezers. Then the tape is slowly peeled away from the chip (Fig. 2.6(f)).

2.1.5 Verification of the number of atomic planes in the crystals

After graphene deposition, we look over the chips to see if there are any graphene flakes of interest. We would like to get monolayer graphene, the thinnest crystal possible. The determination of the number of atomic layers is a two step verification. The first step is done with an optical microscope which provides quick preliminary thickness measurements. The measurements are then confirmed by Raman spectroscopy. The second step is more reliable, as it can directly probe the characteristics of the lattice and provide quantitative results to verify the number of layers.

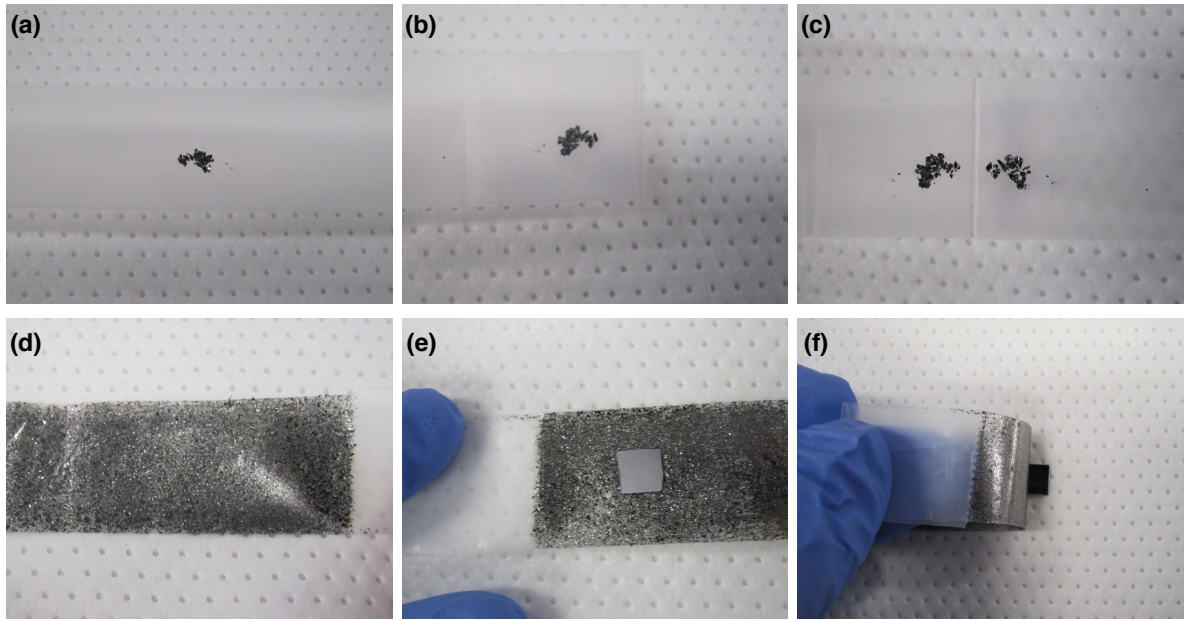


Figure 2.6: Mechanical exfoliation (scotch tape) method. (a) Graphite flakes are placed on a piece of scotch tape. (b) The tape is folded on itself so that graphite is sandwiched. (c) The tape is slowly peeled apart layering down the graphite crystals. (d) After 20 folding steps, the tape is covered with thin graphite flakes. (e) A substrate chip is stuck on the tape. (f) The tape is slowly peeled away from the chip.

Optical Spectroscopy

Despite being only one atom thick, graphene surprisingly has a strong interaction with light. Graphene on a SiO_2 / Si substrate in vacuum absorbs 2.3 % of the visible light intensity, independent of the wavelength. This leads to a light transmission coefficient of 97.7 % which makes graphene almost a transparent material [4]. Using an optical microscope, it is possible to see graphene on a SiO_2 / Si substrate. The thickness of the SiO_2 on Si wafer is chosen to be 300 nm, since it provides the best contrast for graphene under an optical microscope. Monolayer graphene crystals appear as the most transparent ones, and as the number of layers increases, the crystals' contrast increases.

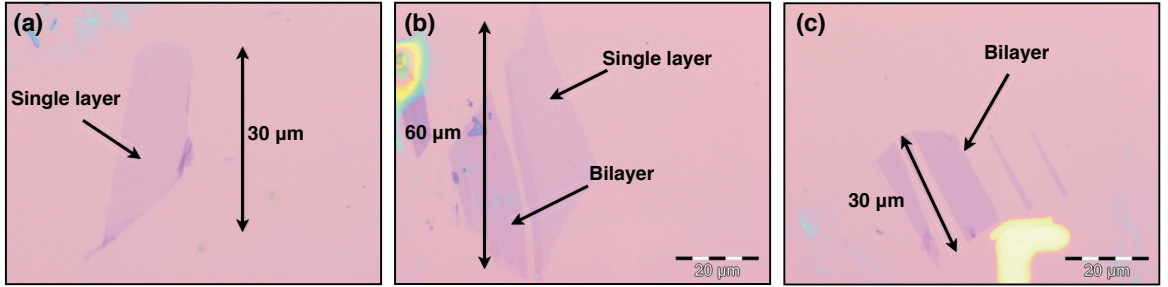


Figure 2.7: Optical images of graphene crystals. (a) Image of a monolayer graphene on SiO_2 , which has the lowest contrast under an optical microscope. (b) Image of a flake containing both mono and bilayer graphene. As seen in the image, bilayer graphene appears darker than monolayer graphene. (c) Image of a bilayer graphene flake.

In Fig. 2.7, optical images of mono and bilayer graphene flakes are shown. Single layer graphene is very transparent and almost the same colour as the background (Fig. 2.7(a)). On the other hand, bilayer graphene appears darker (Fig. 2.7(b) and (c)). Figure 2.7(b) provides a good visual comparison of the contrasts of mono and bilayer graphene, since they are located side by side.

We survey the surface of our chips with an optical microscope at $50\times$ and record the image and position of the most transparent looking flakes with respect to the reference grid. These flakes are initially labeled as monolayer flakes. We also locate the ones that have roughly double the contrast and we group them as bilayer flakes. Their thickness is then confirmed using Raman spectroscopy.

Raman Spectroscopy

Raman spectroscopy is a spectroscopic technique used to measure the phonon modes of a crystal. This method is based on inelastic scattering of a monochromatic light, usually from a laser source. A laser beam is illuminated on the sample and the scattered light's wavelength is measured. The energy of the photons in the scattered light is shifted up or down due to the interactions between incident light and molecular vibrations or phonons in the sample. This shift in energy provides information for sample identifications. Raman spectroscopy is a popular and widely used method to count the number of layers in graphene flakes [62–64]. Monolayer graphene has specific peaks in its Raman spectrum. The two distinct features are called G and 2D peaks (Fig. 2.8). The G peak appears around $1582 \pm 3 \text{ cm}^{-2}$ and is due to stretching of C–C bonds (in-plane vibrations) [65]. Monolayer graphene exhibits a single and sharp 2D peak at around $2679 \pm 3 \text{ cm}^{-2}$ that results from double-resonant intervalley scattering [66]. The position and FWHM (full-width-half-maximum) of the 2D band is sensitive to the number of atomic planes. Another peak which can be seen in graphene's spectrum is the D peak which appears around $1350 \pm 3 \text{ cm}^{-2}$. It arises from the breathing modes of six-atom rings and needs defects to be activated [64,67]. Hence, D peak is only seen in defective graphene and edges.

We use a Raman microscope with 514 nm laser excitation. A good spectrum can be acquired by optimizing the laser power and exposure time which we use. We first run tests on one graphene flake using different powers and exposure times and compare the spectrums. We start with a very small laser power and increase it in small steps with different exposure times until we acquire a low-noise spectrum. As soon as we obtain a good spectrum which takes a reasonable time to acquire, we keep using the same parameters for the rest of the samples. These parameters are usually in 25 - 35 μW and 60 - 90 seconds range. Using higher powers could provide a better signal in shorter times, but we avoid using such higher laser powers as they can distort the spectrum due to sample heating. After recording the spectrum, we look at the positions and FWHM of G and 2D peaks to confirm the number of layers. In Fig. 2.8, G and 2D peaks data from some of our samples are shown. The insets show optical images of the crystals. In panel (a), the G peak is located at $1583 \pm 3 \text{ cm}^{-1}$ and 2D peak is at $2681 \pm 3 \text{ cm}^{-1}$ which confirms that the flake is a single-layer graphene. In panel (b), the Raman peaks for a different graphene flake are shown. The inset

depicts an optical image of this flake. The data is taken from the most transparent part of the flake. The G peak appears $1582 \pm 3 \text{ cm}^{-1}$ and 2D peak sits at $2678 \pm 3 \text{ cm}^{-1}$. In Fig. 2.8, we zoomed-in on the Raman peaks and only show narrow sections of the whole spectrum. We can also make use of the G / 2D area under the peak to identify single vs bilayer and multiple layers as will be shown in Section 5.2.2.

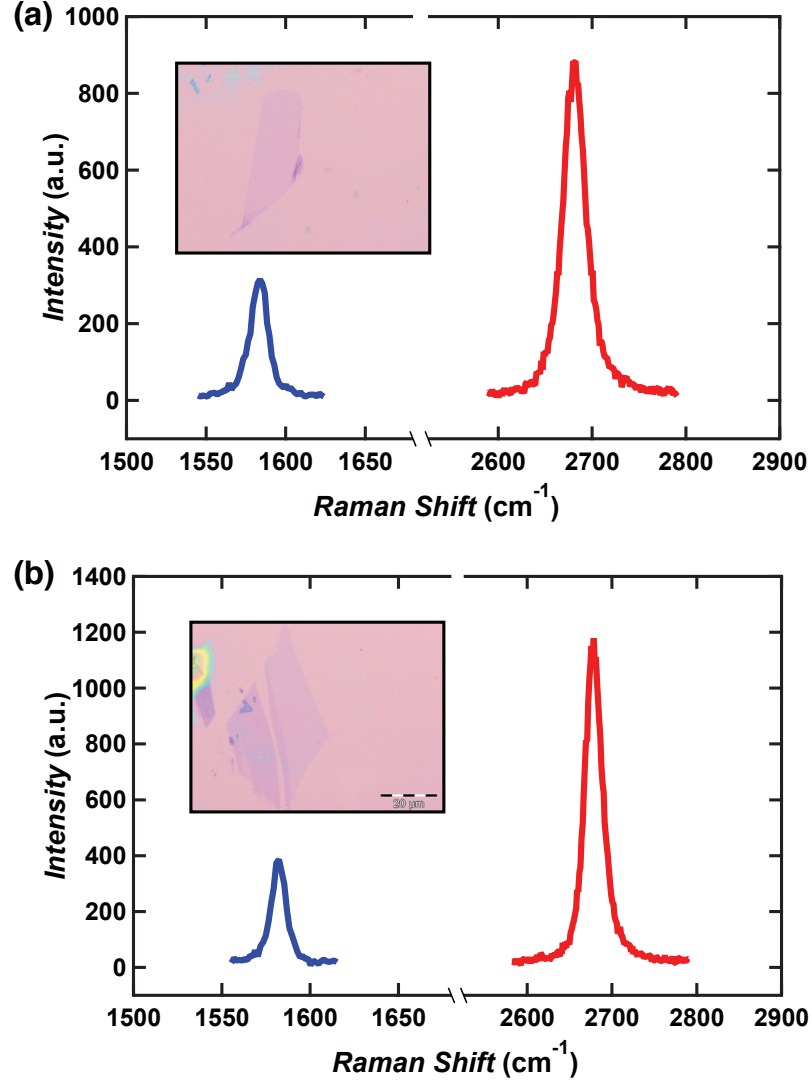


Figure 2.8: Raman spectroscopy is used to determine the thickness of graphene flakes. The positions of G (blue) and 2D (red) Raman peaks of monolayer graphene are shown. (a) The G peak is located at $1583 \pm 3 \text{ cm}^{-1}$ and 2D peak is at $2681 \pm 3 \text{ cm}^{-1}$. Inset: Optical image of the graphene flake from which the Raman data are taken. (b) Zoom-in on the G and 2D peaks of another monolayer graphene. The Raman data are taken from the flake shown in the inset picture. The G peak is at $1582 \pm 3 \text{ cm}^{-1}$ and 2D peak sits at $2678 \pm 3 \text{ cm}^{-1}$. The positions and FWHM of the peaks agree with the spectrum of monolayer graphene.

2.2 Making Electrical Contacts on Graphene

This section presents the fabrication of metal contacts on graphene flakes. We use electron-beam lithography to pattern and align the electrical contacts precisely on the flake. We also describe how we thermally evaporate metal to make mechanically sturdy contacts which will be very helpful for the suspension of the graphene.

2.2.1 Patterning contacts via electron-beam lithography

Electron-beam lithography is, like photolithography, a patterning technique to create structures on a resist. Instead of UV light, e-beam lithography uses a focused beam of electrons to scan the surface and draw patterns. The advantage of e-beam lithography over photolithography is that it can pattern any custom designed shapes with a very high resolution down to the 10 nm scale. This writing resolution is limited to about one micron in the case of standard photolithography.

Since e-beam lithography is a maskless patterning system, we create a design file using an AutoCAD design software. The e-beam writer software can read and expose the design file. Fig. 2.9(a) depicts a design which contains 8 large contacts. The dashed square is enlarged in the inset where the small contacts and alignment marks can be clearly seen. The alignment marks in the design file are drawn identically to the ones on the alignment grid patterned on the substrate (see section 2.1.2). The marks in design file will be overlaid on the markers on the substrate so that the whole pattern is properly aligned and drawn at the right location. Before exposing a pattern on the flake shown in Fig. 2.9(b), we first coat the chip with an electron sensitive resist. We use a bilayer resist of Copolymer EL9 (9 % in ethyl lactate) and PMMA A4 resist (polymethyl methacrylate 4 % in anisole). We spin coat each layer at 3000 rpm for 1 min, and bake them for 15 min each at 170 °C on a hot plate. This gives a copolymer and PMMA thicknesses of ≈ 300 nm and ≈ 200 nm respectively. After exposure, the samples are developed in a solvent to remove the exposed parts of the resist. We use a solution of 1:3 MIBK (methyl isobutyl ketone) : IPA (isopropyl alcohol) for 30 seconds followed by a rinse in methanol for 15 seconds. Finally the chip is transferred into IPA and is rinsed for at least 45 seconds to ensure that the developer is completely removed. Fig. 2.9(c) and (d) show optical images of the sample after exposure and development of the pattern. The small and large

contacts are drawn on the resist as they were designed. The small contacts are aligned precisely on the flake thanks to the alignment marks.

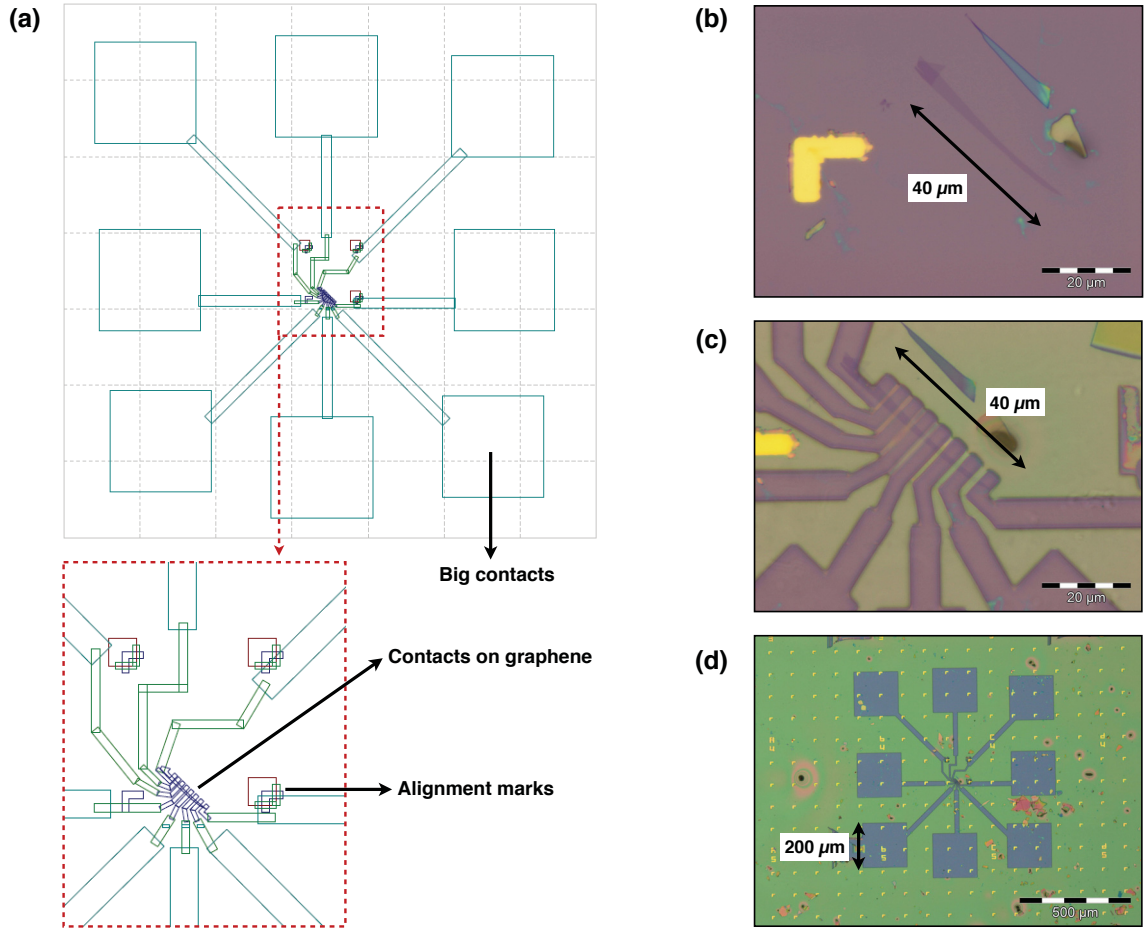


Figure 2.9: Electron-beam lithography of electrical contacts. (a) Image of an AutoCad design of contacts to be patterned via e-beam lithography (EBL). (b) Optical image of a graphene flake. (c) Image of the flake after EBL exposure. (d) Zoomed-out image of the sample showing large contact pads.

2.2.2 Metal deposition of contacts

After exposing and developing the contacts on the resist, we deposit a metal film using thermal evaporation. We first evaporate 3 nm of Chromium (Cr) as an adhesive layer and then deposit Gold (Au) on top. In the next step, we will suspend the graphene

flakes above the substrate by removing the oxide underneath. Having sturdy gold contacts will be extremely helpful during this process. Thick contacts will create a stronger supporting structure. Therefore we evaporate at least 80 nm of Au on the samples. If possible, we prefer to make even thicker contacts, up to 120 nm thick.

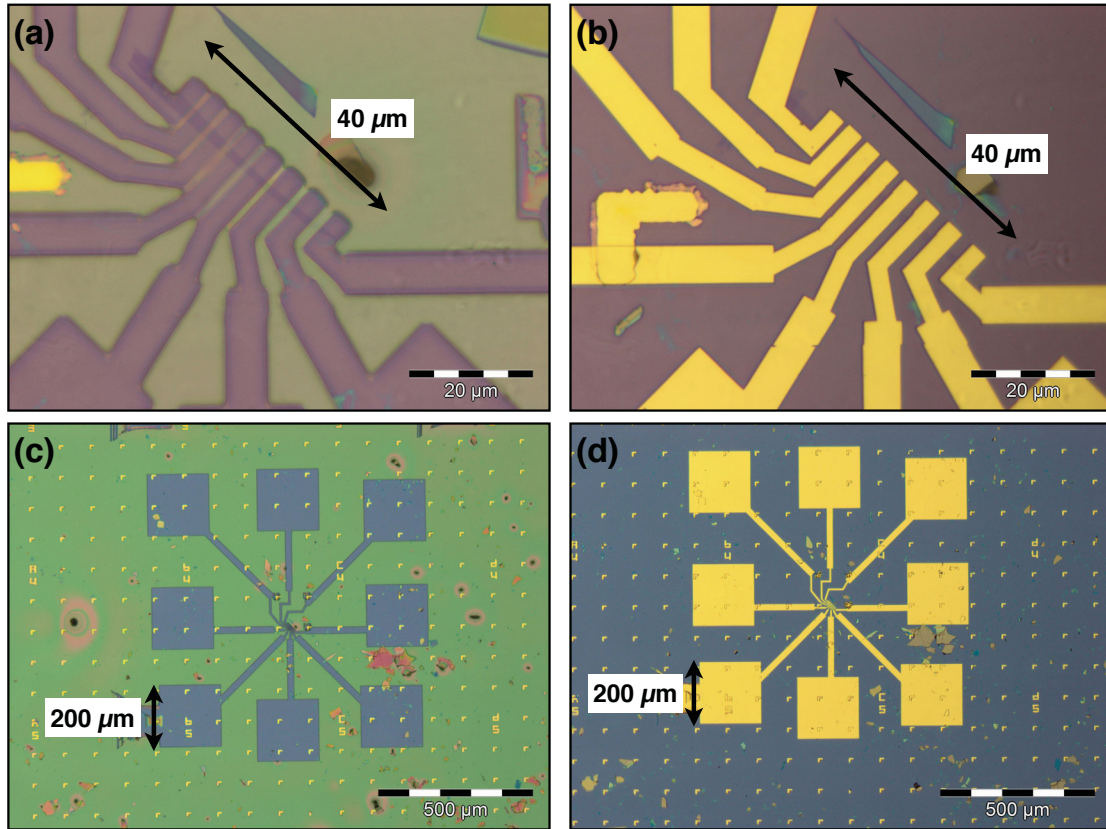


Figure 2.10: Metal transfer of contacts. (a) Image of contacts before and (b) after metal deposition at 100x magnification. (c) Image of contact pads before and (d) after metal deposition at 5x magnification.

After evaporation, we liftoff unexposed parts of the resist layer in acetone leaving the actual pattern on the substrate, and then rinse in IPA. Fig. 2.10(a) and (b) show small electrodes before and after evaporation. Similarly, Fig. 2.10(c) and (d) show the big contact pads before and after evaporation for the same sample.

2.3 Suspension of Graphene

After contacting graphene crystals with metal electrodes, our devices are now ready to be suspended. We remove the SiO_2 underneath the graphene channel so that it will be left hanging above the substrate anchored to the contacts at each end. The suspension will thermally isolate the devices from the substrate and thus remove any heat leakage to the substrate. Moreover, the suspension will decouple the charge transport from the impurities in the substrate.

2.3.1 Wet-etching

For suspension of graphene flakes, we use a wet-etching process in which the samples are immersed in a solution which eats away the oxide. We use a wet etchant, BOE (buffered oxide etch), a mixture of HF (hydrofluoric acid) and NH_4F (ammonium fluoride). Depending on the mixing ratio, the etch rate is tunable. For our samples, we prepare the BOE with 10:1 ratio (10 parts NH_4F and 1 part HF) which yield an etch rate of about 50 nm per minute. The etch rate of the mixture must be well-calibrated and the etching time must be well-adjusted in order to achieve a successful suspension. If the etching time is not long enough to etch the oxide underneath of graphene, it will not be fully suspended. Fig. 2.11(a) shows a SEM image of such a device which was not etched enough and therefore not suspended. It can clearly be seen that the flake is suspended on the edges, but oxide is left under the center of the flake. Fig. 2.11(b) shows a properly suspended device where the oxide underneath is smooth and the flake is completely detached from the substrate.

To etch the devices, we start by immersing the samples in the BOE solution. The samples are quickly removed as soon as the etching time is up and rinsed in DI (deionized) water. At this stage, the samples are rinsed in fresh DI water for at least 3 times to ensure there is no HF left on them. The samples are then put in IPA (isopropyl alcohol) for a final rinse before drying. It is extremely important to keep the samples wet at all times when moving them between any two solutions. The drying process is dependent on the size of the sample. If the length of the flake between the contacts is $\lesssim 1.3 \mu\text{m}$, the sample is gently dried with N_2 gas flow. For longer devices, we use CPD (critical point drying). CPD is used for sensitive devices which can be damaged due to the surface tension of the IPA. In a CPD chamber, IPA

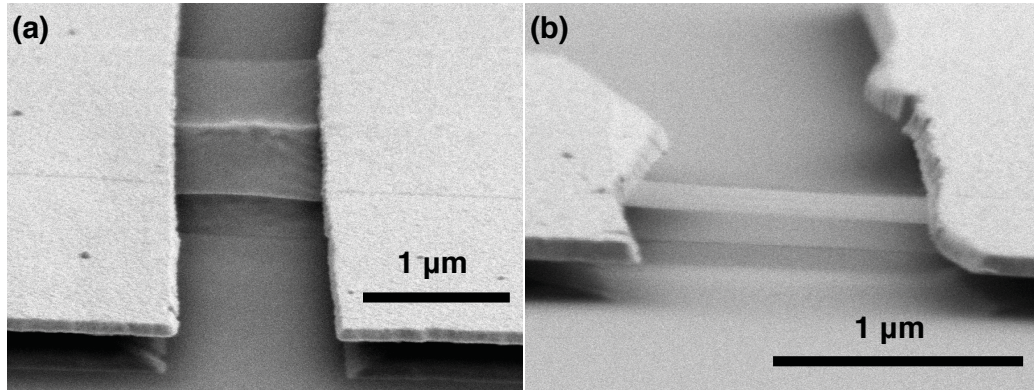


Figure 2.11: SEM images of devices after BOE etching. (a) A device which was not fully suspended as the oxide underneath was not completely removed. Oxide was left along the middle of the flake. (b) A perfectly suspended device.

is first replaced with liquid CO_2 (carbon dioxide). Then, the CO_2 is brought around its critical point using a high temperature and pressure. In this process, CO_2 becomes a supercritical fluid, a medium where the liquid and gas states are indistinguishable, which reduces the surface tension between the interfaces to zero. Finally, the sample is dried and returned to room temperature and pressure.

2.3.2 Ellipsometry and reflectometry

Ellipsometry or reflectometry is an optical method to characterize thin films such as SiO_2 , resists, etc., on substrates. The light is incident on the surface with an angle or directly and the reflected light is detected. The polarization difference between the incident and reflected light is analyzed to obtain the thickness of the film. Fig. 2.12 shows the ellipsometer that we use to measure the thickness of the SiO_2 films on our samples. We do this before wet-etching devices to calibrate the etch rate of the BOE solution, as well as after the etching to keep record of the thickness of SiO_2 remaining on the samples.

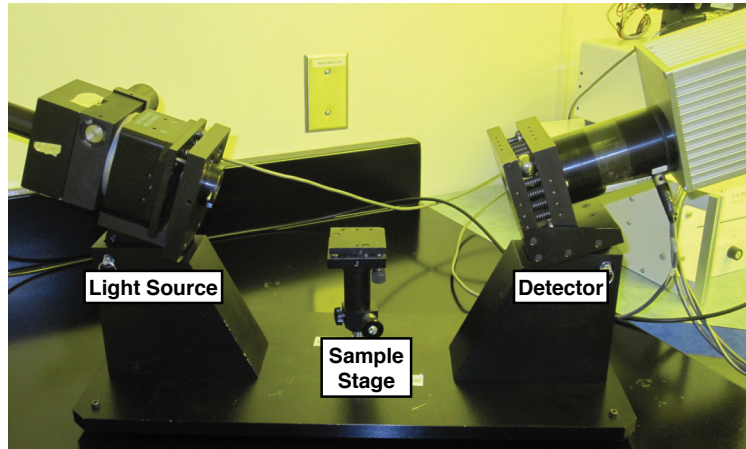


Figure 2.12: Picture of an ellipsometer showing its light source, sample stage and detector. An ellipsometer analyzes the change in polarization between incident and reflected light from a thin film to measure the thickness the film. We use an ellipsometer to measure the thickness of the SiO_2 films on our samples.

2.3.3 Scanning electron and atomic force microscopy imaging of devices

Scanning electron microscope (SEM) is used to capture images of the devices. We take tilted SEM images of devices as in Fig. 2.11 to check if they are completely suspended, and top-view images to measure the width and length of graphene flakes. However, we avoid using SEM before measuring transport data in the devices. SEM scans the surface with a beam of electrons, and deposits amorphous carbon (from background pressure in the vacuum chamber) on the graphene which later cannot be removed. Since it alters the properties of graphene, we do not take SEM images until we are done with studying the samples. Instead, we prefer using an atomic force microscope (AFM) which keeps the samples cleaner. AFM can provide precise measurements of the height of suspension as well as the length and width of the flake. It is important to use tapping mode instead of contact mode not to rip the flake apart as the AFM tip scans. Fig. 2.13 illustrates a screenshot from the AFM software. The panel (a) is an AFM scan of a suspended device. The white line on the image can be moved around anywhere on the scan to extract a 1-dimensional cut from height data. The plot in panel (b) displays a 1-dimensional cut from the data taken along

the line. It shows a step-like shape where the flake is suspended above the substrate.

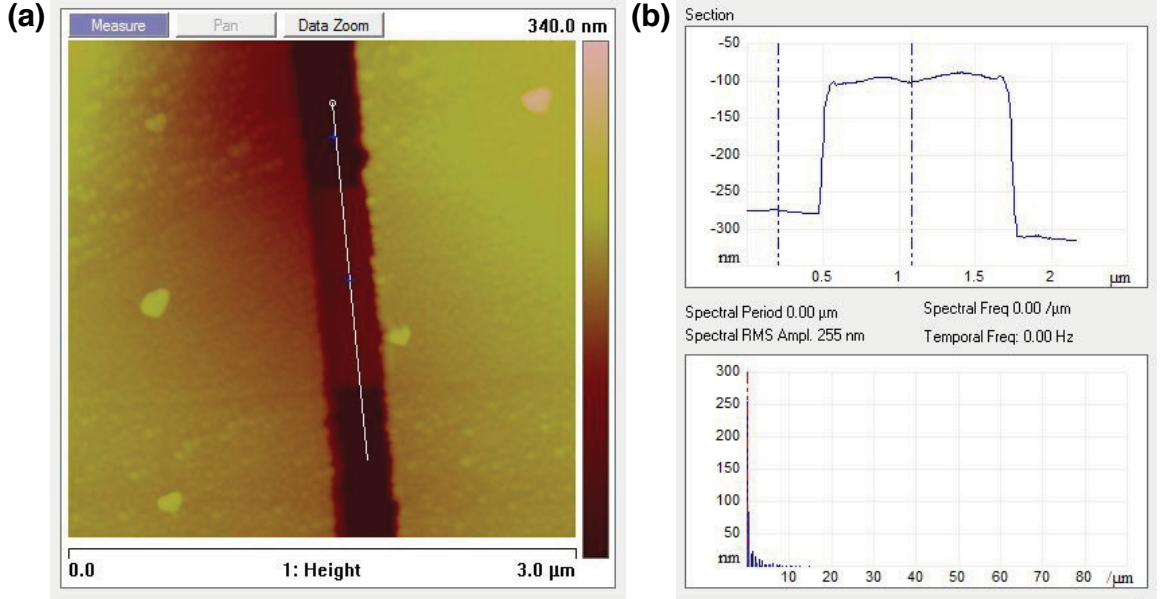


Figure 2.13: AFM imaging of suspended graphene transistors. (a) A screenshot of the AFM software showing an AFM scan of a suspended device. The white line is placed perpendicular to the channel to extract 1-dimensional data. (b) Plot showing the data cut along the white line in (a), which presents the height profile of the suspended channel.

2.4 Measurement Set-up and Circuits

This section describes how we package the samples after fabrication and prepare them for measurements. In addition, we present our measurement circuits and data acquisition procedure.

2.4.1 Testing graphene devices with a probe station

Before packaging the samples, we can test them with a probe station (shown in Fig. 2.14). The needle-shaped probes can be aligned and touched down on the contact pads of the devices by looking through a stereoscope. Current – voltage ($I - V$) data are taken to verify if the transistor is working, and its resistance is extracted from the slope of the $I - V$ curve.

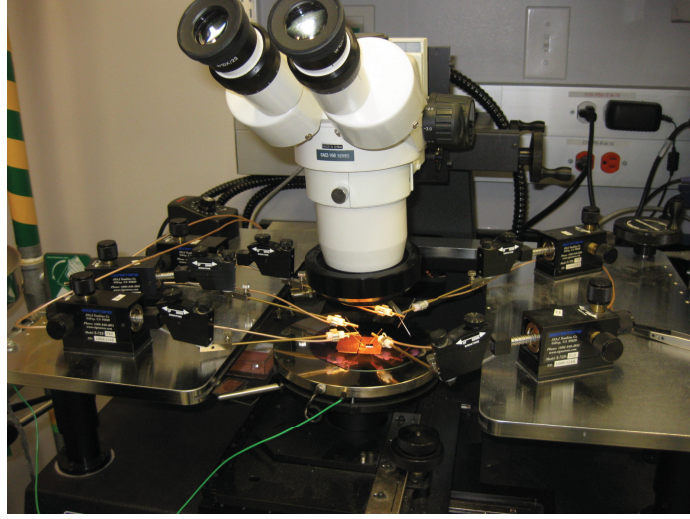


Figure 2.14: Image of the probe station we use to test the samples.

2.4.2 Wire-bonding and handling of samples

In section 2.2.1, we described the fabrication of micron-size electrical contacts on graphene along with large contact pads using EBL. In order to make measurements through these contacts, we need to interconnect the large pads to chip carriers. To do so, we use a wire-bonder which welds (ultrasonic welding) aluminum wires from chip carriers to the gold contact pads. Fig. 2.15(a) shows an optical image of a device with wire-bonds on its gold pads. The wire-bonds on the chip carrier can be seen in the zoom-out image in Fig. 2.15(b). The sample is glued on the chip carrier using a conducting silver print on its back side. The back of the sample must be electrically connected on the gold plate in the middle of the chip carrier to use the Si substrate as a back-gate electrode. We make wire-bonds to the gold plate as well in order to control back-gate voltage. During and after wire-bonding, the samples must be handled very carefully and be grounded to protect the devices from any possible electrical discharges. Wire-bonded samples are stored with the chip carriers in gel-paks to shield them until measurements. To acquire data, the chip carriers are mounted on the chip socket of the cryostats (see Fig. 2.15(b)). The pins of the chip carrier are connected via the chip socket to the electronic measurement set-up.

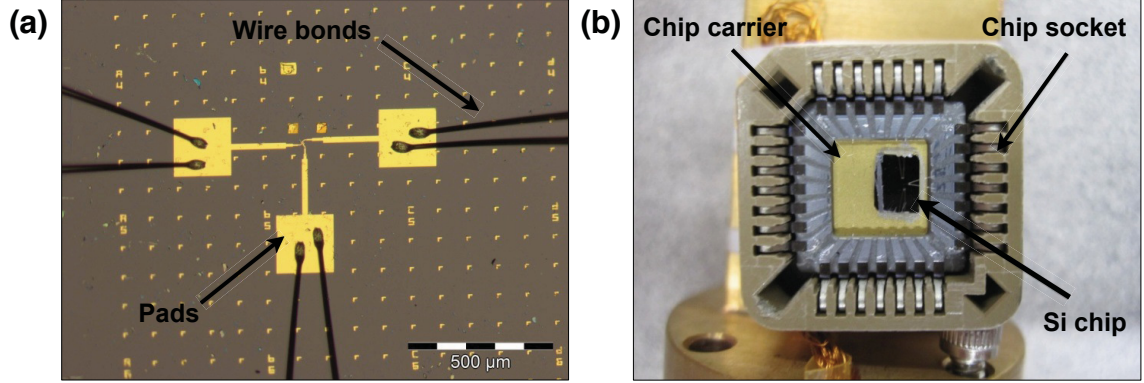


Figure 2.15: Wiring-bonding of the samples. (a) Optical image of a device with wire-bonds on the contact pads. (b) Image of a chip carrier with a sample wire-bonded on it. The chip carrier is mounted on the chip socket made for the measurement set-up. The chip socket provides the connection between the pins of the chip carrier and the electronic set-up.

2.4.3 Cooling down to low temperatures

The experiments are performed under high vacuum and at different temperatures ranging from low to high (usually up to room temperature). We need to have a good control of the temperature at which the data are taken. Hence, we make use of a variable temperature cryostat (VTI) which can make use of Liquid He-4 or Liquid N_2 (see Fig. 2.16) to cool down. It can reach down to 1.5 K with LHe and to 77 K with LN_2 . The sample space in the cryostat can be pumped out and kept under high vacuum (10^{-6} Torr). There is a thermometer and a heater, inside the sample space, which are controlled by a temperature controller. This latter measures and adjusts the temperature of the sample space. We can control the temperature of the sample up to 420 K.

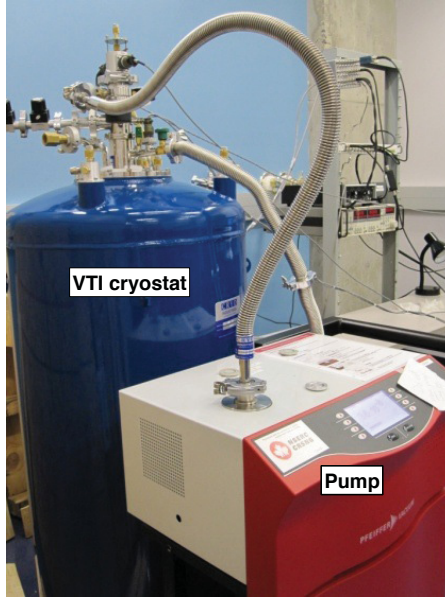


Figure 2.16: Picture of the variable temperature cryostat (VTI) with a turbo-pump attached to the sample space. It pumps down the sample space to a high vacuum. The VTI can cool down to 1.5 K and reach up to 420 K.

2.4.4 Electronic set-up and circuits

Our electronic set-up is designed in a such a way that the sample is kept grounded and shielded at all times when not being measured. While data are taken, we make sure that there are no ground loops in the circuit and all electronics are grounded at one common ground. We also use a personal grounding strap on our wrist. Fig. 2.17 is a cartoon of our DC circuit. Data are collected using a National Instruments Data Acquisition System (DAQ) with a custom coded GUI (graphical user interface), and GPIB instrument control. The connections between the sample and any apparatus shown in Fig. 2.17 are made using BNC coaxial cables. We keep these cables as short as possible to prevent any noise pick-up and wrap them with additional coaxial cables to create shielding. We use a voltage-divider in our circuits when we apply small voltages, and low-pass filter for the Keithley voltage source to avoid any spikes in gate voltages. The data are collected and stored in the computer with a chosen file name as well as the date and time of acquisition.

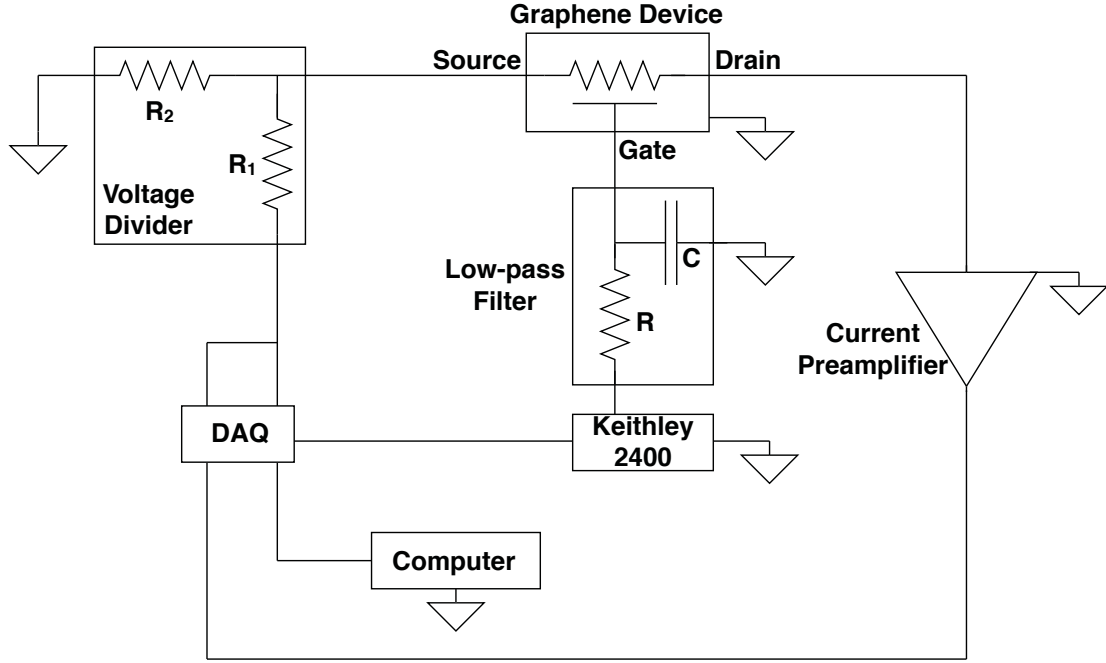


Figure 2.17: Electrical circuit for dc measurements.

2.5 Fabrication Results

In this chapter we described the fabrication procedure that we developed to make suspended graphene transistors. Our aim is to understand and extract electronic thermal conductivity in graphene. To do so, we proposed a device design at the beginning of this chapter in Fig. 2.1. Throughout the chapter, we explained step-by-step the fabrication procedure to make such suspended graphene devices. Fig. 2.18 shows the device design and SEM image of an actual device we fabricated. It clearly shows that we achieved our fabrication objectives. By isolating the graphene crystal from the substrate, we aim to reach high mobilities for charge carriers and remove any heat leakage to the substrate. In addition, we use the mechanical exfoliation method to create graphene crystals, since it provides the highest quality graphene crystals. This method has no control over the size and shape of the flakes. For our suspended devices, we need rectangular shaped flakes (for easy modelling) with widths up to $2.5 \mu\text{m}$ and lengths of at least $5 \mu\text{m}$ to be able to fit two large area (low resistance) contacts on it. Larger and irregularly shaped graphene flakes can be cut into specific sizes by etching them with RIE. This is a commonly used method to get regular

shaped flakes of any size. However this creates disorder on the edges of the flakes and affects the transport measurements. Therefore we never used RIE to cut down and shape our graphene devices. We only used the flakes that were naturally in the shape and size that we needed.

In the following chapter, we will present how we studied these samples to extract their electronic thermal conductivity.

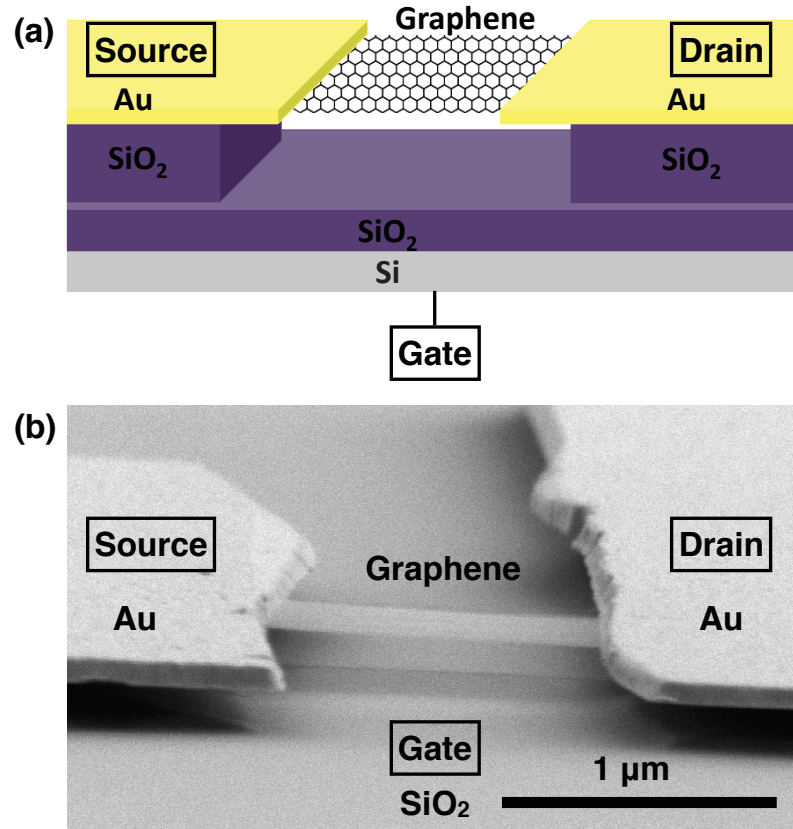


Figure 2.18: (a) Target design of a suspended two-point device. (b) SEM image of a device that we fabricated.

Chapter 3

Electronic Thermal Conductivity of Monolayer Graphene in Intrinsic Regime

The electronic thermal conductivity of graphene and two-dimensional (2D) Dirac materials is of fundamental interest and can play an important role in the performance of nanoscale devices [3, 5]. We report the electronic thermal conductivity K_e in suspended graphene in the nearly intrinsic regime over a temperature range of 20 to 300 K. We present a method to extract K_e using two-point DC electron transport at low bias voltages, where the electron and lattice temperatures are decoupled. We find K_e ranging from 0.5 to 11 W/m.K over the studied temperature range. The data are consistent with a model in which heat is carried by quasiparticles with the same mean free path and velocity as graphene's charge carriers.

We first describe our samples and present their resistance vs gate voltage data from which we can deduce the cleanliness of our samples by calculating their impurity density. Secondly, we discuss the contact resistance in our samples. After that we will move on to our thermometry technique where we will explain how we can monitor and control the temperature of electrons in graphene. By solving a one-dimensional heat equation, we will be able to extract K_e at different temperatures. Finally we will present the theoretical model we used to model our experimental data. The work presented in this chapter was adapted from the following publication: "Electronic thermal conductivity measurements in intrinsic graphene", Serap Yiğen

et al., Physical Review B, 87 (2013) [14]. I did vast majority of the fabrication of all samples and I acquired 100% of the data presented in this thesis. The data were analyzed by me and Dr. Alexandre Champagne. The co-authors contributed with technical helps and discussions during fabrication and measurements.

3.1 Introduction

The electronic heat conductivity of graphene K_e describes how charged quasiparticles carry energy as they diffuse in this material. It could also shed light on K_e in other 2D Dirac systems whose electronic band structure is related to graphene's, such as the surface states of topological insulators [68]. When a hot electron diffuses out of graphene, it cools down the electronic distribution. Thus, measurements of K_e are needed to complement the understanding of the other hot-electron cooling mechanisms in graphene which involve various electron-phonon couplings [23, 57, 69–76]. Measuring and controlling K_e could have applications in the heat management of heavily-doped nm-scale devices where K_e can be dominant [77], and in optimizing graphene's electro-optical properties [16, 17]. While there have been several experimental reports of the phononic thermal conductivity K_p in graphene [11, 16, 17, 19, 44, 51, 54, 78, 79], reports of K_e measurements in suspended graphene are lacking. This is because in most regimes K_p is much larger than K_e , which makes it difficult to measure the amount of heat carried by the charged quasiparticles (electron and holes).

We present a carefully calibrated method to extract K_e in graphene using DC electron transport in suspended devices. The accuracy of the method is dependent on high-mobility (annealed) devices. We present data from three different samples which show consistent results. The extracted K_e are compared with calculated values, K_{e-th} , for a diffusing gas of Dirac quasiparticles. The agreement between theory and measurements is quantitative for all three devices over the temperature range (20 - 300 K) studied. Throughout the text we use T to designate the lattice (cryostat) temperature, and T_e for the average electron temperature in the suspended devices. At very low bias, $|V_B| \lesssim 1$ mV, $T = T_e$. We first describe our samples, second, we present our T_e thermometry, then show how we apply a controlled ΔT using Joule heating, and finally extract K_e from the transport data.

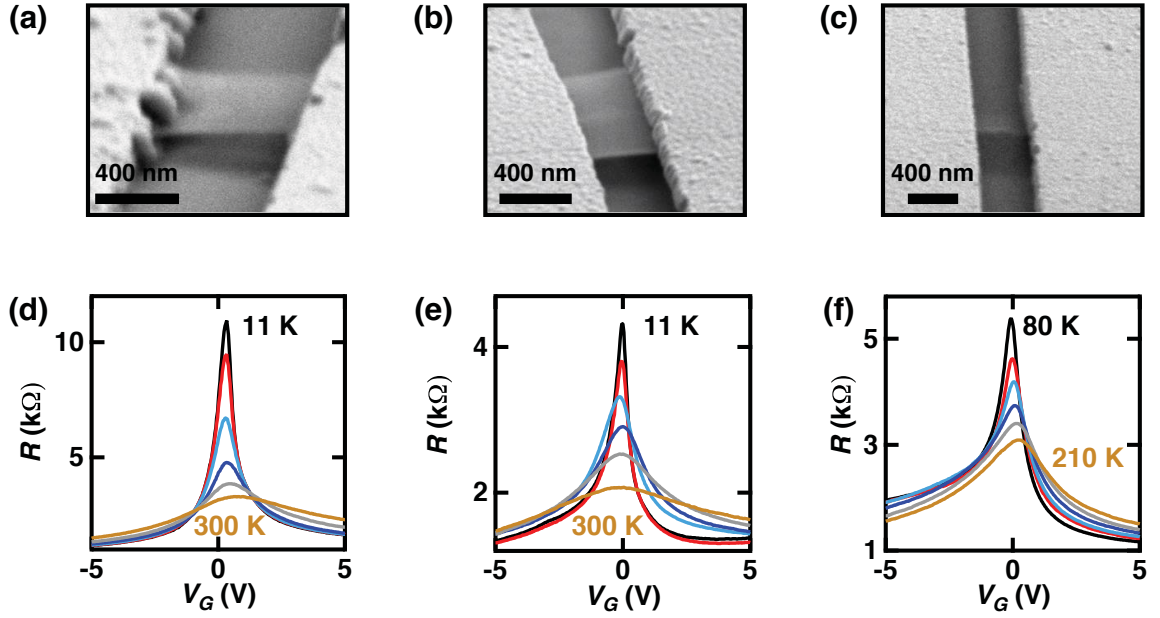


Figure 3.1: Suspended graphene devices. (a) - (c) Tilted SEM images of 650 nm, 400 nm and 400 nm long suspended graphene transistors (samples A, B and C). (d) - (f) Resistance R of sample A, B and C vs gate voltage V_G at $T_e = T = 11, 50, 100, 150, 210$, and 300 K (Samples A and B) and $T_e = T = 80, 100, 125, 150, 180$, and 210 K (sample C) and $V_B = 0.5$ mV.

Figure 3.1(a)-(c) show tilted scanning electron microscopy (SEM) images of Sample A, B and C respectively. We confirmed using optical contrast and Raman spectroscopy that all three samples are single-layer graphene. Sample A is 650 nm long, 675 nm wide, and suspended 140 ± 10 nm above the substrate [atomic force microscopy (AFM) measurement] which consists of 100 ± 2 nm of SiO_2 (ellipsometry measurement) on degenerately doped (Si) which is used as a back-gate electrode. Sample B is 400 nm long, $1.05 \mu\text{m}$ wide, and suspended 175 ± 10 nm above a 74 ± 2 nm SiO_2 film on Si. Sample C is 400 nm long, $0.97 \mu\text{m}$ wide, and suspended 227 ± 10 nm above a 74 ± 2 nm SiO_2 film on Si. To prepare the samples, we followed the fabrication methods which are explained in Chapter 2. We used exfoliated graphene, and standard electron beam lithography (EBL) to define Ti(5nm)/Au(80nm) contacts. The samples were suspended with a wet BOE etch such that their only thermal connection is to the gold contacts. We annealed the devices using Joule heating *in situ* by flowing a large current in the devices [40] (up to 540, 840 and 837 μA for A, B and C). Fig. 3.2 shows the two-point dc transport data in Sample A before (red) and after (black) current annealing. Annealing and subsequent measurements were done under high vacuum, 10^{-6} Torr.

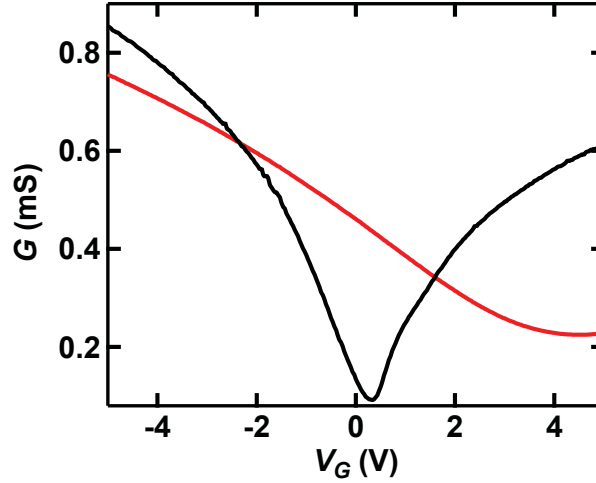


Figure 3.2: Sample annealing data. $G = I/V_B$ vs V_G data for Sample A before (red) and after (black) current annealing, $T \approx 20$ K.

Figures 3.1(d)-(f) show DC two-point resistance data, $R = V_B/I$, for Samples A, B and C respectively, after annealing, versus gate voltage V_G , which controls charge

density. From the width of the R maximum at 11 K, we extract a half width at half maximum (HWHM) of 0.45, 0.6 and 0.95 V for Samples A, B, and C. Using a parallel plate model for the gate capacitance of the devices, these HWHMs correspond to an impurity induced charge density [80] of $n^* \approx 1.5, 1.7$ and $2.1 \times 10^{10} \text{ cm}^{-2}$.

3.1.1 Upper bond for contact resistance

Our thermometry technique is based on two-point resistance measurement of graphene transistors. We used R both as a thermometer and heater to measure and control T_e in graphene. This is valid only if the contact resistance between graphene and contacts is not dominant over the graphene's resistance. Otherwise, the self-heating would happen at the contacts instead of in graphene crystal. In addition, the change of resistance with temperature would not be a good representation of T_e profile in graphene.

The devices were fabricated with large contact areas between the gold electrodes and graphene crystals, 1.1 to $3 \mu\text{m}^2$ per contact, to minimize the contact resistance R_c . An upper bound for R_c of our devices can be extracted from the two-point $R - n_G$ curves. The data for Sample A is shown in Fig. 3.3. We fit the data with the expression [42],

$$R = R_o + \left(\frac{L}{W}\right) \left(\frac{1}{n_G e \mu}\right) \quad (3.1)$$

where R_o is the resistance due to neutral scatterers plus R_c , L is the length of the device, W the width, n_G the charge density induced by V_G , μ the mobility, and e the electron's charge. We fit the data at $T = T_e = 100 \text{ K}$ for $(V_G - V_D) > 1.3 \text{ V}$ to avoid the thermal smearing around the Dirac point, V_D . The fit for the hole (electron) regime is shown as a light blue (red) dashed line in Fig. 3.3(a). The extracted mobility for Sample A in the doped regime is $\mu \approx 8.5 \times 10^4 \text{ cm}^2/\text{V.s}$ at 100 K, and $R_o \approx 682 \pm 53$ and $1135 \pm 80 \Omega$ for hole and electron doping respectively. The difference between hole, R_{o-h} and electron doping, R_{o-e} , is understood as an additional $p - n$ barrier for the electron due to p -doping from the gold electrodes [42]. Figure 3.3(b) shows the conductance, $G = 1/R$, for Sample A before the series resistance R_o is subtracted (black line) and after R_o is subtracted for the hole (light blue) and electron (red)

doped data. The corrected conductance depends linearly on the gate induced charge density, n_G .

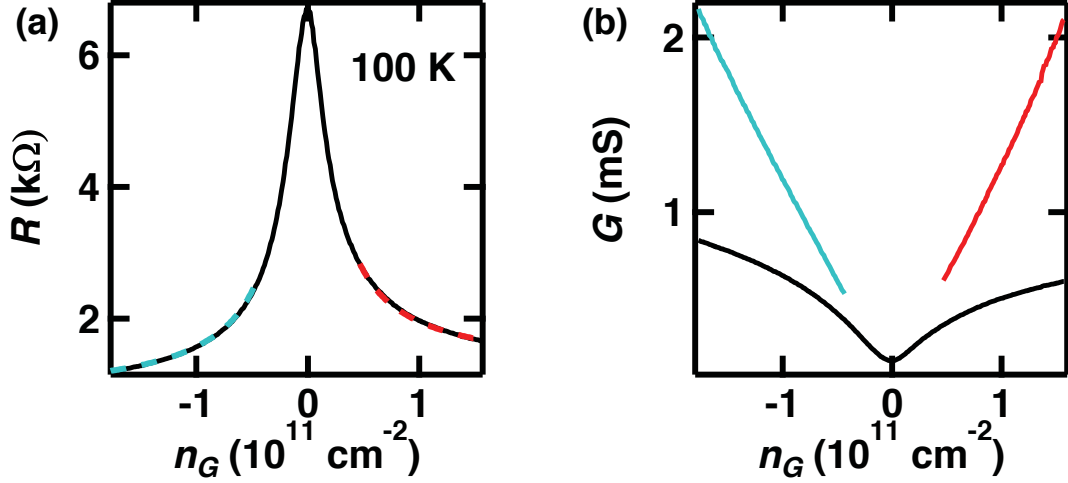


Figure 3.3: Upper bound for contact resistance of Sample A. (a) $R - n_G$ data at 100 K for Sample A. The light blue and red dashed lines are fits as described in the text from which the total series resistance, R_o , is extracted. (b) The same $G - n_G$ data as in panel (a), before (black line) and after (blue and red lines) subtracting R_o .

At the Dirac point, we let $R_{o-Dirac} = (R_{o-h} + R_{o-e})/2 = 908.5 \, \Omega$ for Sample A. For Sample C, we find $R_{o-Dirac} = 1097 \, \Omega$. We note that $R_{o-Dirac}$ is much smaller than R of Samples A and C, therefore $R_c < R_{o-Dirac}$ has at most a modest impact on our measurements in these devices. It is not possible to extract R_o for Sample B because it enters the ballistic regime away from the Dirac point (doped regime). In the doped regime (away from the Dirac point) and at low temperature, the R vs T data for Sample B are consistent with ballistic electron transport. These data will be discussed in Chapter 4. The contact areas of Sample B are larger, and its width wider, than for Samples A and C. Assuming a similar resistance per unit area as for A and C, we expect $R_c \lesssim 657 \, \Omega$ for B. Based on the reported thermal conductance of Au/Ti/Graphene and Graphene/SiO₂ interfaces [81], the thermal resistance of our contacts are several orders of magnitude lower than the one we measure below for graphene. Thus, the thermal resistance of the contacts can safely be neglected.

3.2 Electron Thermometry and Joule Heating of Electrons

After understanding the contact resistance in our devices, we present our technique by which we measure two-point R of the samples to monitor T_e in graphene.

Figure 3.4 shows R vs cryostat temperature, T , calibration curves for Samples A (circles, left axis), B (squares, right axis), and C (triangles, left axis) near $V_G = V_D$. $R = V_B/I$ data are extracted from the slope of the $I - V_B$ data as shown in the inset of Fig. 3.4 at 11 K (solid) and 300 K (dashed), for ± 1 mV bias where no Joule heating effect is present ($T_e = T$). The data are taken at $V_G = 0.5$ V close to $V_D = 0.33$ V for Sample A, and at $V_G = 0$ V for Samples B and C ($V_D = -0.1$ and 0.07 V), corresponding to $n_G = 5.7, 2.9$, and $-1.5 \times 10^9 \text{ cm}^{-2}$. The T dependence of the data shows an insulating behavior up to ≈ 200 K for Sample A and C, and up to 300 K for Sample B. The interpolated dashed lines in panel (a) will be used as thermometry curves to monitor T_e . Note that the thermometry is most accurate where the curves are steepest.

Figure 3.5 shows the relative conductance $G(T)/G_{11K}$ in the intrinsic regime extracted from Fig. 3.4 for Sample A and B. The T dependence of G in graphene, at low charge density, is strongly dependent on the type of charge transport. For ballistic transport, we expect a very weak temperature dependence at low T , and a linear dependence when $k_B T \gg E_F$ [82]. In the diffusive regime, the expected temperature dependence depends on the type of charge scatterers, and $G(T)/G_{11K} \propto T^\alpha$ with $\alpha = -1, 0, 2$ for acoustic phonon, short-range (neutral), and long-range (charged) scatterers respectively [25, 76]. The temperature dependence of real samples is expected to combine all three types of scattering. We fit the data with a function $G/G_{11K} = 1 + AT^p$, and extract $p = 1.85, 1.74, 1.72$ and 1.63 ± 0.03 for Sample A with $R_c = R_{o-Dirac}$ and 0 (open and filled circles), and Sample B with $R_c = 657$ and $0 \text{ } \Omega$ (open and filled squares). This T -dependence strongly supports diffusive charge transport dominated by long-range charge impurities, as reported in previous experiments on high-mobility devices [40, 76] and expected theoretically [25]. The small departure from a T^2 dependence is expected as the samples are not exactly at the Dirac point.

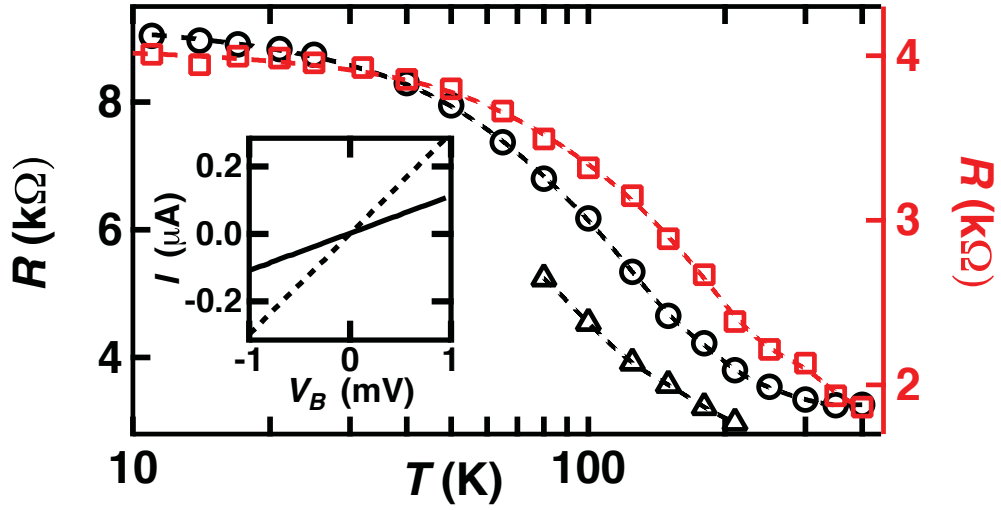


Figure 3.4: Electron thermometry. Temperature dependence of R in Sample A (circles, left axis), Sample B (squares, right axis), and Sample C (triangles, left axis) near the charge degeneracy $n_G = 5.7, 2.9$ and $-1.5 \times 10^9 \text{ cm}^{-2}$. The dashed lines are numerically interpolated curves used for thermometry. Inset: $I - V_B$ data for Sample A, $|V_B| < 1 \text{ mV}$, whose slope is used to extract R . The solid (dashed) line is at $T = T_e = 11$ (300) K.

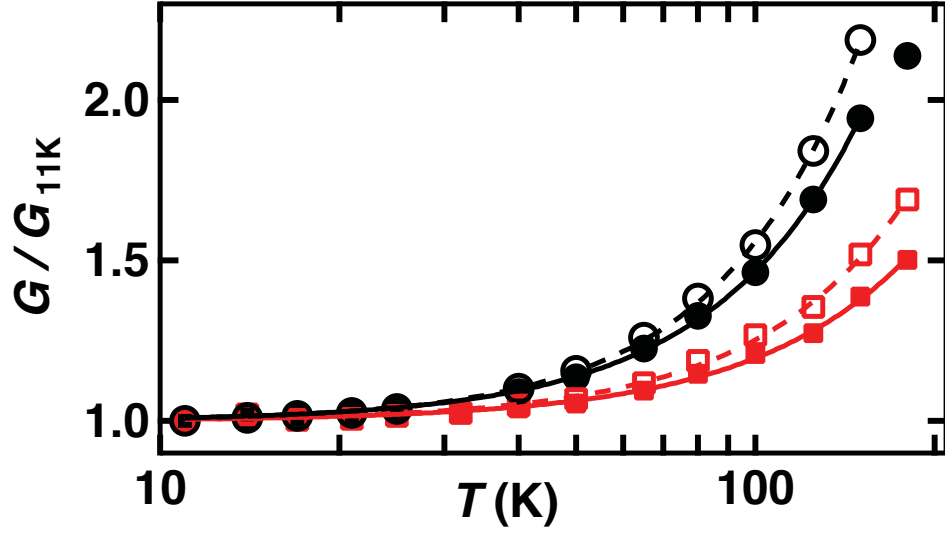


Figure 3.5: Relative conductance G/G_{11K} of Sample A (circles) and Sample B (squares) versus $T = T_e$. The filled symbols show the raw two-point data, and the open symbols the data after subtracting $R_c = R_{o-Dirac}$ (see text). The solid and dashed lines are power law fits consistent with charge impurity scattering.

3.2.1 Mean-free path in the nearly intrinsic regime

We calculated the mean free path of charge carriers in the nearly intrinsic regime to further support the existence of diffusive transport in our devices. In order to extract an approximate elastic mean free path, l , for charge carriers when the chemical potential is close to the Dirac point, we consider doping due to impurities, n^* , and thermally activated electron-hole pairs,

$$n_{th} = \left(\frac{\pi}{6}\right) \left(\frac{k_B T}{\hbar \nu_F}\right)^2 \quad (3.2)$$

where k_B is Boltzmann's constant, T the lattice temperature, $\nu_F = 10^6$ m/s the Fermi velocity. The total charge carrier density is [83]

$$n_{tot} = n + p = \sqrt{n_G^2 + 4 \left[\left(\frac{n^*}{2}\right)^2 + n_{th}^2 \right]} \quad (3.3)$$

where n_G is the charge density induced by the gate electrode. For instance, at $T = 100$ K we find $n_{tot}(100 \text{ K}) = 2.4, 2.5$ and $2.8 \times 10^{10} \text{ cm}^{-2}$ for Samples A, B and C. We calculate the charge carrier mobility,

$$\mu = \frac{\sigma}{n_{tot}e} \quad (3.4)$$

where σ is the charge conductivity. At $T = 100$ K, $\mu = 4.1$ (4.8), 2.9 (3.6), and 2.0 (2.7) $\times 10^4$ cm²/V.s using $R_c = 0(R_{o-Dirac})$ for Samples A, B and C respectively. The mobility decreases with T for all samples. From the mobility, we extract the mean-free path of the carriers as,

$$l = \sqrt{\frac{n_{tot}}{\pi}} \frac{h\mu}{2e} \quad (3.5)$$

At $T = 100$ K, we find $l = 74$ (87), 54 (67), 39 (52) nm for A, B and C, which is several times shorter than the size of the samples.

Hence, we conclude that all samples are in the diffusive regime at low charge density (Fig. 3.5 and mean-free path calculations) and scattering is predominantly due to charged impurities. The data in Fig. 3.4, and its agreement with theory, serves as a reliable thermometer for T_e in our devices.

3.2.2 Joule self-heating of electrons

After establishing the T_e thermometry, we demonstrate controlled Joule self-heating of the electrons to apply a thermal bias $\Delta T = T_e - T$ between the suspended graphene and the electrodes. Figure 3.6(a) shows R vs V_B for Sample A at $T = 50, 100, 150$ K (for Samples B and C see Figs. 3.7 and 3.8). Panel (b) shows the details of the data at 100 K. R decreases monotonically with increasing V_B , at all T . We argue that this change in the R vs V_B data is caused by Joule heating of the sample. Other mechanisms which could cause a non-linear $I - V_B$ relation include: scattering from flexural phonons, in-plane optical phonons, substrate phonons, and Zener-Klein tunneling. We restrict our measurements to $V_B \lesssim 30$ meV. This rules out any R change due to scattering from optical in-plane phonons, ≈ 200 meV, and flexural phonons, ≈ 70 meV, in graphene [76]. Phonons in the substrate can also be ruled out as the samples are suspended. The contribution of Zener-Klein tunneling to $I - V_B$ non-linearity was only observed in very low-mobility devices, and at $V_B > 100$ mV [84]. This leaves Joule heating as the only plausible cause for the observed R vs V_B behavior [24]. Using the calibration curve for the samples, Fig. 3.4, and data from Fig. 3.6(a) and 3.6(b), we extract the average T_e vs V_B , as shown for Sample A in Fig.

3.6(c) and 3.6(d). In Fig. 3.6(d), we fit a power law (solid line) $T_e = 100 + BV_B^x$, and find $x = 2.00 \pm 0.04$, as expected for Joule heating over a small T_e range where K_e and R do not change appreciably (Samples B and C, see Figs. 3.7 and 3.8). Figs. 3.6(d), 3.7(d), and 3.8(d) show that the accuracy with which T_e can be extracted is much better than 1 K. We calculate T_e errors from the scatter of the data in Fig. 3.6(d), and similar plots at each T , to vary from 0.2 K (steepest regions of Fig. 3.4) up to 2 K (flat regions of Fig. 3.4). The smooth dependence of T_e on V_B at all T is consistent with electrons having a well defined temperature, as predicted by calculations of the $e - e$ collision length [85] in the following section. This is also confirmed by the K_e data shown below.

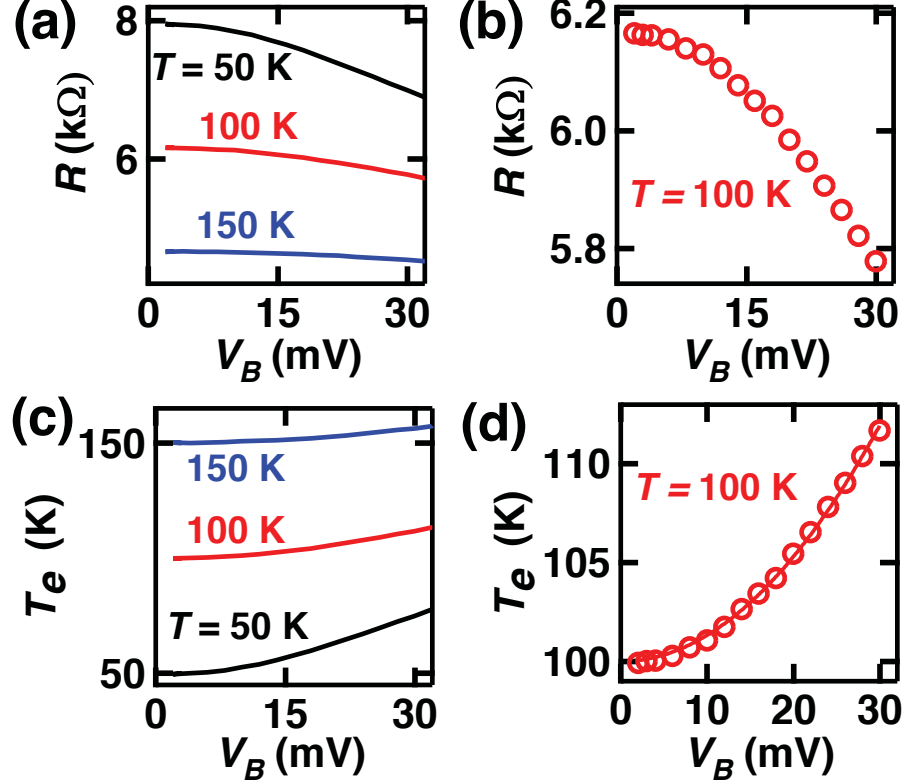


Figure 3.6: Electron heating for Sample A. (a) R vs V_B at various T for Device A at $V_G = 0.5$ V $\approx V_D$. (b) Details of the data at $T = 100$ K. Joule heating due to V_B raises the flake's average T_e above T . T_e is extracted using Fig. 3.4(a). Panels (c) and (d) show T_e vs V_B in Sample A at a few different T , and at $T = 100$ K respectively. All of our K_e data is extracted with $V_B \lesssim 30$ mV. The solid line in panel (d) is a power law fit $T_e = 100 + BV_B^x$, and we find $x = 2.00 \pm 0.04$, as expected for Joule heating over a small T_e range.

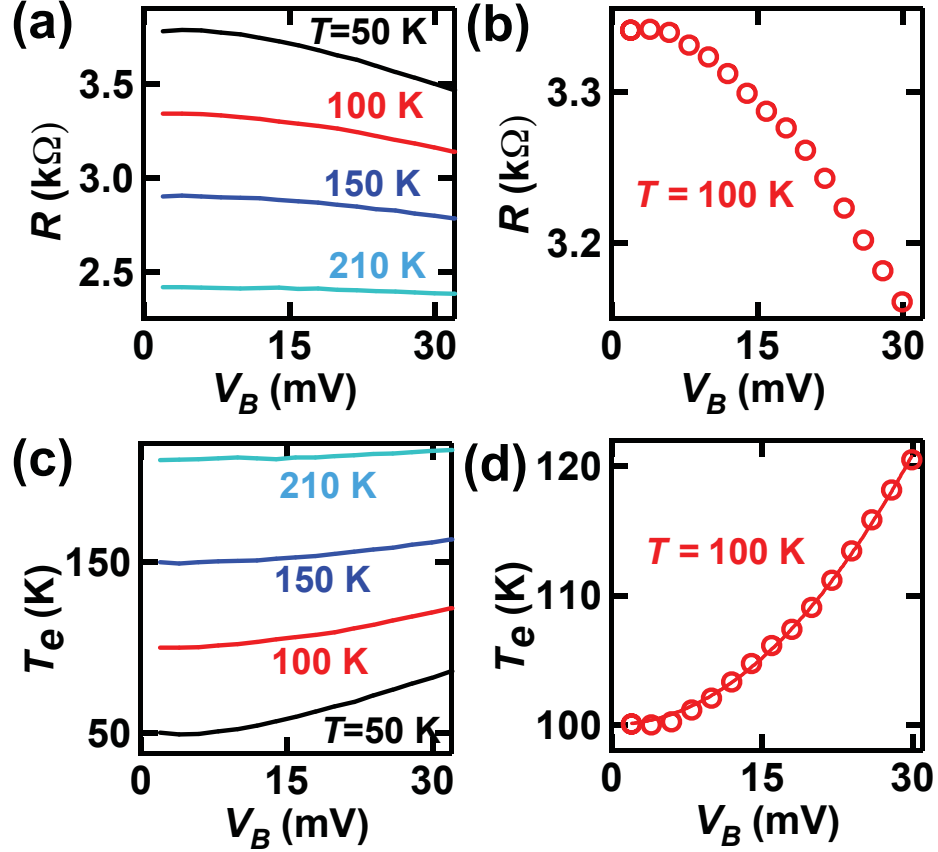


Figure 3.7: Electron heating for Sample B. (a) R vs V_B at $T = 50, 100, 150, 210$ K at $V_G = 0.0$ V $\approx V_D$. (b) Zoom-in on the 100 K data. Joule heating due to V_B raises the flake's average T_e above T . T_e is extracted using Fig. 3.4(a). Panels (c) and (d) show T_e vs V_B in Sample B at several T , and at $T = 100$ K respectively. All of our K_e data is extracted with $V_B \lesssim 30$ mV. The solid line in panel (d) is a power law fit $T_e = 100 + BV_B^x$, and we find $x = 2.02 \pm 0.04$, as expected for Joule heating over a small T_e range.

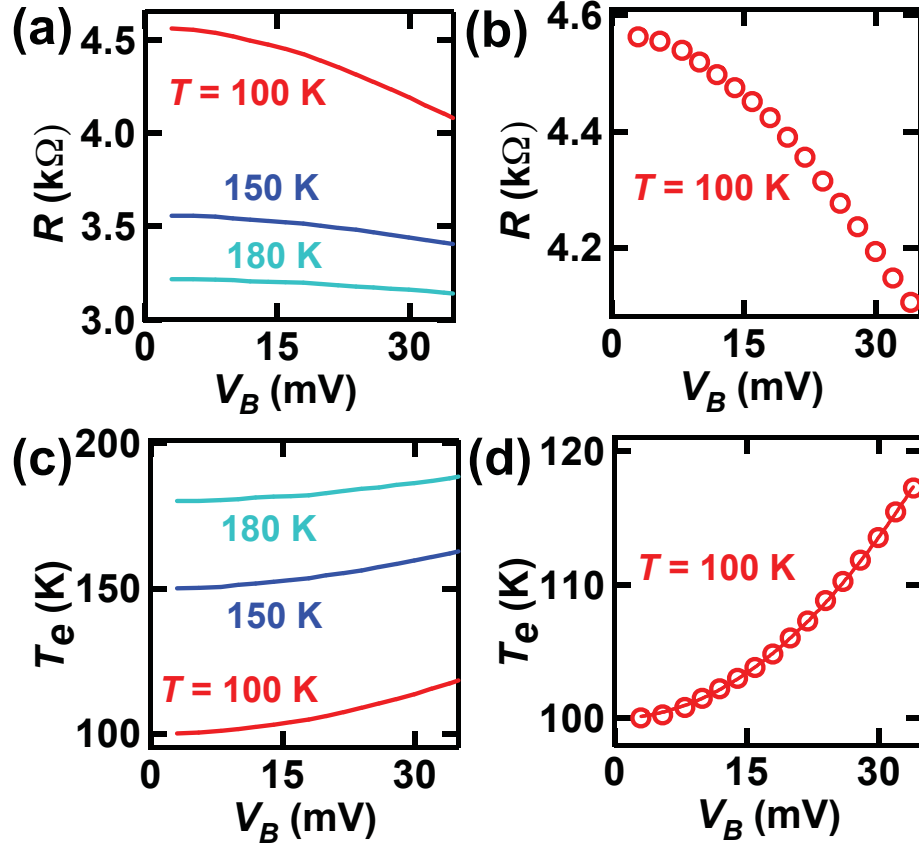


Figure 3.8: Electron heating for Sample C. (a) R vs V_B at $T = 100, 150, 180$ K for Device C at $V_G = 0.0$ V $\approx V_D$. (b) Zoom-in on the 100 K data. Joule heating due to V_B raises the flake's average T_e above T . T_e is extracted using Fig. 3.4(a). Panels (c) and (d) show T_e vs V_B in Sample B at a few T , and at $T = 100$ K respectively. All of our K_e data is extracted with $V_B \lesssim 30$ mV. The solid line in panel (d) is a power law fit $T_e = 100 + BV_B^x$, and we find $x = 2.00 \pm 0.02$, as expected for Joule heating over a small T_e range.

3.2.3 Electron-electron scattering length

The electron-electron (inelastic) mean-free path, l_{ee} , in graphene was calculated by Li and Das Sarma [85] for various charge densities and temperatures, but for disorder free samples (ballistic transport). They found that l_{ee} decreases rapidly with T . For instance, in their Fig. 3(a) they calculated l_{ee} in suspended graphene at a charge density $n = 10^{10} \text{ cm}^{-2}$ which is close to the density in our devices (1.7 and $2.1 \times 10^{10} \text{ cm}^{-2}$). They found that $l_{ee} \approx 200 \text{ nm}$ at $T = 100 \text{ K}$. This is shorter than our devices, but only by a factor of 2 or 3. However, the l_{ee} in our devices should be much shorter due to disorder (measured from the width of the $R - V_G$ peak). Quoting Li and Das Sarma (conclusion): “It is well known that disorder has qualitative and quantitative effects on the inelastic mean free path and the phase breaking length, in general, suppressing the mean free path substantially from its ballistic limit.”

Another piece of evidence supporting that l_{ee} in our devices is much shorter than their total length is shown in Fig. 3.9 where we observe a small, but clearly visible, mesoscopic oscillation in the $G - V_G$ characteristic of Sample B at $T = 17 \text{ K}$. This oscillation disappears as T is raised above $T = 30 \text{ K}$. Mesoscopic oscillations (quantum interferences) are expected when l_{ee} is much longer than l_{e-imp} , and should disappear when $l_{ee} \lesssim l_{e-imp}$. Thus, Fig. 3.9 suggests that $l_{ee} \lesssim l_{e-imp}$ at $T \gtrsim 30 \text{ K}$. Since l_{e-imp} is significantly shorter than the size of the sample (see section 3.2.1), we expect the same to hold for l_{ee} . We do not observe mesoscopic fluctuations in our 3 devices over the T range where we report K_e . We also note that Du et al. [80] studied samples which are very similar to ours (length of 0.5 micron, suspended, current annealed, and showing similar mobility and elastic mean-free path), and also observed that mesoscopic fluctuations disappeared above $T \approx 20 - 40 \text{ K}$ (see their Fig. 3(c)). Finally, the agreement between our experimentally extracted and theoretically calculated K_e , over the entire T range studied, strongly supports a well defined $T_e(x)$.

We also note that since the graphene which is buried under the gold contacts was not current annealed, it is much more disordered than the suspended portion of the device. This large increase in disorder should lead to a reduced l_{ee} under the gold, implying that $l_{ee-under} < l_{ee-exposed}$.

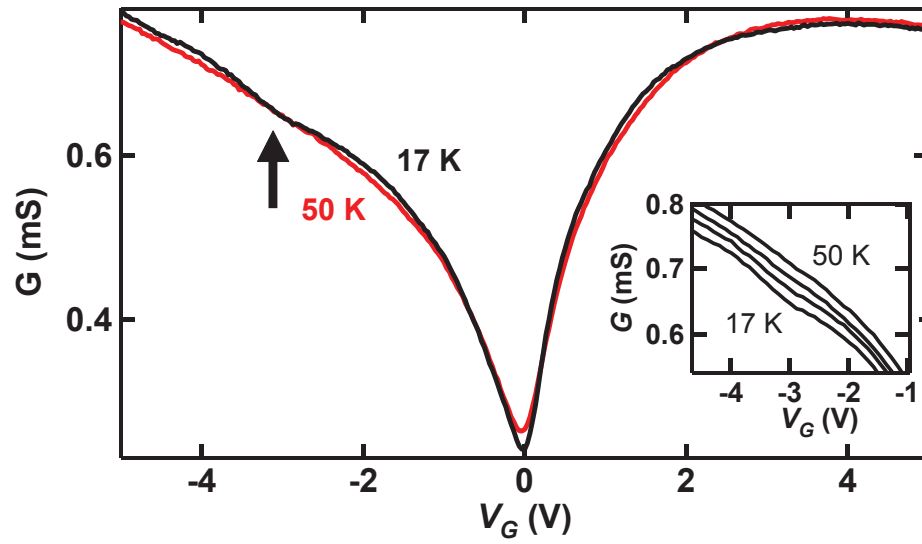


Figure 3.9: Mesoscopic conductance oscillation in Sample B. G vs V_G at $T = 17$ and 50 K for Device B. The black arrow indicates a conductance oscillation which disappears at $T > 30$ K, suggesting that the inelastic mean-free path (due to $e - e$ collisions) is comparable to the elastic mfp (e -impurity collisions) in this sample around 30 K. The inset shows G vs V_G at several T between 17 K and 50 K, the curves are offset for clarity.

3.3 Extracting Electronic Thermal Conductivity (K_e) in Intrinsic Graphene

Since our devices are much wider than the elastic mean-free path (section 3.2.1), the effect of their edges on transport should be small. We use a 1-d heat equation to extract K_e in our devices:

$$K_e \frac{d^2 T_e}{dx^2} + Q = 0 \quad (3.6)$$

where $Q = RI^2/WLh$ is the Joule heating power per unit volume, W the width, L the length, and $h = 0.335$ nm the thickness. Using boundary conditions $T_e = T$ at the two ends (contacts) of the flake, we find

$$T_e(x) = T + \frac{LQx - Qx^2}{2K_e} \quad (3.7)$$

Averaging over the length we find,

$$T_e = \frac{1}{L} \int_0^L T_e(x) dx = T + \frac{QL^2}{12K_e} \quad (3.8)$$

Finally,

$$K_e = \frac{QL^2}{12\Delta T} \quad (3.9)$$

where $\Delta T = T_e - T$. Using R and I from Fig. 3.6 and similar plots, for $\Delta T = 1, 2$ and 5 K we extract K_e vs T_e in Fig. 3.10(a) for Sample A. Fig. 3.10(b) shows K_e vs T_e for all three samples for $\Delta T = 5$ K. Data in Fig. 3.10 show a strong K_e dependence on T_e ranging from roughly 0.5 W/K.m at 20 K to 11 W/K.m at 300 K. The T_e range is limited to the region where we have accurate thermometry (Fig. 3.4), up to ≈ 200 K for A and C, and 300 K for B. Error bars representing the total uncertainty on K_e are shown for the $\Delta T = 5$ K data (see section 3.3.1). If the V_B needed to apply ΔT were to dope significantly the samples, it could affect the measured K_e . Using

$n_{tot}(T)$ (Eq. 4.2) [83], we define an effective chemical potential:

$$\mu_{eff}(T) = \hbar v_F \sqrt{\pi n_{tot}(T)} \quad (3.10)$$

For instance, at $T = 100$ K, $\mu_{eff}(100 \text{ K}) = 18, 18.4$ and 19.5 meV respectively for the three devices. The V_B necessary to achieve $\Delta T \leq 5$ K in Fig. 3.10 is always smaller than $\mu_{eff}(T)$. We only observe a change in the extracted K_e values when ΔT exceeds 8 K, and $V_B > \mu_{eff}(T)$. Thus V_B does not affect our K_e , with the caveat that we cannot extract K_e precisely at $n = 0$. The thermoelectric voltages in our devices are negligible compared to V_B [86, 87].

3.3.1 Error analysis

To calculate the uncertainties on the values extracted for K_e , using equation 4.4 below, we account for four sources of uncertainty: error on the sample's length, ΔL , width ΔW , resistance ΔR due to the contact resistance R_c , and extracted electronic temperature ΔT_e . We estimate $\Delta L \approx 40$ nm, $\Delta W \approx 50$ nm, $\Delta R = R_c = R_o$ (which is an upper limit since $R_o = R_c +$ resistance from neutral scatterers), and ΔT_e = the standard deviation of T_e from the fit of T_e vs V_B as shown in Figs. 3.6(d), 3.7(d) and 3.8(d). We note that the uncertainty ΔT_e is inversely proportional to the slope of the calibration curve, Figure 3.4, at T_e .

$$K_e = \frac{RI^2L}{12Wh\Delta T} \quad (3.11)$$

The error on the measured current I is negligible compared to the other sources of error, and the thickness $h = 0.335$ nm is a standard value used by all experiments and theory. Note that $\Delta T = T_e - T$ where T is the cryostat temperature. The error on T is about 0.1 K and comes from the accuracy of our temperature controller, thus the error on ΔT is roughly $\Delta T_e + 0.1$ K. We calculate ΔK_e using the equation:

$$\frac{\Delta K_e}{K_e} = \sqrt{\left(\frac{\Delta L}{L}\right)^2 + \left(\frac{\Delta W}{W}\right)^2 + \left(\frac{\Delta R}{R}\right)^2 + \left(\frac{\Delta(\Delta T)}{\Delta T}\right)^2} \quad (3.12)$$

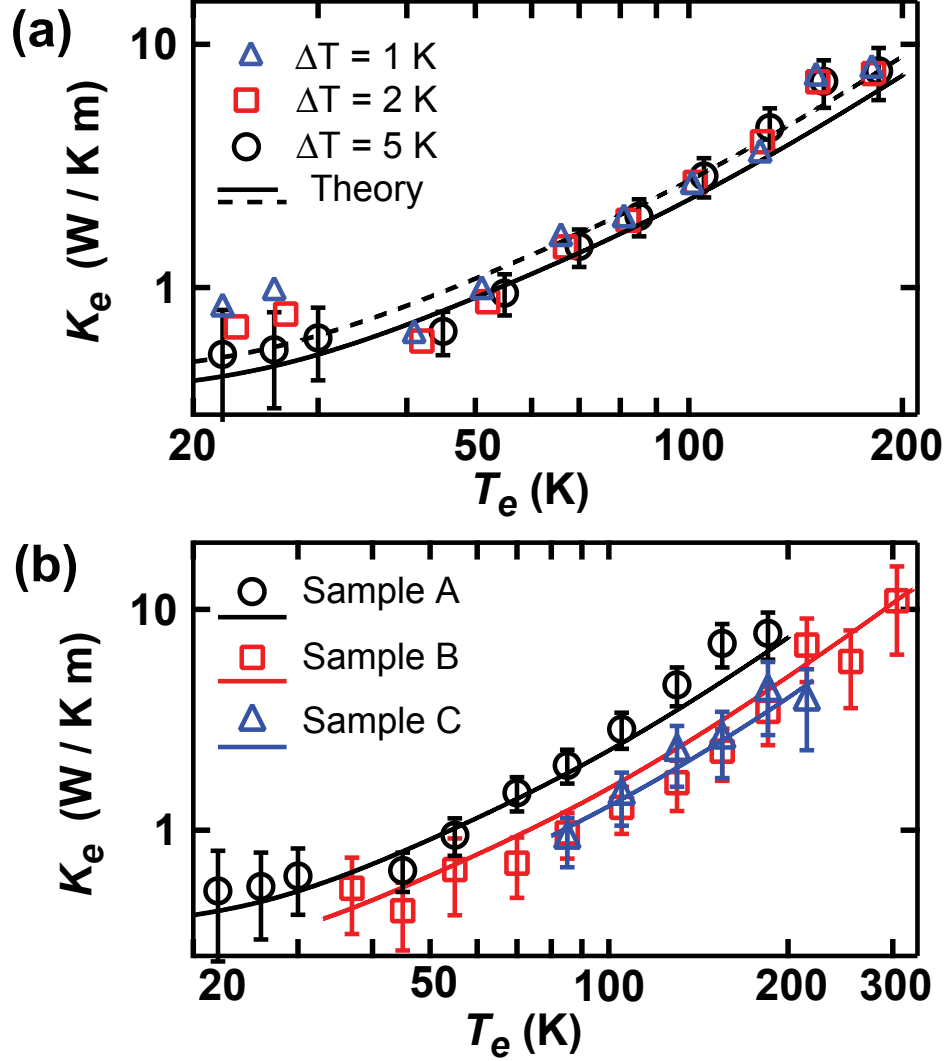


Figure 3.10: Electronic thermal conductivity, K_e , in the quasi-intrinsic regime, $n_{tot,T=0} \approx 1.7$ (Samples A, B) and 2.1 (Sample C) $\times 10^{10} \text{ cm}^{-2}$. (a) K_e vs T_e for $\Delta T = T_e - T = 1, 2$ and 5 K for Sample A. The solid line is a theoretical calculation of K_{e-th} . The dashed line shows the same calculation with a contact resistance $R_c = R_{o-Dirac}$. The error bars are shown for the $\Delta T = 5$ K data. (b) K_e vs T_e for $\Delta T = 5$ K for Samples A, B and C, and K_{e-th} for each sample.

The calculated errors are shown in Fig. 3.10. For example, the error bars $\Delta K_e/K_e$ at $T = 100$ K are 18.3%, 24.1% and 25.8% from Samples A, B, and C.

3.4 K_e for Diffusing Dirac Quasiparticles in 2D

We compare our data with the usual model for diffusing particles in 2-dimensions:

$$K_{e-th} = \frac{1}{2} C v l \quad (3.13)$$

If the heat flow is due to charge carriers, then the specific heat is $C = C_e$, the velocity is $v_F = 10^6$ m/s, and the mean free path l is the same as for charge transport. We find (section 3.2.1), l_{A-avg} , l_{B-avg} , and $l_{C-avg} = 71$ (85), 47 (59), and 37 (51) nm on average over the T_e range with $R_c = 0$ ($R_{o-Dirac}$). We calculate the charge carrier specific heat, C_e , using the density of states for graphene and the Fermi-Dirac distribution:

$$C_e = \frac{dU_e}{dT} \quad (3.14)$$

where the total energy of the charged quasiparticles, U_e , is calculated from the density of states and Dirac statistic for quasiparticles in graphene as,

$$U_e = \int_0^\infty \frac{2\epsilon^2}{\pi(\hbar v_F)^2} \frac{1}{e^{(\frac{\epsilon-\mu}{kT})} + 1} d\epsilon - \int_{-\infty}^0 \frac{2\epsilon^2}{\pi(\hbar v_F)^2} \left(\frac{1}{e^{(\frac{\epsilon-\mu}{kT})} + 1} - 1 \right) d\epsilon \quad (3.15)$$

where $\mu = \mu_{eff}(T = 0) = \hbar v_F \sqrt{\pi n_{tot}(T = 0)} = 14.8, 15.4$ and 17.1 meV are the effective chemical potential for Samples A, B and C respectively. n_{tot} is defined above in Eq. 4.2 and includes both the gate induced charge density and the impurity induced density.

We plot K_{e-th} in Figs. 3.10(a) and 3.10(b) as solid lines with $R_c = 0$. They capture the quantitative T_e dependence of our K_e data. The K_e data points are in good quantitative agreement with the calculated values for all three samples, and especially for Samples A and C. The dashed line in Fig. 3.10(a) shows K_{e-th} if we use $R_c = R_{o-Dirac}$. If we account for R_c , i.e., smaller Q , K_e changes by the same magnitude as K_{e-th} but in the opposite direction (not shown for clarity). The

quantitative agreement between data and theory is not as accurate for Sample B since its R is smaller than for Samples A and C, and the impact of R_c could be bigger. The data and calculations shown in Fig. 3.10(b) with $R_c = 0$ are within 20%, 30%, and 15 % of each other for Samples A, B and C. If we include $R_c = R_o$, which overestimates the effect due to R_c , the agreement between the data and theory for Sample B is at worst within a factor of 2, and much better for Samples A and C. We fit a power law expression $K_e \propto T^p$ over $T_e = 45 - 185$ K for Samples A and B, and find $p = 1.73 \pm 0.15$ and 1.63 ± 0.13 which is very close to the fit on K_{e-th} , $p_{th} = 1.62$ and 1.59 . This agreement is preserved even if we let $R_c = R_o$. As expected p_{th} goes to 2 when $\mu/kT \ll 1$. We conclude that the K_e data is consistent with heat being carried by particles moving with the v_F and l of the charge carriers. The magnitude of K_e reaches ≈ 11 W / K.m at 300 K with $n_{tot,T=0} \approx 1.7 - 2.1 \times 10^{10} \text{ cm}^{-2}$.

A condition to make reliable K_e measurements is that all of the Joule heat remains in the carriers until they diffuse to the leads. Both experiments and theory confirm that the electron-phonon energy transfer in high-mobility graphene, at low V_B , is very small below 300 K [16, 17, 24, 25], and decreases at lower T and n . In our devices, we extract a cooling length for hot electrons (section 3.4.1 below), $\xi \approx 100$ to $10 \mu\text{m}$ for $T_e = 20$ to 300 K. Since ξ is much longer than L , and V_B below the energy of optical phonons, we expect T_e and T to be decoupled in our devices when $V_B \neq 0$, and all of the Joule heat to be carried to the contacts by charge carriers. Indeed, the K_e we measure are two to three orders of magnitude lower than the reported phonon thermal conductivity K_p in graphene [44, 51].

3.4.1 Electron cooling length estimate

Bistritzer and MacDonald [57] calculated the electron-acoustic phonon scattering rate for graphene in the intrinsic regime. They found,

$$\gamma_{e-ac} = 1.18 \times 10^3 D^2 (\text{meV}^2.s)^{-1} \times (k_B T_e)^2 \quad (3.16)$$

where D is the deformation potential measured in eV. The value of is not well known and has been reported in the range of 10 - 50 eV. We set $D = 20$ eV, as in Ref. [57] and most other theoretical work. We find $\gamma_{e-ac} = 1.7 \times 10^6 - 1.2 \times 10^8 \text{ s}^{-1}$ for Sample

A over the studied T_e range, 3.2×10^6 - 3.3×10^8 s⁻¹ for Sample B, and 2.4×10^7 - 1.6×10^8 s⁻¹ for Sample C. Based on these scattering rates, we can estimate the electron cooling length as

$$\xi = \sqrt{\frac{K_e}{\gamma_{e-ac} C_e}} \quad (3.17)$$

where K_e is the measured heat conductivity in Fig. 3.10, and C_e the calculated specific heat from Eq. 3.14. We find $\xi = 150$ to 14 μm for Sample A, $\xi = 74$ to 8.5 μm for Sample B, and $\xi = 27$ to 11 μm for sample C over the T_e range in Fig. 3.10. These values are always much larger than the length of the devices, 650 nm for A and 400 nm for B and C, which ensures that most of the Joule heating stays in the charge carriers until they reach the gold contacts.

3.5 Conclusion and Outlook

In summary, we fabricated high quality suspended monolayer graphene devices, developed self-thermometry and self-heating methods to extract and control T_e , and the electronic thermal conductivity in graphene. We extracted K_e in the quasi-intrinsic regime, $n_{tot,T=0} \approx 1.7$ - 2.1×10^{10} cm⁻², from $T_e = 20$ K to 300 K. The K_e data in three different devices are in very good agreement with a model where heat is carried by diffusing Dirac quasiparticles. Our results provide evidence that the dominant electron cooling mechanism in intrinsic sub-micron graphene devices below 300 K is hot-electron diffusion to the leads. The theoretical model we use naturally leads to the Wiedemann-Franz relation in the doped-regime and suggests that it should be obeyed in graphene. This will be discussed in the following chapter (Ch. 4). We will present data from the doped regime (electron and hole doping). We will test Wiedemann-Franz law and also study how K_e changes with carrier density in graphene.

Chapter 4

Wiedemann-Franz Relation and Thermal-Transistor Effect in Graphene

We extract experimentally the electronic thermal conductivity, K_e , in suspended graphene that we dope using a back-gate electrode. We make use of two-point dc electron transport at low bias voltages and intermediate temperatures (50 - 160 K), where the electron and lattice temperatures are decoupled. The thermal conductivity is proportional to the charge conductivity times the temperature, confirming that the Wiedemann-Franz relation is obeyed in suspended graphene. We extract an estimate of the Lorenz coefficient as 1.1 to $1.7 \times 10^{-8} \text{ W } \Omega \text{K}^{-2}$. K_e shows a transistor effect and can be tuned with the back-gate by more than a factor of 2 as the charge carrier density ranges from ≈ 0.5 to $1.8 \times 10^{11} \text{cm}^{-2}$. The work presented in this chapter is adapted from the following publication: “Wiedemann-Franz Relation and Thermal-Transistor Effect in Suspended Graphene”, Serap Yiğen and Alexandre Champagne, Nano Letters 14, 289 (2014) [15].

4.1 Introduction

Graphene’s electronic thermal conductivity, K_e , describes how easily Dirac charge carriers (electron and hole quasiparticles) can carry energy. In low-disorder graphene at moderate temperatures ($< 200 - 300 \text{ K}$), the energy transfer rate between charge

carriers and acoustic phonons is extremely slow [14, 16, 17, 24, 45, 58]. Thus, K_e impacts how a hot electron cools down, and the efficiency of charge harvesting in graphene optoelectronic devices [16–18]. Moreover, understanding and controlling K_e could help develop graphene bolometers capable of detecting single terahertz photons [45, 46]. There are theoretical calculations of K_e [77, 88, 89], and recent experimental data near the charge neutrality point (CNP) in clean suspended graphene [14] and in disordered samples at very low temperatures [45, 46]. However, a detailed mapping of K_e vs charge density at intermediate temperatures is lacking. Understanding how K_e in clean (suspended) graphene depends on charge density, n , and the electronic temperature, T_e , is crucial for applications. An important fundamental question is whether the Wiedemann-Franz (WF) law, $K_e = \sigma L T_e$ where σ is the charge conductivity, and L is the Lorenz number, is obeyed in graphene. In clean graphene at low charge densities (hydrodynamic regime), strong electron-electron interactions could lead to departures from the generalized WF law [88, 89].

We report K_e in monolayer graphene extracted from carefully calibrated dc electron transport measurements following a method we previously discussed (chapter 3 and [14]). We study a temperature range of $T = 50 - 160$ K, where the electron and lattice temperatures are very well decoupled in low-disorder graphene [14, 16, 17, 24, 45, 58], over a charge density range of ≈ 0.5 to $1.8 \times 10^{11} \text{cm}^{-2}$. We extract data in the hole and electron doped regimes from two high-mobility suspended devices. The extracted K_e are compared with predictions from the WF law. The agreement between the WF relation and measurements is very good for both devices over the n range studied and T up to 160 K. The value of L is $\approx 0.5 - 0.7 L_o$, where L_o is the Lorenz factor for metals. We observe a sudden jump in the extracted thermal conductivity above 160 K which is consistent with the onset of strong coupling between electrons and acoustic phonons [58]. Finally, we observe a thermal transistor effect consistent with the WF prediction, where K_e can be tuned by more than a factor of 2 with a back-gate voltage, V_G , ranging up to ± 5 V. Throughout the text we use T to designate the lattice (cryostat) temperature, and T_e for the average electron temperature in the suspended devices. At very low bias, $|V_B| \leq 1$ mV, $T = T_e$.

Figure 4.1(a) and (b) shows dc two-point resistance data, $R = V_B/I$, versus gate voltage, V_G , which controls the charge density, n_G (upper axis) for Samples A and C

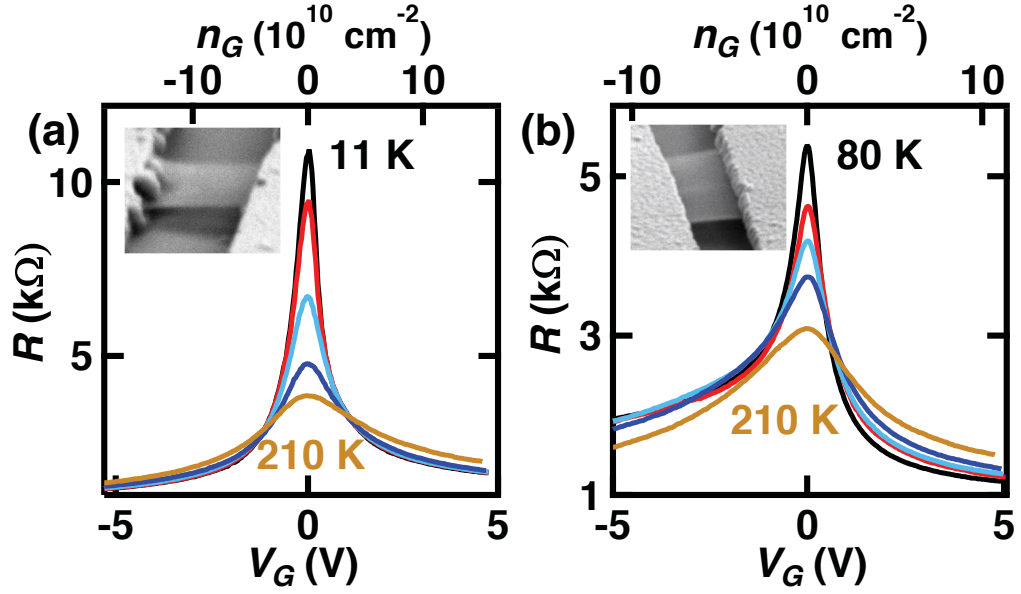


Figure 4.1: Suspended and annealed graphene devices. (a) R of Sample A vs. gate voltage, V_G , at $T_e = T = 11, 50, 100, 150$ and 210 K, and $V_B = 0.5$ mV. (b) $R - V_G$ data for Sample C at $T_e = T = 80, 100, 125, 150$ and 210 K, and $V_B = 5$ mV. The insets show tilted SEM images of the suspended graphene transistors: Sample A (650 nm long), and a device identical to Sample C (400 nm long). For clarity, the data curves in (a) and (b) are slightly shifted along the V_G axis so that all the maxima line up at $V_G = 0$, the shifts in (a) range from -0.3 to -0.45 V, and in (b) from 0 to 0.2 V.

respectively. From the width of the R maximum at low T , we extract a half-width-half-maximum, HWHM, of 0.45 and 0.95 V for Samples A and C. These HWHMs correspond to an impurity induced charge density of $n^* \approx 1.5$ and $2.1 \times 10^{10} \text{ cm}^{-2}$. For clarity, the data in Fig. 4.1 is slightly shifted along the V_G axis so that all the maxima (Dirac points) line up at $V_G = 0$, the shifts in Fig. 4.1(a) range from -0.3 to -0.45 V at various T , and in Fig. 4.1(b) from 0 to 0.2 V. The insets in Fig. 4.1 show scanning electron microscope (SEM) tilted images of Sample A and a sample identical to Sample C.

We confirmed, using optical contrast and Raman spectroscopy, that both samples are single-layer graphene. Sample A is 650 nm long, 675 nm wide, and suspended 140 ± 10 nm above the substrate (AFM measurement) which consists of 100 ± 2 nm of SiO_2 (ellipsometry measurement) on degenerately-doped Si which is used as a back-gate electrode. Sample C is 400 nm long, $0.97 \mu\text{m}$ wide, and suspended 227 ± 10 nm above a 74 ± 2 nm SiO_2 film on Si. To prepare the samples, we followed the fabrication procedure that is presented in Chapter 2. We used exfoliated graphene, and standard e-beam lithography to define Ti(5nm)/Au(80nm) contacts. The samples were suspended with a wet BOE etch such that their only thermal connection was to the gold contacts. We annealed the devices using Joule heating *in situ* by flowing a large current in the devices [14,40] (up to 540 and $837 \mu\text{A}$ for Samples A and C). Annealing and all subsequent measurements were done under high vacuum, $\leq 10^{-6}$ Torr.

4.1.1 Upper bond for contact resistance

To minimize contact resistance, R_c , the devices were fabricated with large contact areas between the gold electrodes and graphene crystals, ranging from 1.1 to $3 \mu\text{m}^2$ per contact. An upper bound for series resistance, R_o , which includes both the contact resistance, R_c , and the resistance from neutral scatterers, can be extracted from the two-point $R - V_G$ curves [90] in Fig. 4.1 (similar to section 3.1.1). We fit the data with the expression

$$R = R_o + \left(\frac{1}{\frac{n_{GE}\mu W}{\ell} + G_{CNP}} \right) \quad (4.1)$$

where R_o is the resistance due to neutral scatterers plus R_c , ℓ is the length of the device, W the width, n_G the charge density induced by V_G , μ the mobility, and e the electron's charge. We fit the data at $T = T_e = 100$ K, and for $(V_G - V_D) > 1.3$ V to avoid the thermal smearing around the Dirac point, V_D . The fit for the hole (electron) regime is shown as a light blue (red) dashed line in Fig. 3.3(a). The extracted mobility for Sample A in the doped regime is $\mu \approx 5.5 \times 10^4 \text{ cm}^2 / \text{V.s}$ at 100 K. 3.3(b) shows the conductance, $G = 1/R$, for Sample A before the series resistance R_o is subtracted (black line) and after R_o is subtracted for the hole (blue) and electron (red) doped data. The corrected conductance depends linearly on the gate induced charge density, n_G .

The extracted series resistances for Sample A are $R_{o-h} \approx 477 \pm 53$ and $R_{o-e} \approx 944 \pm 80 \text{ } \Omega$ for hole and electron doping, respectively. The difference between R_{o-h} and R_{o-e} is understood as an additional $p - n$ barrier for the electron due to doping from the gold electrodes [42]. For Sample C, we find $R_{o-h} = 1563 \text{ } \Omega$ and $R_{o-e} = 812 \text{ } \Omega$. We note that series resistance is smallest for hole doping in Sample A and for electron doping in Sample C. In annealed samples, oxygen desorbs from the gold contacts and changes the work function of the electrodes. This means that graphene under the gold electrodes can be either electron doped or hole doped depending on the thoroughness of the contact annealing [42,91,92]. To minimize the effect of R_c on our data, we study the lowest resistance side of the Dirac point for each Sample. This allows us to study hole transport in Sample A and electron transport in Sample C. Since R_o includes both R_c and the resistance due to neutral scatterers in the channel, we conservatively set $R_c = R_o/2$ with an uncertainty ranging up to $R_{c-max} = R_o$, and down to $R_{c-min} = \text{lowest reported resistance for Au/graphene [93]}$ with similar n , which is $\approx 100 \text{ } \Omega.\mu\text{m}^2$. Thus, in the following data analysis we use for Samples A and C, $R_{c-A} = 239 \pm_{120}^{239}$ and $R_{c-C} = 406 \pm_{281}^{406}$. We extract a conservative estimate of the charge carrier mobility in our devices, over the n and T_e range studied, as $\mu = \sigma/(n_{tot}e) \approx 3.5 \times 10^4 \text{ cm}^2/\text{V.s}$, where n_{tot} is the total carrier density including the gate, impurity and thermal doping [14,83]:

$$n_{tot} = n + p = \sqrt{n_G^2 + 4 \left[\left(\frac{n^*}{2} \right)^2 + n_{th}^2 \right]} \quad (4.2)$$

where n_G is the charge density induced by the gate electrode. For instance, for Sample A at 100 K and $V_G = -5.3 \text{ V}$ ($n_G = -1.8 \times 10^{11} \text{ cm}^{-2}$) we find $n_{tot}(100$

K) $\approx n_G$ and for Sample C at 100 K and $V_G = 5.0$ V ($n_G = 1.1 \times 10^{11} \text{ cm}^{-2}$) we find $n_{tot}(100 \text{ K}) \approx 1.15 \times 10^{11} \text{ cm}^{-2}$. We calculate a realistic estimate of the charge carrier mobility by using $\mu = \frac{\sigma}{n_{tot}e}$, where σ is the charge conductivity. At $T = 100$ K, $\mu = 3.6$ and $2.9 \times 10^4 \text{ cm}^2 / \text{V.s}$ using $R_c = R_o/2$ for Samples A ($V_G = -5.3$ V) and C ($V_G = 5.0$ V) respectively. The extracted mobility decreases with T . From the mobility, we extract the mean-free path of the carriers as,

$$l = \sqrt{\frac{n_{tot}}{\pi}} \frac{h\mu}{2e} \quad (4.3)$$

At $T = 100$ K, we find $l = 177$ and 114 nm for A ($V_G = -5.3$ V) and C ($V_G = 5.0$ V), which is several times shorter than the length and width of the samples ($650 \text{ nm} \times 675 \text{ nm}$ for A, and $400 \text{ nm} \times 970 \text{ nm}$ for C).

Based on the reported thermal conductance of Au/Ti/Graphene and Graphene/SiO₂ interfaces [81], the thermal resistance of the contacts can safely be neglected [79] compared to our K_e data presented below.

4.2 Extracting Electronic Thermal Conductivity (K_e) in Doped Graphene

Figure 4.2 summarizes our approach to extract K_e in suspended high-mobility graphene, whose details we previously discussed (chapter 3 and [14]). We repeat some of the discussion of our methods because the charge densities studied here are much higher than in Ref. [14], which leads to several important changes. Figure 4.2(a)-(b) presents how we monitor the charged quasiparticle temperature in our devices by monitoring R , and Fig.4.2(c)-(d) shows how we can controllably heat-up these quasiparticles at a temperature slightly above the contacts' temperature via Joule heating. By combining these two capabilities and using the heat equation, we will later extract K_e vs T and n .

Figure 4.2(a) shows the two-point dc R vs cryostat temperature, T , calibration curves for Sample A (circles, left axis), and Sample C (squares, right axis) which are respectively hole-doped with a gate-induced density of $n_G = -1.8 \times 10^{11} \text{ cm}^{-2}$ and electron-doped with $n_G = 1.1 \times 10^{11} \text{ cm}^{-2}$. $R = V_B/I$ is extracted from the slope of the $I - V_B$ data as shown in the inset of Fig.4.2(a). Note that for ± 1 mV bias

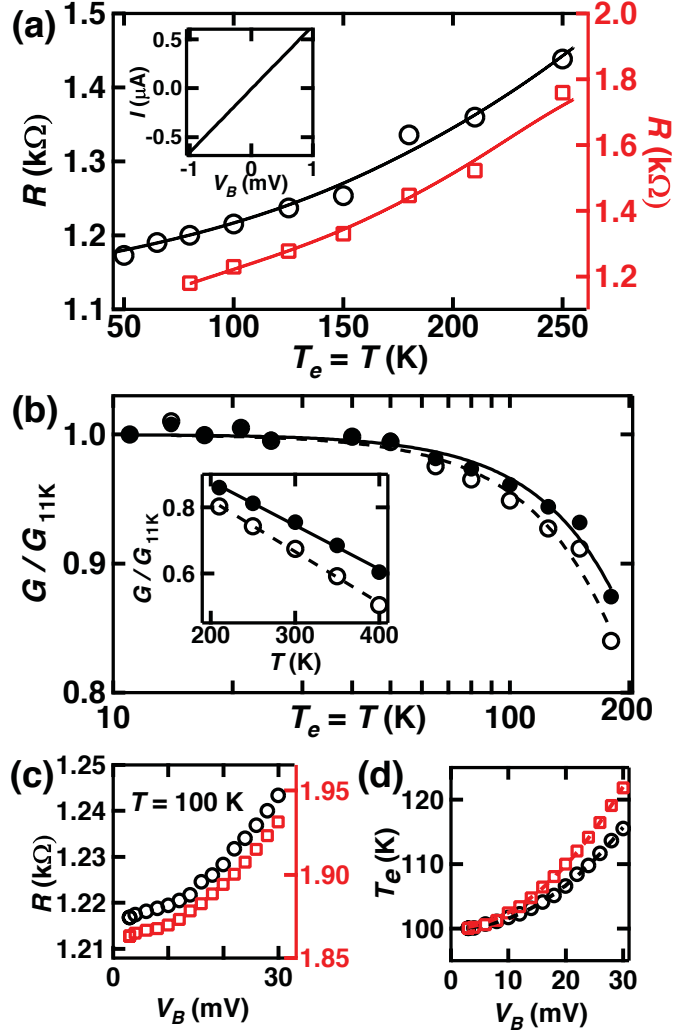


Figure 4.2: Electron thermometry and electron Joule heating. (a) R vs T_e in Sample A (circles, left axis) and Sample C (squares, right axis), respectively hole ($n_G = -1.8 \times 10^{11} \text{ cm}^{-2}$) and electron doped ($n_G = 1.1 \times 10^{11} \text{ cm}^{-2}$). The solid lines are numerically interpolated curves used for thermometry. Inset: example of $I - V_B$ data at 100 K for Sample A whose slope is used to extract R , $|V_B| < 1$ mV such that $T_e = T$. (b) Relative conductance G/G_{11K} of Sample A vs $T_e = T$. The solid circles show the raw two-point data, and the open circles the data using $R_c = 239 \Omega$. The solid and dashed lines are power law fits consistent with charge impurity scattering. Inset: G/G_{11K} of Sample A at high T showing a linear decrease in R consistent with acoustic phonon scattering. (c) R vs V_B data for Sample A at $T = 100$ K, and $n_G = -1.8$ (circles, left axis) and -0.8 (squares, right axis) $\times 10^{11} \text{ cm}^{-2}$ (i.e. $V_G = -5.3$ and -2.3 V). Joule heating due to V_B raises the flake's average T_e above T . (d) T_e vs V_B in Sample A extracted from (c) using the calibration in (a) and similar curves.

no Joule heating effect is present and $T_e = T$. As showed in Fig. 4.2(a)-inset, the $I - V_B$ characteristics at very low V_B are precisely linear (no Joule heating). In which case $V_B/I = dV_B/dI$, and we use the slope to extract R to avoid an error due to a very small (experimental) offset in V_B (few 10s of micro-Volt). At higher bias, this small offset is negligible and we can safely use $R = V_B/I$. In Figure 4.2(c), T_e is not constant versus V_B due to Joule heating, thus dV_B/dI also contains information about how quickly the temperature is changing with V_B , rather than only the temperature at one specific V_B value. Since ΔT is small, we find no significant quantitative difference in our results using either dV_B/dI or V_B/I to extract T_e , but the correct quantity which represents T_e is V_B/I . The T_e dependence of the data shows a metallic behavior with R increasing with T_e . The interpolated lines in Fig.4.2(a), and similar curves, will be used as secondary thermometry curves to monitor T_e in the devices.

Figure 4.2(b) shows the relative conductance $G(T)/G_{11K}$ for Sample A extracted from Fig.4.2(a) and similar data. The solid circles show the raw two-point data, and the open circles the data after subtracting $R_c = R_o/2$. The T dependence of $G = 1/R$ in graphene, at modest charge density, is strongly dependent on the type of charge transport. We fit the data in Fig. 4.2(b) with a function $G/G_{11K} = 1 - AT^p$, and extract $p = 2.1 \pm 0.2$ for both curves. This T -dependence strongly supports diffusive charge transport dominated by long-range charge impurities, as reported in previous experiments on high-mobility devices [40,76,80] and expected theoretically [58]. The inset of Fig. 4.2(b) shows that G/G_{11K} of Sample A decreases linearly for $T \geq 200$ K, which suggests a relatively strong acoustic phonon scattering above this temperature, as expected theoretically [58]. Sample C shows a qualitatively identical behavior of its R vs T in Fig. 4.2(a), but the absence of low temperature data proscribes an accurate fit of its dependence. We will focus our measurements on the $T < 200$ K range (see Eq. 4.3), where both samples are in the diffusive regime with scattering predominantly due to charged impurities. This scattering is elastic, and its T_e dependence (used for thermometry) comes mostly from the temperature dependence of its screening [76].

Electron-electron scattering between charge carriers is inelastic. By applying a V_B one can inject high-energy carriers in the suspended device which then thermalize with the carriers in the sample and raise T_e in the suspended graphene relative to the temperature in the gold contacts. Note that when writing T_e , we always refer to the *average* temperature of charged quasiparticles in our devices. We demonstrate

controlled Joule self-heating of the electrons to apply a thermal bias $\Delta T = T_e - T$ between the suspended graphene and the electrodes (cryostat temperature). Figure 4.2(c) shows R vs V_B for Sample A at $T = 100$ K and $n_G = -1.8 \times 10^{11}$ (circles, left axis) and $-0.8 \times 10^{11} \text{ cm}^{-2}$ (squares, right axis). Sample C data is shown in Fig. 4.3.

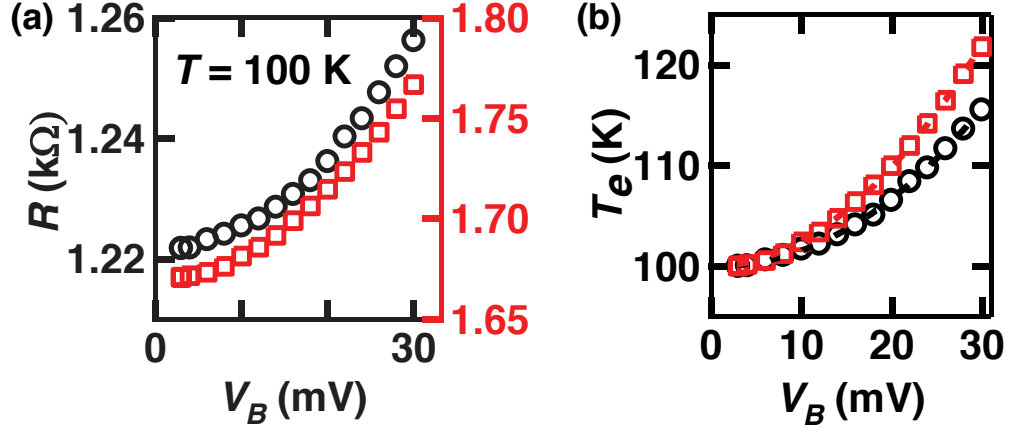


Figure 4.3: Electron heating in Sample C. (a) R vs V_B at $T = 100$ K for device C at $V_G = 5$ V (circle data, $n_{tot,T=0} \approx 1.1 \times 10^{11} \text{ cm}^{-2}$) and $V_G = 2$ V (square data, $n_{tot,T=0} \approx 0.5 \times 10^{11} \text{ cm}^{-2}$). Joule heating due to V_B raises the flake's average T_e above the cryostat T . (b) T_e vs V_B in Sample C at $T = 100$ K extracted from (a) using the thermometry curves as in Fig. 4.2(a). All of our K_e data is extracted with $V_B \lesssim 27$ mV. The solid lines in panel (b) are power law fit $T_e = 100 + BV_B^x$, and we find $x = 2.10 \pm 0.03$ and 1.99 ± 0.02 , which is very close the expected $x = 2$ for Joule heating over a small T_e range.

R increases monotonically with increasing V_B , at all T . We restrict our measurements to $V_B \leq 27$ meV. We have previously argued (chapter 3 and [14]) that in our high-mobility devices, under such low V_B and in the T range we study, the change in R is caused by Joule heating of the charge carriers [14, 24]. Using the curves, R vs T_e and R vs V_B , we extract T_e vs V_B as shown for Sample A in Fig. 4.2(d). We fit a power law (dashed lines) $T_e = 100 + BV_B^x$, and find $x = 1.93 \pm 0.04$ for both data sets, as expected for Joule heating where $T_e \propto V_B^2$. Figures 4.2(d) and 4.3(b) show that the accuracy with which T_e can be extracted is much better than 1 K. The smooth dependence of T_e on V_B at all T is consistent with electrons having a well defined temperature as predicted by calculations of the $e - e$ collision length [85] (see section 3.4.1), and confirmed by the K_e data shown below.

We use a 1-d heat equation (Section 3.3 and [14]) to extract K_e in our devices, and find

$$K_e = \frac{Q\ell^2}{12\Delta T} \quad (4.4)$$

where $\Delta T = T_e - T$, $Q = RI^2/W\ell h$ is the Joule heating power per unit volume, W the width, ℓ the length, $h = 0.335$ nm the thickness, and T_e is the electronic temperature averaged over ℓ . In Fig. 4.4(a)-(b) we plot K_e vs T_e for Samples A and C for $\Delta T = 10$ K, where the circle, square and triangle data show K_e at $n_{tot,T=0} \approx -1.8, -1.1, -0.8 \times 10^{11} \text{ cm}^{-2}$ for Sample A, and $n_{tot,T=0} \approx 1.1, 0.7, 0.5 \times 10^{11} \text{ cm}^{-2}$ for Sample C. The quantity $n_{tot,T=0}$ refers to the total charge density induced by V_G and charged impurities (Eq. 4.2). We clearly observe that K_e increases with both n and T_e in both samples. For instance, K_e ranges from roughly 1 W/K.m at 60 K and $n = -8 \times 10^{10} \text{ cm}^{-2}$ to 5 W/K.m at 135 K and $n = -1.8 \times 10^{11} \text{ cm}^{-2}$ for Sample A. Error bars representing the uncertainty on the extracted K_e are shown in Fig. 4.4. For error analysis, we used the same method presented in section 3.3.1. To calculate the uncertainties on the values extracted for K_e , using Eq. 4.4, we account for four sources of uncertainty: error on the sample's length, $\Delta\ell$, width ΔW , resistance ΔR due to the contact resistance uncertainty ΔR_c , and extracted electronic temperature ΔT_e . We estimate $\Delta\ell =$ one mean free-path (extracted using Eq. 4.3) which ranges from 205 nm at 80 K ($V_G = -5.3$ V) to 158 nm at 150 K ($V_G = -2.3$ V) for Sample A and from 135 nm at 80 K ($V_G = +5.0$ V) to 87 nm at 150 K ($V_G = -2.0$ V) for sample C. $\Delta W \approx 50$ nm, $\Delta R = \Delta R_c = R_o/2 = 239$ and $406 \text{ } \Omega$ for Samples A and C, and $\Delta T_e =$ the standard deviation of T_e from the fit of T_e vs V_B as shown in Figs. 4.2(d) and 4.3(b).

The error on the measured current I is negligible compared to the other sources of error, and the thickness $h = 0.335$ nm is a standard value used by all experiments and theory. Note that $\Delta T = T_e - T$ where T is the cryostat temperature. The error on T is about 0.1 K and comes from the accuracy of our temperature controller, thus the error on ΔT is roughly $\Delta T_e + 0.1$ K. We calculate ΔK_e using equation:

$$\frac{\Delta K_e}{K_e} = \sqrt{\left(\frac{\Delta L}{L}\right)^2 + \left(\frac{\Delta W}{W}\right)^2 + \left(\frac{\Delta R}{R}\right)^2 + \left(\frac{\Delta(\Delta T)}{\Delta T}\right)^2} \quad (4.5)$$

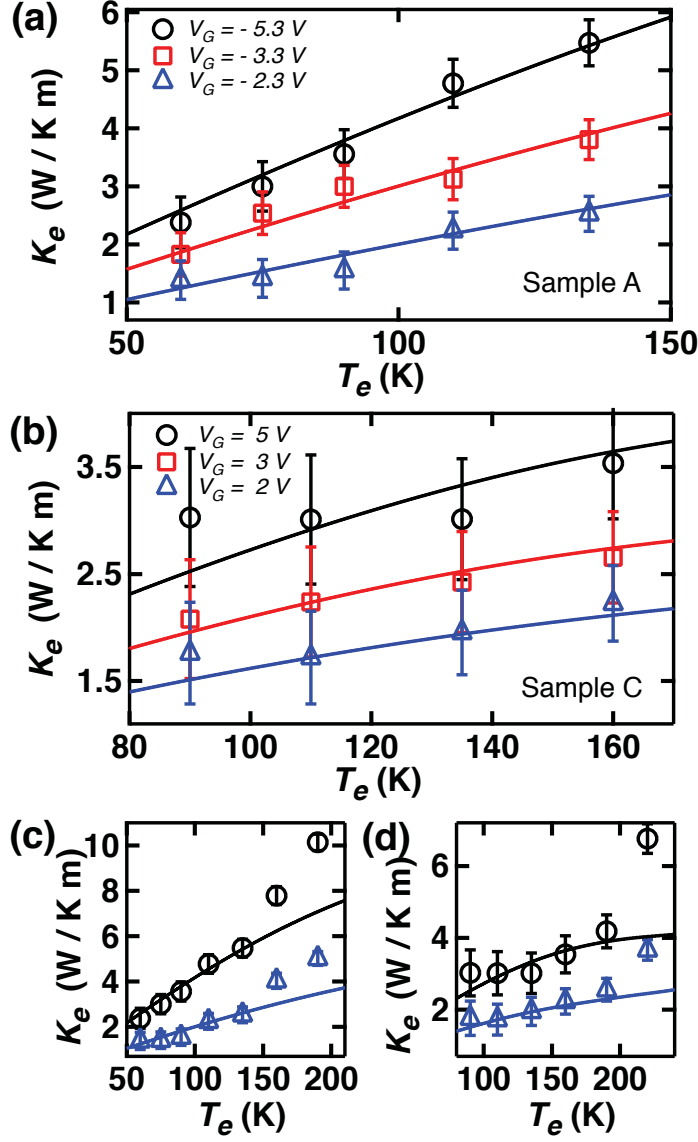


Figure 4.4: Wiedemann-Franz (WF) law. (a) The electronic thermal conductivity, K_e , of Sample A in the hole-doped regime versus T_e for $\Delta T = T_e - T = 10$ K. The circle, square and triangle data show K_e at $V_G = -5.3, -3.3$ and -2.3 V, respectively, corresponding to $n_{tot, T=0} \approx -1.8, -1.1, -0.8 \times 10^{11} \text{ cm}^{-2}$. The solid lines are given by the WF relation $K_{WF} = L\sigma T_e$ with $L = 0.45, 0.53$ and $0.55 \times L_o$ respectively. (b) K_e vs T_e for $\Delta T = 10$ K for Sample C in the electron-doped regime. The circle, square and triangle data show K_e at $V_G = 5, 3$ and 2 V corresponding to $n_{tot, T=0} \approx 1.1, 0.7, 0.5 \times 10^{11} \text{ cm}^{-2}$. The solid lines are the K_{WF} with $L = 0.66, 0.68, 0.7 \times L_o$. (c) and (d) show the same data as in (a) and (b) up to higher T_e where the apparent departure between the data and WF prediction is understood as the onset of electron-phonon coupling.

The calculated errors are shown in Figs. 4.4 and 4.6. For example, the error bars $\frac{\Delta K_e}{K_e}$ at $T = 100$ K are approximately 20% for Samples A and 40% for Sample C.

We confirmed that the V_B needed to create ΔT did not dope significantly the samples or affect the measured K_e . Using $n_{tot}(T)$ (Eq. 4.2) [14, 83], we define an effective chemical potential $\mu_{eff}(T) = \hbar v_F \sqrt{\pi n_{tot}(T)}$. For instance, for Sample A at $V_G = -5.3$ V and $T = 100$ K, $\mu_{eff}(100\text{K}) = 49$ meV. The various V_B necessary to achieve $\Delta T \leq 10$ K in Fig. 4.4 are always significantly smaller than $\mu_{eff}(T)$ and never larger than 27 mV. We only observe a change in the extracted K_e values (in the doped-regime) when ΔT exceeds 20 K, and $V_B > \mu_{eff}(T)$. The thermoelectric voltages in our devices are negligible compared to V_B [86, 87].

4.3 Theoretical Model: Wiedemann-Franz Law

We test the WF law ($K_e = \sigma L T_e$, where σ is the electrical conductivity, T_e is the electronic temperature and L is the Lorenz number) in our samples, which have a mobility of $\mu \approx 3.5 \times 10^4$ cm²/V.s, as a function of T_e and n . While the Lorenz number in most metals is close to $L_o = 2.44 \times 10^{-8}$ W Ω K⁻², it is well known that its value can be reduced in semiconductors at low charge density [94, 95]. The solid lines in Fig. 4.4 show K_{e-WF} given by the WF law using the measured σ and extracted T_e (Fig. 4.2), with L used as the single fitting parameter. The WF relation holds for both Samples at all T_e between 50 K and 160 K, and densities $n_h = -1.8$ to -0.8×10^{11} cm⁻² and $n_e = 0.5$ to 1.1×10^{11} cm⁻². For Sample A, $L = 0.45, 0.53$ and $0.55 \times L_o$, and for Sample C $L = 0.66, 0.68, 0.7 \times L_o$ (triangle, square, and circle data, respectively). The main uncertainty on L comes from the uncertainty on R_c , and corresponds to $\pm_{0.2}^{0.1} L_o$ for Sample A, and $\pm 0.4 L_o$ for Sample C. We note that the qualitative temperature and density dependence of the data in Fig. 4.4, and the agreement with the WF law, is preserved even if we use either the maximum $R_c = R_o$ or minimum $R_c = 120 \Omega$ (see section 4.3.1). The increase in L as n increases is consistent with previous studies in semiconductors where the value of L tends toward L_o at higher carrier density [95].

Electron to acoustic phonon coupling is very weak in clean graphene at moderate doping and temperature ($< 200 - 300$ K) [14, 16, 17, 24, 58], but increases at higher n

and T . In the context of our experiment, if the thermal energy conductance between electrons and phonons G_{e-p} is non-negligible compared to the electronic thermal conductance G_e , the heat conductivity we extract is a mixture of K_e and K_{e-p} in parallel. As can be seen in Fig. 4.4(c)-(d), above ≈ 160 K the extracted K no longer agrees with the WF prediction (solid line), indicating that we cannot isolate K_e for $T_e > 160$ K. Previously we found that we could extract K_e up to 300 K in samples whose n was very close to the CNP [14] (Chapter 3), suggesting that $e - p$ coupling is weaker at lower n as expected theoretically [58]. In Fig. 4.4(c)-(d), the departure between the K data and WF prediction starts around 150 K for Samples A and 200 K for Sample C. The different T ranges over which K_e dominates in the two devices comes from the ratio $G_e/G_{e-ph} = W/(W\ell) = 1/\ell$ which is 60 % larger for Sample C than Sample A.

4.3.1 Contact resistance effect on extracted Lorenz numbers

The uncertainty on the contact resistance does not significantly affect the accuracy of the agreement of the data in Fig. 4.4 of the main text with the Wiedemann-Franz relation. We used $R_c = R_o/2 = 239$ and $406 \text{ } \Omega$ for Samples A and C respectively in Fig. 4.4. Figures 4.5 and 4.4 show that the quality of the fit of the data to the WF law is not affected by the systematic uncertainty on R_c . The only effect of the R_c uncertainty is a quantitative change in the extracted Lorenz number L . Fig. 4.5(a) shows the WF law fit to the data if we let $R_c = R_{min} = 120 \text{ } \Omega$ (calculated using the lowest reported gold-graphene resistance [93] at similar densities), and Fig. 4.5(b) shows the WF law fit to the data if we let $R_c = R_{max} = 477 \text{ } \Omega$ (extracted in section 4.1.1)

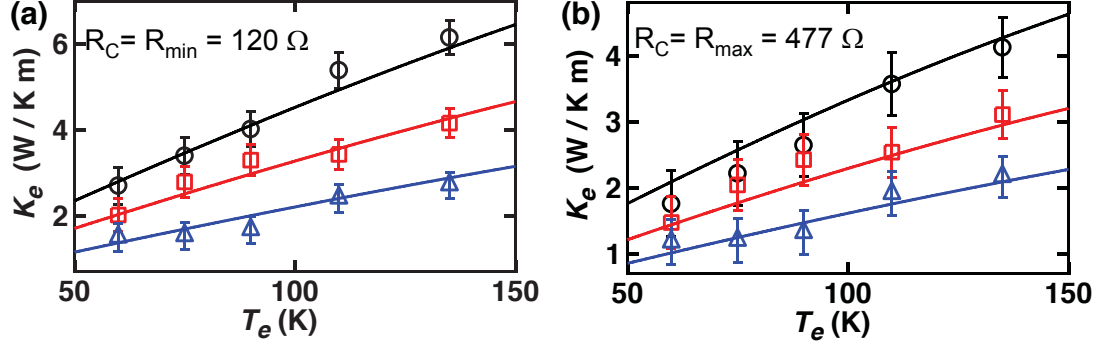


Figure 4.5: Effect of the contact resistance uncertainty on data in Fig. 4.4(a). The electronic thermal conductivity, K_e , of Sample A in the hole-doped regime vs T_e for $\Delta T = T_e - T = 10$ K. The circle, square and triangle data show K_e at $V_G = -5.3, -3.3$ and -2.3 V respectively corresponding to $n_{tot, T=0} \approx -1.8, -1.1, -0.8 \times 10^{11} \text{ cm}^{-2}$. (a) Using $R_c = R_{min} = 120 \Omega$. The solid lines are given by the WF relation $K_{WF} = L\sigma T_e$ with $L = 0.53, 0.64$ and $0.68 \times L_o$ respectively. (b) Using $R_c = R_{max} = 477 \Omega$. The solid lines are given by the WF relation with $L = 0.33 \times L_o$ for all three curves.

4.4 Thermal Transistor Effect in Graphene

Figure 4.6 shows the extracted K_e vs V_G at $T_e = T + \Delta T = 100 + 10$ K for Sample A (C) as solid red squares (black circles). For reference only, we also show two data points (open grey symbols) close to $V_G \approx 0$ which are taken from Ref. [14] for the same Samples. We cannot extract K_e at intermediate n , i.e. when $0.3 \text{ V} \leq |V_G| \leq 1.5 \text{ V}$. This is because while R smoothly increases with T_e in the metal-like regime (Fig. 4.2(a)), $|V_G| \geq 1.5 \text{ V}$, and smoothly decrease in the insulator-like regime [14], $|V_G| \leq 0.3 \text{ V}$, the R vs T_e behavior does not act as a good thermometer at intermediate densities. We also note that the WF relation we discuss in this work, $K_e = \sigma L T_e$, only applies in the degenerately doped regime where the Fermi energy $\mu \gg k_B T_e$, and we focus our discussion on this regime. The solid symbol data in Fig. 4.6 show that K_e is tuned by the charge carrier density in the samples. The solid lines are the WF values K_{e-WF} calculated using the measured σ , $T_e = 110$ K, and setting $L = 0.53$ and $0.67 L_o$ for Samples A and C. The agreement between the WF law and data in the doped regime is excellent. Even using a modest V_G range, K_e could be tuned by a factor of ≥ 2 in Fig. 4.6. This is a very strong thermal-transistor effect (with the caveat that $K_p \gg K_e$ [44, 51]). This could have applications in optoelectronics. A larger K_e

means that when a charge carrier is excited by a photon, it can travel a larger distance and excite additional carriers before it thermalizes with the lattice. Thus, more of the photon energy is harvested as electrical current [18]. Additionally, a tunable K_e implies a tunable C_e which could be used to optimize bolometric applications of graphene [45, 46].

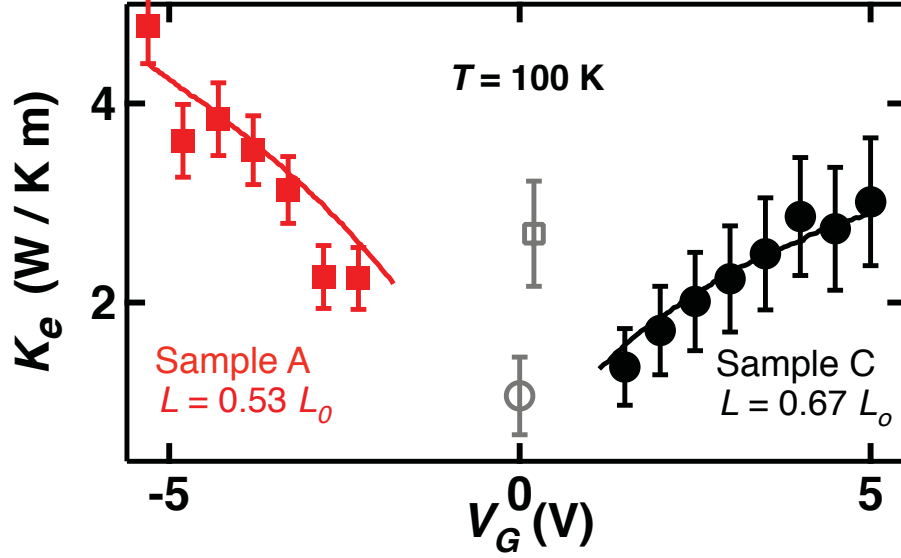


Figure 4.6: Electronic thermal conductivity transistor effect. K_e vs V_G data for Samples A (solid squares, $n < 0$) and C (solid circles, $n > 0$), for $T = 100$ K and $\Delta T = 10$ K. $V_G \approx 0$ data (open symbols, $\Delta T = 5$ K) are from Ref. [14]. The solid lines show K_{WF} predicted by the Wiedemann-Franz relation using a Lorenz number of $L = 0.53 L_0$ and $0.67 L_0$ for A and C respectively

4.5 Conclusion and Outlook

In summary, we fabricated high quality suspended graphene devices. We used a self-thermometry and self-heating method [14] to extract the electronic thermal conductivity in doped graphene. We report for the first time K_e in suspended graphene over a broad range of T and n . The data presented clearly demonstrates that $K_e \propto \sigma T$, which confirms that the Wiedemann-Franz law holds in high-mobility ($\mu \approx 3.5 \times 10^4 \text{ cm}^2/\text{V.s}$) suspended graphene over our accessible temperature range, 50 K - 160 K. This temperature range is limited at high-temperature by a turning on of the electron-phonon coupling, which prevents us from isolating K_e at higher T . The clear onsets of the electron-phonon coupling (Fig. 4.2(b), and 4.4(c)-(d)) between 150 K- 200 K is consistent with theoretical calculations [58]. We studied charge densities of holes and electrons ranging up to $1.8 \times 10^{11} \text{ cm}^{-2}$ and found Lorenz numbers $L \approx 0.5 - 0.7 L_o$, where L_o is the standard Lorenz number for metals. The quality of the agreement between the data and the WF relation in Figs. 4.4 and 4.6 is not affected by the uncertainty on the extracted Lorenz numbers (section 4.3.1). Finally, we demonstrated a strong thermal-transistor effect where we could tune K_e by more than a factor of 2 by applying only a few volts to a gate electrode.

In the future, these measurements could be extended to even cleaner devices at lower densities to study possible corrections to the generalized WF relation due to strong electron-electron interactions [88,89]. The demonstrated density control of K_e could be useful to make energy harvesting optoelectronic devices [16–18] and sensitive bolometers [45,46].

Chapter 5

Conclusion and Ongoing Projects

In this chapter, we will conclude the work presented in this thesis and discuss our results in the context of literature. We will also discuss the outlook of this work and an ongoing project about bilayer graphene. We will motivate this work and describe how we prepare bilayer graphene transistors. Finally, we will discuss the possible experiment ideas which could be explored with these devices.

5.1 Conclusion: Electronic Thermal Conductivity in Monolayer Graphene

In this thesis, we studied the electronic thermal conductivity, K_e , in monolayer graphene versus temperature and carrier density. We designed and fabricated high quality two-point suspended graphene transistors. We adopted a Joule self-heating and self-thermometry method, and extracted the electronic thermal conductivity from two-point charge transport measurements. We studied our samples at low bias voltages and intermediate temperatures where the electron-phonon energy transfer is negligible. Thus we could decouple the temperature of electrons from phonons and isolate K_e .

In chapter 1, we briefly introduced the electronic and thermal properties of graphene to give a background for the work presented in this thesis. We started by deriving the linear low-energy band structure and discussed its effect on the behaviour of charge carriers and the density of states. We also explained how we dope (p-type or n-type) and undope (intrinsic) graphene via electrical doping. Finally we reviewed the

thermal properties of graphene and proposed our work to measure electronic thermal conductivity in graphene.

In chapter 2, we explained how we fabricate two-point suspended graphene devices (Fig. 5.1(a)). We used standard micro fabrication methods to prepare our samples. We started with preparing the substrates and making graphene flakes using mechanical exfoliation method. We selected single layer graphene flakes and made electronic contacts on them using lithography techniques. We used wet etching method to suspend our devices above the substrate. This ensured that the graphene crystal is completely decoupled from the substrate, thus there will not be any interactions with the substrate phonons. Lastly, we presented the electrical circuit which we used to acquire data from our samples.

In chapter 3, we presented the electronic thermal conductivity measurements in intrinsic high-mobility graphene devices. First, we explained the electron thermometry technique in which we used graphene's resistance both as a heater and a thermometer. We measured two-point resistance of graphene versus temperature (Fig. 5.1(b)). This thermometry curve was then used to monitor temperature of electrons from the resistance. We applied Joule self-heating to increase the temperature of electrons (Fig. 5.1(c)). We solved one dimensional heat equation and extracted K_e .

We found that K_e has a strong temperature dependence in the nearly intrinsic regime ($n_{tot,T=0} \approx 1.7 - 2.1 \times 10^{10} \text{ cm}^{-2}$), ranging from 0.5 to 11 W/m.K over a temperature range 20 to 300 K (Fig. 5.1(d)). We compared our results with a model of diffusing quasiparticles which has the same mean free path and velocity as graphene's charge carriers. Our data had a very good agreement with the model, confirming that the heat is carried by diffusing Dirac quasiparticles. Our data proved that the main cooling mechanism in our intrinsic graphene devices is hot-electron diffusion to the leads.

In chapter 4, we reported K_e in our samples in the doped regime. We doped our samples using a back-gate electrode which results in a total carrier charge density of $\approx 0.5 - 1.8 \times 10^{11} \text{ cm}^{-2}$. We applied our well-calibrated self-heating and self-thermometry techniques and extract K_e in the hole and electron doped regimes over a temperature range of $T = 50 - 160 \text{ K}$. We extracted K_e in our devices and tested Wiedemann-Franz (WF), $K_e = \sigma L T_e$ where σ is the charge conductivity and L is the Lorenz number (Fig. 5.2(a)-(b)).

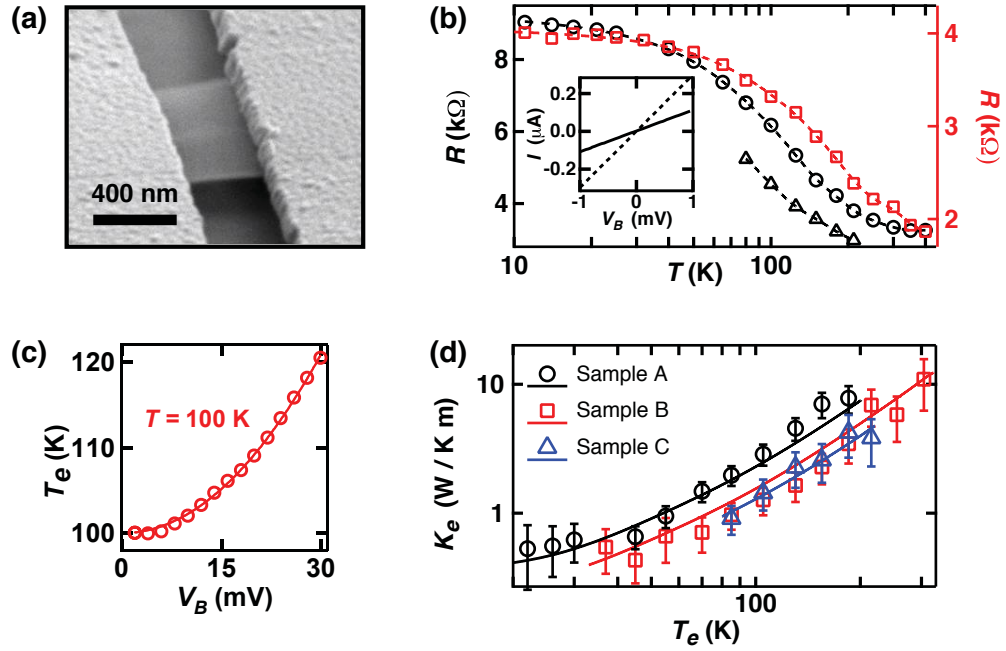


Figure 5.1: Summary of K_e in intrinsic graphene. (a) SEM image of a two-point suspended device. (b) Electron thermometry curve for Sample A (circles, left axis), Sample B (squares, right axis), and Sample C (triangles, left axis). Each resistance point is extracted from the slope of an $I - V_B$ curve like the one shown in the inset. (c) Joule self-heating at $T = 100$ K. (d) K_e versus T_e for Sample A, B and C.

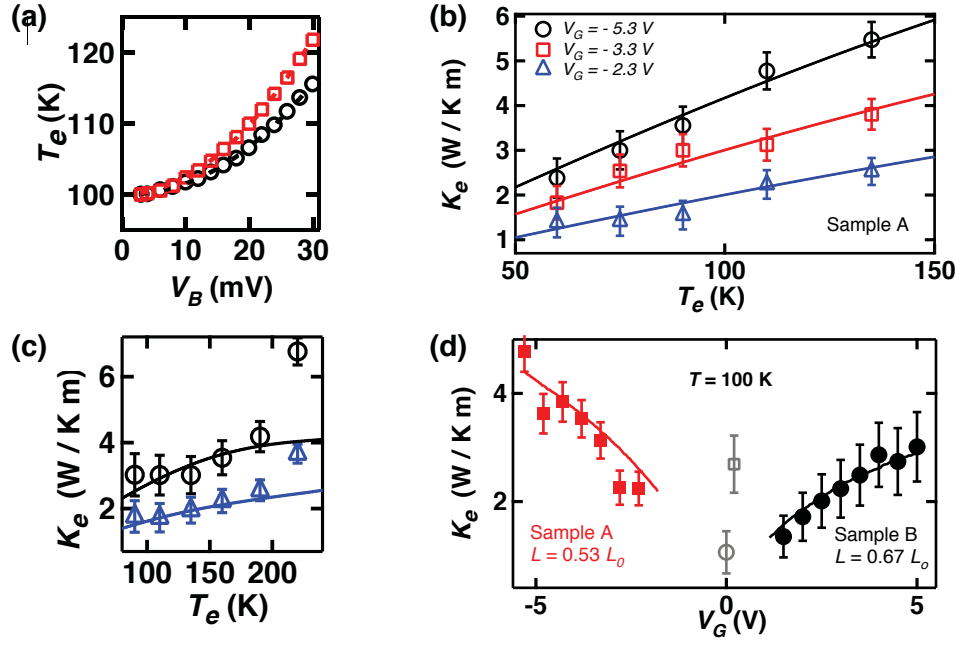


Figure 5.2: Summary of K_e in doped graphene. (a) Joule self-heating at $T = 100$ K and $V_G = -5.3$ V (circles), $V_G = -2.3$ V (squares). (b) K_e versus T_e in the hole-doped regime. Solid lines are given by the WF relation. (c) shows the same data as in (b) up to higher T_e where the departure between the data and WF prediction is understood as the onset of electron-phonon coupling. (d) K_e versus V_G for Sample A (solid squares, $n < 0$) and B (solid circles, $n > 0$). Open symbols data are at $V_G \approx 0$. Solid lines are given by WF relation.

We found that the measured K_e is in a very good agreement with the prediction of WF over the carrier density and temperature range studied. Our data showed that the WF law is obeyed in graphene. The value of L is $\approx 0.5 - 0.7 L_o$, where L_o is the Lorenz factor for metals. We observed an inconsistency between extracted K_e and the WF law above 160 K as expected due to the onset of strong coupling between electrons and acoustic phonons (Fig. 5.1(c)). Finally, we observed a strong thermal transistor effect where K_e could be tuned by more than a factor of 2 with a back-gate voltage, ranging up to ± 5 V (Fig. 5.1(d)).

In conclusion, our work gives a detailed mapping of K_e in graphene with respect to temperature and carrier density. Self-thermometry and Joule self-heating methods are proven to be efficient to study and isolate K_e in materials. Hence, the experimental technique used in this thesis offers a good base which can be extended to other two-dimensional materials.

5.2 Ongoing Projects: Bilayer Graphene

Graphene's perfect lattice and unusual band structure has quickly attracted tremendous attention within the scientific community. The simple scotch tape method made it possible to exfoliate two-dimensional (2D) graphene flakes from 3D graphite and to study them in bench-top experiments. The invention of this exfoliation method of graphene led to a new era in two-dimensional materials and opened up the possibilities to study other two-dimensional materials (boron nitride, topological insulators, etc..) as well as few-layer graphene.

Bilayer graphene, consisting two layers of graphene, is particularly of interest to scientists and engineers due its high quality electronic properties, mechanical strength and transparent nature [96, 97]. The low energy band structure of bilayer graphene is gapless as in monolayer graphene, but its low energy dispersion is quadratic. The charge carriers are no longer massless in bilayer graphene. Bilayer graphene offers the advantage of opening a band gap in its electronic dispersion through electrical or chemical doping. So far, it has been possible to open an energy band up to 300 meV [98–102]. This is an enormous advantage of bilayer devices over monolayer ones.

Bilayer graphene shares many similar properties with monolayer graphene as well. The mobility of charge carriers can reach as high as $40,000 \text{ cm}^2/\text{V.s}$ at room

temperatures, in air, on boron nitride substrates [90]. It has been shown that the total thermal conductivity of bilayer graphene is high and is dominated by phonons as in monolayer graphene. The room temperature thermal conductivity is measured to be about 2,800 W/K.m [44, 49]. Furthermore, bilayer graphene has remarkable mechanical strength and flexibility. Taking all these outstanding properties into consideration, bilayer graphene definitely has a huge potential for future applications like monolayer graphene. It could be applied in many areas including high-speed electronics, photonic devices, flexible touch screens, photodetectors, and energy storage applications.

There have been reports on the total or phonon thermal conductivity of bilayer graphene, yet no report of its electronic thermal conductivity, K_e . Electronic thermal conductivity measurements in bilayer graphene could help understand how much energy is carried by charge carriers. Also, it can help understanding the energy transfer between charge carriers and phonons in bilayer graphene, and how the charge carriers cool down. Managing and understanding how electrons carry energy in bilayer graphene would be very helpful for future nanoscale devices. To pursue K_e measurements in bilayers, we fabricate suspended two-point bilayer graphene transistors. We benefited from our experience and knowledge from monolayer graphene samples to build high-quality bilayer graphene devices.

In this section, we present the status of our ongoing bilayer graphene project. First, we will introduce the electronic band structure of bilayer graphene and derive the low energy dispersion relation of its charge carriers. Then we will describe the fabrication of our bilayer graphene devices and explain how we use Raman spectroscopy to identify the number of layers. Finally we will discuss the measurements we propose to make on the bilayer devices.

5.2.1 Electronic band structure

In this section, we briefly derive the electronic band structure of bilayer graphene from the tight-binding model [29, 103, 104]. Bilayer graphene is formed of two coupled monolayers of graphene where the carbon atoms are arranged in a honeycomb lattice (see Chapter 1). Figure 5.3 shows the crystal structure of bilayer graphene. The first layer is made up of atoms \tilde{A} (red) and \tilde{B} (black) and is drawn with solid lines. The second layer which is drawn with dashed lines, consists of atoms A (grey) and B

(white). This crystal configuration is called Bernal stacking (\tilde{A} - B) in which the atom \tilde{A} from the first layer and the atom B from the second layer overlay on each other. These atomic sites (\tilde{A} - B) are referred as dimers and the rest is called as non-dimer sites.

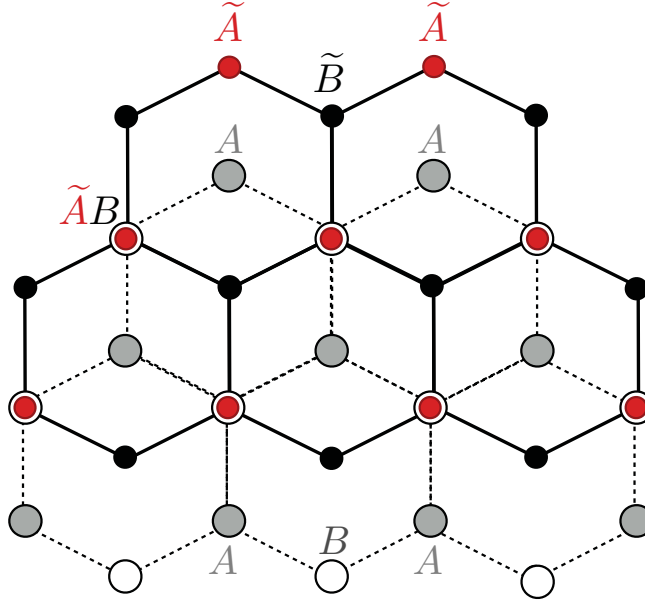


Figure 5.3: Crystal structure of bilayer graphene. The top layer is shown with solid lines and the atoms are labeled as \tilde{A} (red) and \tilde{B} (black). The bottom layer is drawn with dashed lines and the atoms are labeled as A (grey) and B (white). The atom \tilde{A} of upper layer and the atom B of bottom layer overlay on each other. These atomic sites (\tilde{A} - B) are referred as dimers and this crystal configuration is called Bernal stacking (\tilde{A} - B stacking).

Solving for the energy spectrum of electrons in bilayer (or few-layers) graphene is more complex than for monolayer graphene due to the stacking of layers. In the case of monolayer graphene, we only considered the hopping of electrons between nearest-atoms (γ_0 , $A \rightarrow B$). For bilayer graphene, we have to consider the hopping between the layers and as well as between adjacent atoms. Thus, we need to define the following tight-binding parameters to describe the hopping integrals:

$$\gamma_0 = -\langle \phi_A | \mathcal{H} | \phi_B \rangle = -\langle \phi_{\tilde{A}} | \mathcal{H} | \phi_{\tilde{B}} \rangle \quad (5.1)$$

$$\gamma_1 = \langle \phi_{\tilde{A}} | \mathcal{H} | \phi_B \rangle \quad (5.2)$$

$$\gamma_3 = -\langle \phi_A | \mathcal{H} | \phi_{\tilde{B}} \rangle \quad (5.3)$$

$$\gamma_4 = \langle \phi_A | \mathcal{H} | \phi_{\tilde{A}} \rangle = \langle \phi_B | \mathcal{H} | \phi_{\tilde{B}} \rangle \quad (5.4)$$

where \mathcal{H} is the Hamiltonian [29]. The parameter γ_1 describes the vertical hopping between the orbitals on the dimer sites (\tilde{A} - B), γ_3 describes the interlayer coupling between non-dimer sites (A - \tilde{B}) and γ_4 describes interlayer coupling between dimer and non-dimer orbitals (A - \tilde{A} or B - \tilde{B}). The transfer integral matrix for bilayer graphene can be written as

$$H = \begin{pmatrix} E_A & -\gamma_0 f(k) & \gamma_4 f(k) & -\gamma_3 f^*(k) \\ -\gamma_0 f^*(k) & E_B & \gamma_1 & \gamma_4 f(k) \\ \gamma_4 f^*(k) & \gamma_1 & E_{\tilde{A}} & -\gamma_0 f(k) \\ -\gamma_3 f(k) & \gamma_4 f^*(k) & -\gamma_0 f^*(k) & E_{\tilde{B}} \end{pmatrix} \quad (5.5)$$

where E_A , E_B , $E_{\tilde{A}}$ and $E_{\tilde{B}}$ are the on-site energies on the four atomic sites and the function $f(k)$ describes the nearest-neighbour hopping [29, 103] which was derived in Section 1.1 (Equation 1.13). This Hamiltonian gives rise to four valley-degenerate bands shown in Fig. 5.4, of which there are two valance and two conduction bands. One valance and one conduction band (V_1 and C_1) touch each other at zero energy whereas the other two (V_2 and C_2) are shifted away from the zero energy. This splitting energy is of the order of the interlayer coupling γ_1 and stems from the strong coupling of the orbitals on the dimer sites (\tilde{A} - B). The low-energy bands, on the other hand, arise from the hopping between the non-dimer sites. In intrinsic bilayer graphene, like in monolayer, the Fermi level sits at the zero energy where low-energy bands touch each other.

The energy spectrum of electrons can be determined by solving the eigenvalue equation, $H\Psi = E\Psi$. Defining an effective four-band Hamiltonian near the Dirac points, the four valley-degenerate energy bands can be determined as $E = \varepsilon_{\alpha}^{\pm}$, with $\alpha = 1, 2$. Energy ε_2 describes higher energy bands (V_2 - C_2). Energy ε_1 describes

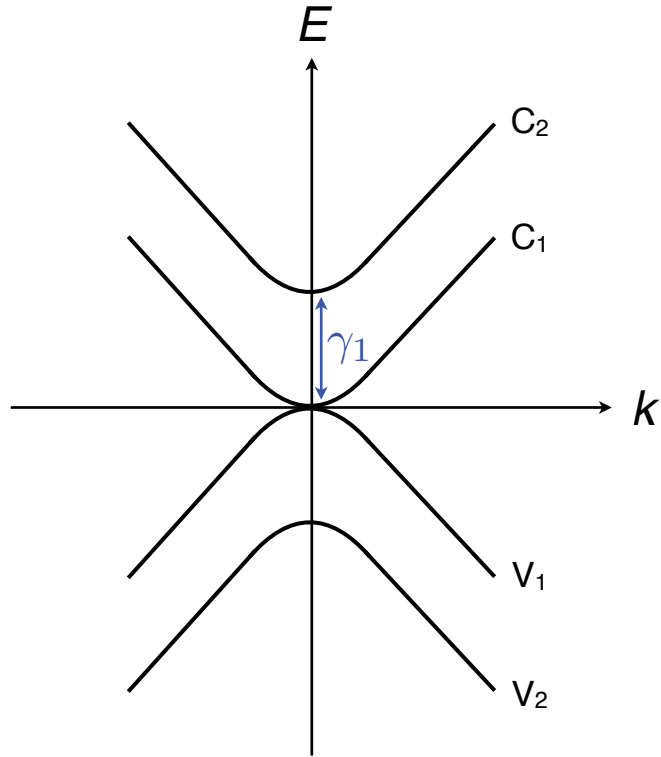


Figure 5.4: The low-energy electronic band structure of bilayer graphene. The lowest energy bands (V_1 and C_1) touch each other at zero energy and the higher energy bands (V_2 and C_2) are shifted away from the zero energy by the interlayer coupling γ_1 .

the low energy bands ($V_1 - C_1$) that are related to orbital on non-dimer sites. The low energy bands can be approximated as [29,104].

$$\varepsilon_1^\pm \approx \pm \frac{1}{2} \gamma_1 [\sqrt{1 + 4v^2 p^2 / \gamma_1^2} - 1] \quad (5.6)$$

At large momentum, it approximately reduces to linear dispersion, $\varepsilon_1 \approx vp$ and at small momentum it approximates to quadratic dispersion $\varepsilon_1 \approx p^2/2m$ where the mass is $m = \gamma_1/2v^2$.

5.2.2 Suspended bilayer graphene FETs

We fabricated suspended bilayer graphene field-effect transistors (FET) by following the fabrication procedure presented in Chapter 2. We used SiO_2 / Si wafers as substrate. The Si substrate will be used as back gate electrodes to control the charge carrier density, n_G . Bilayer graphene crystals are exfoliated on the substrate and preselected based on their optical contrast. Then their thicknesses are confirmed with Raman spectroscopy.

For the preselection of graphene flakes, we used an optical microscope under which the contrast of graphene flakes on silicon substrate can be observed. The most transparent flakes are grouped as monolayer graphene. The darker flakes are categorized depending on their contrasts. We use the optical images of previous samples, the thicknesses of which were confirmed with Raman Spectroscopy, as reference. This allows us to compare their contrasts and make more precise selection of flakes. Figure 5.5 shows optical images of monolayer, bilayer and trilayer graphene on SiO_2 substrate. Single layer graphene shown in panel (a) appears to be the most transparent. Bilayer graphene, in panel (b), has a darker contrast than single layers. In panel (c), trilayer graphene has an even darker contrast.

Even though the optical contrast method provides a good visual selection of graphene flakes, we still need to confirm our predictions. The most reliable way to distinguish the number of layers is to compare their Raman spectra. Using Raman spectroscopy, we can measure accurately the thickness of graphene crystals up to 6 layers. As the number of layer increases, there is a noticeable change in the shapes of 2D and G Raman peaks. Figure 5.6(a) shows the Raman spectrum of a single layer with G (blue) and 2D (red) Raman peaks. The G peak is located at $1583 \pm 3 \text{ cm}^{-1}$

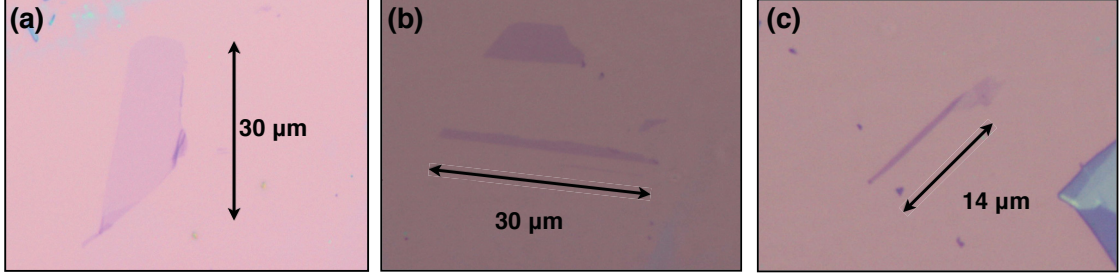


Figure 5.5: Optical images of (a) Monolayer, (b) Bilayer and (c) Trilayer graphene. The flakes appear to be darker as the number of layers increases.

and 2D peak is at $2681 \pm 3 \text{ cm}^{-1}$. Panel (b) shows the Raman spectrum of a bilayer graphene with G peak locating at $1583 \pm 3 \text{ cm}^{-1}$ and 2D peak locating at $2702 \pm 3 \text{ cm}^{-1}$. Panel (c) depicts the Raman spectrum of a trilayer graphene. The G peak is at $1583 \pm 3 \text{ cm}^{-1}$ and 2D peak is at $2712 \pm 3 \text{ cm}^{-1}$. The insets show the optical images of the flakes from which the data were acquired.

The Raman spectra shown in Figure 5.6 have apparent differences in the shape and height of their G and 2D bands which can give hints about the thickness of graphene. However, the most accurate way to confirm the number of layers is to compare the G/2D ratios. In table 5.1, we calculate the intensity ratio of height and area under the G and 2D bands of the Raman spectra presented in Fig. 5.6 and also give the positions of the center of 2D peaks which appear at different positions for single-layer, bilayer and trilayer graphene. As seen in the table, the position of 2D peaks shifts and the G/2D values differ as the number of layers increases. The integrated intensities (area under the peaks) are used as a reference to determine the number of layers [63]. Figure 5.7 shows the previously reported values for the integrated intensity ratios of G/2D bands as the number of layer increases (reproduced from reference [63]). Our values for the ratios of G/2D are consistent with the previous reported values [63,105].

After confirming that our flakes are bilayers using Raman spectroscopy, we build two-point transistors with them. We followed the fabrication process explained in Chapter 2. Fig 5.8 shows optical images of some of the bilayer devices we fabricated. We prepared devices with various length and widths. The width of the graphene flakes ranges from $0.5 \mu\text{m}$ to $2 \mu\text{m}$. The length of the graphene channel (between the contacts) ranges from $0.5 \mu\text{m}$ to $4 \mu\text{m}$. For devices longer than $1.5 \mu\text{m}$, we used

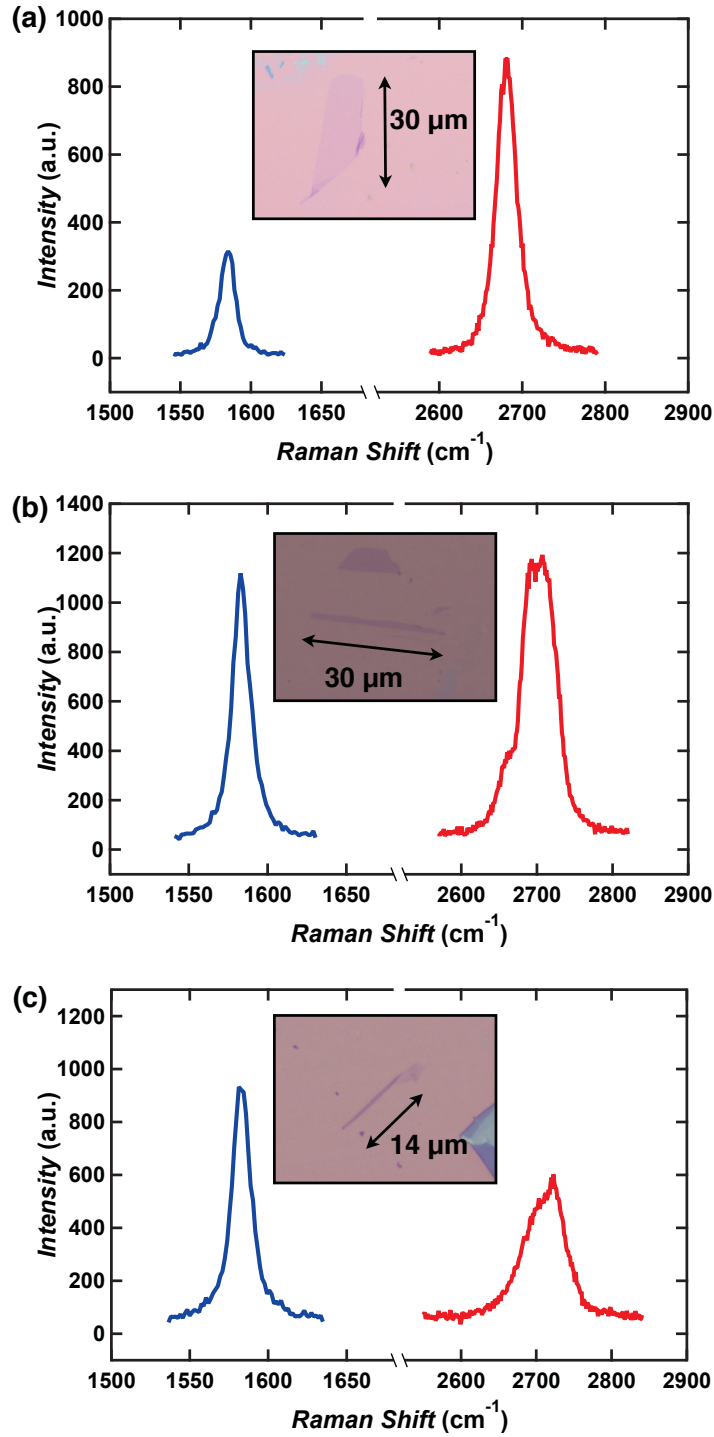


Figure 5.6: Raman spectroscopy of graphene flakes. (a) Raman spectrum of a single layer graphene flake showing G (blue) and 2D (red) Raman peaks. The inset shows an optical image of the flake. (b) Optical image and Raman spectrum of a bilayer graphene, showing G and 2D Raman peaks. (c) Optical image and raman spectrum of a trilayer graphene, showing G and 2D Raman peaks.

G/2D	Monolayer	Bilayer	Trilayer
Height	≈ 0.34	≈ 0.85	≈ 1.65
Area	≈ 0.19	≈ 0.4	≈ 0.5
Position (2D)	2681 cm^{-1}	2702 cm^{-1}	2712 cm^{-1}

Table 5.1: Comparison of G/2D intensity ratios for our single-layer, bilayer and trilayer graphene devices. These numbers are extracted from the Raman peaks shown in Fig. 5.6 by fitting with Lorentzian function and finding the height of the peaks and the area under the peaks. The last row presents the positions of the center of 2D peaks.

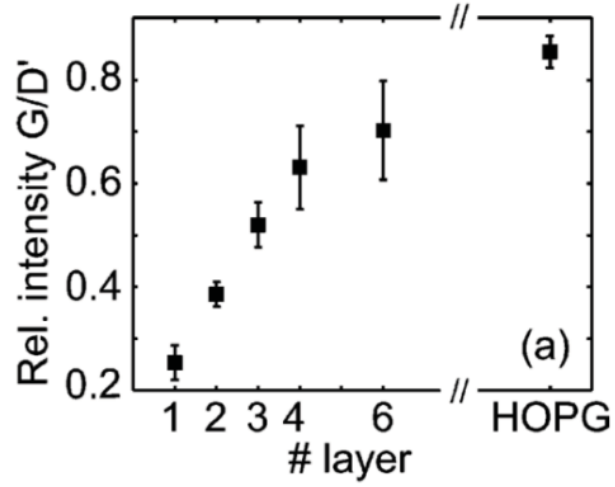


Figure 5.7: Integrated intensities (area) of Raman peaks of single and few layers graphene. Change in the ratio of the integrated intensities of G and 2D (D') peaks versus the number of layers. Reproduced from reference [63].

CPD (critical point dryer) to suspend. CPD reduces the surface tension of drying process during the wet etching. They are suspended to decouple the graphene crystals from the substrate. These samples are suitable for both electron and heat transport studies.

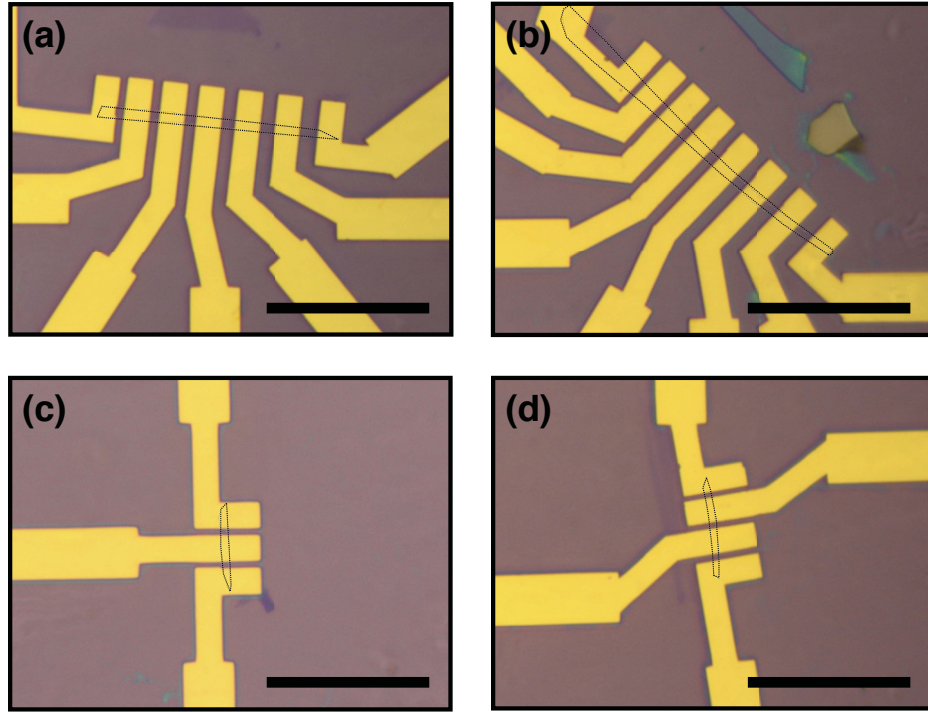


Figure 5.8: Optical images of the bilayer graphene samples. (a) A Sample with six 2-point devices. The length (the distance between the contacts) of the graphene channel ranges from $0.75\ \mu\text{m}$ to $2\ \mu\text{m}$. (b) A Sample with seven 2-point devices. The length of the devices ranges from $0.5\ \mu\text{m}$ to $2.25\ \mu\text{m}$. (c) A Sample with two 2-point devices. The length of devices is $1\ \mu\text{m}$. (d) A sample with three 2-point devices. The length of the devices is $1\ \mu\text{m}$. The dashed lines show the flakes lying underneath the contacts. The scale bar represents $20\ \mu\text{m}$.

5.2.3 Electronic thermal conductivity in bilayer graphene

Electronic thermal conductivity measurements would give information about how much energy is carried by charge carriers in bilayer graphene. Furthermore, it would help us understand electron-phonon interactions and electron cooling mechanisms in bilayer graphene. Understanding electron-phonon interaction is a significant step towards explaining many other physical processes in solids. For example, electron-phonon interaction can affect the electron transport, relaxation processes, electronic and phononic thermal conductivity, heat capacity, superconductivity and so on.

Bilayer graphene has been favoured to be used in applications thanks to the possibility of opening a band gap [98–102]. Because of this gap, bilayer graphene FETs can have a higher on/off ratio which can be up to 100 at room temperatures [97, 106, 107]. Studying the electronic thermal conductivity in bilayer graphene FETs can give us the knowledge necessary to control (via doping, strain, etc..) the amount of heat carried by the charge carriers which would be very helpful for developing novel applications in nano-electronics [108] and opto-electronics [97] such as bolometers [109, 110], photodetectors for terahertz detection [96, 111].

For our measurements, the suspension of the bilayer graphene channels will prevent any heat leakage to the substrate. Thus, the heat will only diffuse through the graphene crystal via scattering processes. The heat is transferred through electron-phonon scattering which is described by the following power law:

$$P = \Sigma (T_e^\delta - T_{ph}^\delta) \quad (5.7)$$

where Σ is the coupling constant, T_e is the electron temperature and T_{ph} is the phonon temperature [60, 112]. At intermediate temperatures, the thermal relaxation of hot-electrons through acoustic phonons [110] would be $P_{e-ac} \propto (T_e^4 - T_o^4)$ where T_o is the bath temperature, while the heat diffused by hot-electron scatterings is given by $P_{diff} \propto (T_e^2 - T_o^2)$ [60]. Therefore, at low enough temperatures and low bias, electron-phonon energy transfer in bilayer graphene should be small and the heat transport dominated by hot electrons diffusion [60, 109, 113]. In the high temperature regime and at high bias voltages, optical phonons will come into effect and electronic heat diffusion will be dominated by phonon scatterings ($P_{e-op} \propto T_e^2 - T_o^2$) [60, 112]. It was shown that electron-optical phonon scattering in bilayer graphene dominates at electronic temperatures of $T = 300 - 1000$ K [112]. Figure 5.9 shows a plot of

estimated P_{e-ph} in bilayer graphene as a function of electronic temperature T_e (for $n = 10^{11} \text{ cm}^{-2}$ and $T_{ph} = 0$), due to different phonon scattering processes (adapted from Reference [112]).

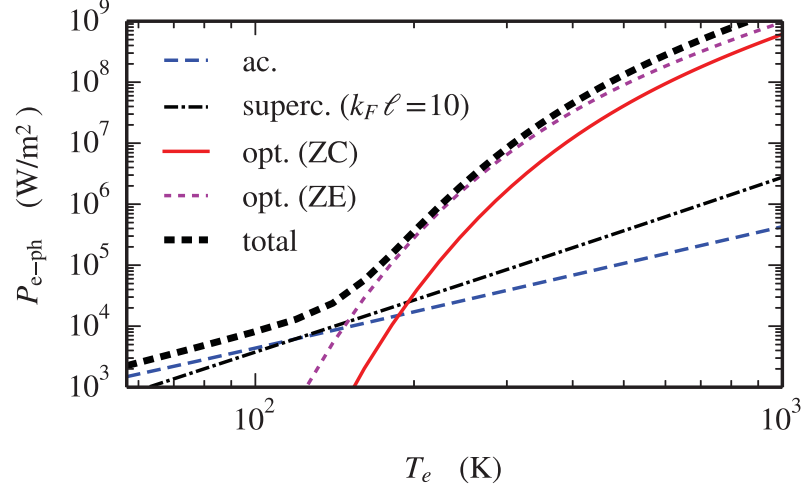


Figure 5.9: Expected P_{e-ph} in bilayer graphene versus electronic temperature T_e (for $n = 10^{11} \text{ cm}^{-2}$ and $T_{ph} = 0$), due to different phonon scattering processes (adapted from Reference [112]).

It is both experimentally and theoretically suggested that at intermediate temperatures and low bias voltage (corresponding to electronic temperatures of $< 300 \text{ K}$), electron-phonon energy transfer will be minimum. As a result, it should be possible to decouple the electron temperature (T_e) from the lattice temperature (T_{phonon}) in bilayer graphene and isolate the electronic thermal conductivity. Based on our work with monolayer graphene, we can propose that the electronic thermal conductivity can be isolated in our suspended bilayer graphene FETs by working at low bias voltages and temperatures ($< 300 \text{ K}$). Bilayer graphene FETs should be annealed to increase the mobility of charge carriers, however it should be left in the diffusive regime.

Another way to study K_e in bilayer graphene FETs would be ac measurements [114, 115]. If an alternating-current at an angular frequency ω , $I = I_0 \sin(\omega t)$, is applied to a material, an oscillating power will be created. The power at the same frequency, P_ω , is due to the Peltier effect and is called first harmonic. The power induced at frequency 2ω , $P_{2\omega}$, arises from the Joule heating and is called second

harmonic. From the second harmonic, the temperature rise $\Delta T_{2\omega}$ can be extracted.

These experiment can be extended to the Quantum Hall regime. By applying a perpendicular magnetic field to the devices, Quantum Hall Effects (QHE) in bilayer graphene can be observed [116, 117]. QHE experiments have been successful on bilayer graphene with similar two-point devices and found a temperature dependent differential conductance around the CNP at very low temperatures [118]. Therefore one can try to study K_e with our approach in the QHE regime. The contact resistance of the devices can be extracted by adapting the technique presented in the Ref. [118]. This work can help to understand how heat / energy is carried by the QHE edge states.

5.3 Contributions to Other Projects

I made contribution to other projects which resulted in two publications in peer-reviewed journals [119, 120]. In this section, we will briefly mention the results of these two projects.

5.3.1 Ultra-short suspended single-wall carbon nanotube transistors

We described a method to fabricate clean suspended single-wall carbon nanotube (SWCNT) transistors hosting a single quantum dot ranging in length from a few 10s of nm down to ≈ 3 nm. We first aligned narrow gold bow-tie junctions on top of individual SWCNTs and suspend the devices. We then used a feedback-controlled electromigration to break the gold junctions and expose nm-sized sections of SWCNTs. We measured electron transport in these devices at low temperature and showed that they form clean and tunable single-electron transistors. These ultra-short suspended transistors offer the prospect of studying THz oscillators with strong electron-vibron coupling.

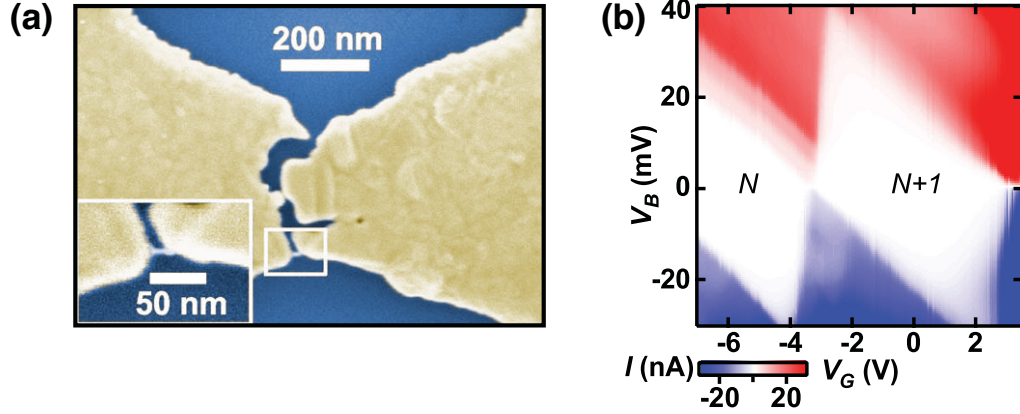


Figure 5.10: Ultra-short suspended single-wall carbon nanotube transistors. (a) Top view SEM image of SWCNT device after breaking. The inset shows a zoom-in on the 22 ± 5 nm-long SWCNT-QD. (b) $I - V_B - V_G$ data for SWCNT device. The data show clean SWCNT-QD [119].

5.3.2 Tailoring 10 nm scale suspended graphene junctions and quantum dots

The possibility to make 10 nm scale, and low-disorder, suspended graphene devices would open up many possibilities to study and make use of strongly coupled quantum electronics, quantum mechanics, and optics. We presented a versatile method, based on the electromigration of gold-on-graphene bow-tie bridges, to fabricate low-disorder suspended graphene junctions and quantum dots with lengths ranging from 6 nm up to 55 nm. We controlled the length of the junctions, and shape of their gold contacts by adjusting the power at which the electromigration process is allowed to avalanche. Using carefully engineered gold contacts and a nonuniform downward electrostatic force, we could controllably tear the width of suspended graphene channels from over 100 nm down to 27 nm. We demonstrated that this lateral confinement creates high-quality suspended quantum dots. This fabrication method could be extended to other two-dimensional materials.

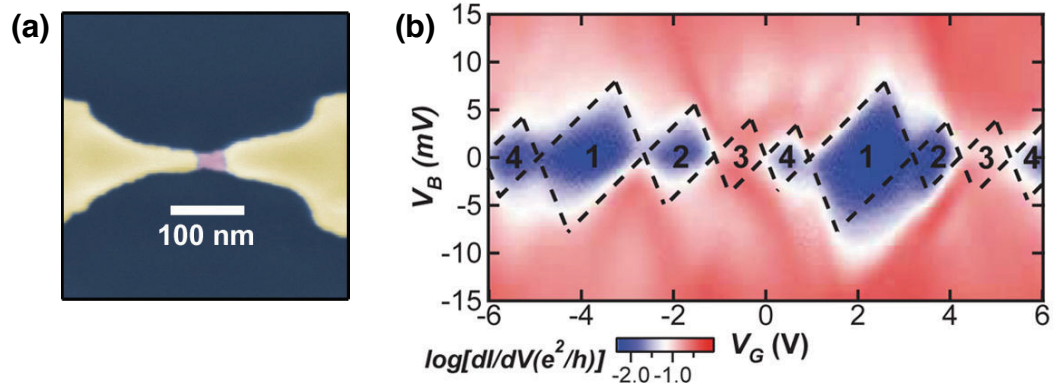


Figure 5.11: Tailoring 10 nm scale suspended graphene junctions and quantum dots. (a) Top view SEM image of a device whose graphene channel was cut down to the width of its sharp source contact. (b) $dI/dV - V_B - V_G$ data for the graphene junction depicted in (a). The dashed lines show Coulomb diamonds. The data indicates that there is a single QD in the channel [120].

Bibliography

- [1] K. S. Novoselov et al., *Electric field effect in atomically thin carbon films*, Science **306**, 666 (2004).
- [2] M. D. Stoller, S. J. Park, Y. W. Zhu, J. H. An, and R. S. Ruoff, *Graphene-Based Ultracapacitors*, Nano Lett. **8**, 3498 (2008).
- [3] P. Avouris, *Graphene: Electronic and Photonic Properties and Devices*, Nano. Lett. **10**, 4285 (2010).
- [4] F. Bonaccorso, Z. Sun, T. Hasan, and A. C. Ferrari, *Graphene photonics and optoelectronics*, Nature Photon. **4**, 611 (2010).
- [5] K. S. Novoselov et al., *A roadmap for graphene*, Nature **490**, 192 (2012).
- [6] X. J. Wan, Y. Huang, and Y. S. Chen, *Focusing on Energy and Optoelectronic Applications: A Journey for Graphene and Graphene Oxide at Large Scale*, Accounts Chem. Res. **45**, 598 (2012).
- [7] A. A. Balandin et al., *Superior Thermal Conductivity of Single-Layer Graphene*, Nano Lett. **8**, 902 (2008).
- [8] W. Cai et al., *Thermal Transport in Suspended and Supported Monolayer Graphene Grown by Chemical Vapor Deposition*, Nano Lett. **10**, 1645 (2010).
- [9] S. S. Chen et al., *Raman Measurements of Thermal Transport in Suspended Monolayer Graphene of Variable Sizes in Vacuum and Gaseous Environments*, ACS Nano **5**, 321 (2011).
- [10] C. Faugeras et al., *Thermal Conductivity of Graphene in Corbino Membrane Geometry*, ACS Nano **4**, 1889 (2010).

- [11] S. Ghosh et al., *Extremely high thermal conductivity of graphene: Prospects for thermal management applications in nanoelectronic circuits*, Appl. Phys. Lett. **92**, (2008).
- [12] L. A. Jauregui et al., *Thermal Transport in Graphene Nanostructures: Experiments and Simulations*, ECS Trans. **28**, 73 (2010).
- [13] D. L. Nika, S. Ghosh, E. P. Pokatilov, and A. A. Balandin, *Lattice thermal conductivity of graphene flakes: Comparison with bulk graphite*, Appl. Phys. Lett. **94**, (2009).
- [14] S. Yigen, V. Tayari, J. O. Island, J. M. Porter, and A. R. Champagne, *Electronic thermal conductivity measurements in intrinsic graphene*, Phys. Rev. B **87** (2013).
- [15] S. Yigen and A. R. Champagne, *Wiedemann-Franz Relation and Thermal-Transistor Effect in Suspended Graphene*, Nano Lett. **14**, 289 (2014).
- [16] N. M. Gabor et al., *Hot Carrier-Assisted Intrinsic Photoresponse in Graphene*, Science **334**, 648 (2011).
- [17] J. C. W. Song, M. S. Rudner, C. M. Marcus, and L. S. Levitov, *Hot Carrier Transport and Photocurrent Response in Graphene*, Nano Lett. **11**, 4688 (2011).
- [18] K. J. Tielrooij et al., *Photoexcitation cascade and multiple hot-carrier generation in graphene*, Nature Phys. **9**, 248 (2013).
- [19] M. Freitag et al., *Energy Dissipation in Graphene Field-Effect Transistors*, Nano Lett. **9**, 1883 (2009).
- [20] E. Pop, D. Mann, Q. Wang, K. E. Goodson, and H. J. Dai, *Thermal conductance of an individual single-wall carbon nanotube above room temperature*, Nano Lett. **6**, 96 (2006).
- [21] E. Pop, D. A. Mann, K. E. Goodson, and H. J. Dai, *Electrical and thermal transport in metallic single-wall carbon nanotubes on insulating substrates*, J. Appl. Phys. **101** (2007).

- [22] E. Pop et al., *Negative differential conductance and hot phonons in suspended nanotube molecular wires*, Phys. Rev. Lett. **95** (2005).
- [23] J. C. W. Song, M. Y. Reizer, and L. S. Levitov, *Disorder-Assisted Electron-Phonon Scattering and Cooling Pathways in Graphene*, Phys. Rev. Lett. **109**, 106602 (2012).
- [24] J. K. Viljas, A. Fay, M. Wiesner, and P. J. Hakonen, *Self-heating and nonlinear current-voltage characteristics in bilayer graphene*, Phys. Rev. B **83**, 205421 (2011).
- [25] S. Das Sarma and E. H. Hwang, *Density dependent electrical conductivity in suspended graphene: Approaching the Dirac point in transport*, Phys. Rev. B **87**, 035415 (2013).
- [26] D.-e. Jiang and Z. Chen, *Graphene Chemistry: Theoretical Perspectives*, John Wiley & Sons, 2013.
- [27] M. J. Allen, V. C. Tung, and R. B. Kaner, *Honeycomb Carbon: A Review of Graphene*, Chem. Rev. **110**, 132 (2010).
- [28] A. Jorio, M. S. Dresselhaus, R. Saito, and G. Dresselhaus, *Raman spectroscopy in graphene related systems*, John Wiley & Sons, 2010.
- [29] E. McCann and M. Koshino, *The electronic properties of bilayer graphene*, Rep. Prog. Phys. **76** (2013).
- [30] A. H. Castro Neto, F. Guinea, N. M. R. Peres, K. S. Novoselov, and A. K. Geim, *The electronic properties of graphene*, Rev. Mod. Phys. **81**, 109 (2009).
- [31] P. R. Wallace, *The Band Theory of Graphite*, Phys. Rev. **71**, 622 (1947).
- [32] J. W. McClure, *Band Structure of Graphite and de Haas-van Alphen Effect*, Phys. Rev. **108**, 612 (1957).
- [33] J. C. Slonczewski and P. R. Weiss, *Band Structure of Graphite*, Phys. Rev. **109**, 272 (1958).
- [34] D. C. Elias et al., *Dirac cones reshaped by interaction effects in suspended graphene*, Nature Phys. **7**, 701 (2011).

- [35] S. Das Sarma, S. Adam, E. H. Hwang, and E. Rossi, *Electronic transport in two-dimensional graphene*, Rev. Mod. Phys. **83**, 407 (2011).
- [36] T. Ando, A. B. Fowler, and F. Stern, *Electronic-Properties of Two-Dimensional Systems*, Rev. Mod. Phys. **54**, 437 (1982).
- [37] K. S. Novoselov et al., *Two-dimensional gas of massless Dirac fermions in graphene*, Nature **438**, 197 (2005).
- [38] A. K. Geim and K. S. Novoselov, *The rise of graphene*, Nature Mater. **6**, 183 (2007).
- [39] Y. W. Tan et al., *Measurement of scattering rate and minimum conductivity in graphene*, Phys. Rev. Lett. **99** (2007).
- [40] K. I. Bolotin et al., *Ultrahigh electron mobility in suspended graphene*, Solid State Commun. **146**, 351 (2008).
- [41] K. I. Bolotin, K. J. Sikes, J. Hone, H. L. Stormer, and P. Kim, *Temperature-dependent transport in suspended graphene*, Phys. Rev. Lett. **101** (2008).
- [42] E. V. Castro et al., *Limits on Charge Carrier Mobility in Suspended Graphene due to Flexural Phonons*, Phys. Rev. Lett. **105** (2010).
- [43] R. Franz and G. Wiedemann, *Ueber die Wrme-Leitungsfhigkeit der Metalle*, Annalen der Physik **165**, 497 (1853).
- [44] A. A. Balandin, *Thermal properties of graphene and nanostructured carbon materials*, Nature Mater. **10**, 569 (2011).
- [45] K. C. Fong and K. C. Schwab, *Ultrasensitive and Wide-Bandwidth Thermal Measurements of Graphene at Low Temperatures*, Phys. Rev. X **2** (2012).
- [46] K. C. Fong et al., *Measurement of the Electronic Thermal Conductance Channels and Heat Capacity of Graphene at Low Temperature*, Phys. Rev. X **3** (2013).
- [47] D. L. Nika, E. P. Pokatilov, A. S. Askerov, and A. A. Balandin, *Phonon thermal conduction in graphene: Role of Umklapp and edge roughness scattering*, Phys. Rev. B **79**, 155413 (2009).

- [48] S. Ghosh, D. L. Nika, E. P. Pokatilov, and A. A. Balandin, *Heat conduction in graphene: experimental study and theoretical interpretation*, New J. Phys. **11** (2009).
- [49] S. Ghosh et al., *Dimensional crossover of thermal transport in few-layer graphene*, Nature Mater. **9**, 555 (2010).
- [50] J. U. Lee, D. Yoon, H. Kim, S. W. Lee, and H. Cheong, *Thermal conductivity of suspended pristine graphene measured by Raman spectroscopy*, Phys. Rev. B **83** (2011).
- [51] E. Pop, V. Varshney, and A. K. Roy, *Thermal properties of graphene: Fundamentals and applications*, MRS Bulletin **37**, 1273 (2012).
- [52] L. Shi et al., *Measuring thermal and thermoelectric properties of one-dimensional nanostructures using a microfabricated device*, J. Heat Trans-T Asme **125**, 1209 (2003).
- [53] W. Y. Jang, Z. Chen, W. Z. Bao, C. N. Lau, and C. Dames, *Thickness-Dependent Thermal Conductivity of Encased Graphene and Ultrathin Graphite*, Nano Lett. **10**, 3909 (2010).
- [54] J. H. Seol et al., *Two-Dimensional Phonon Transport in Supported Graphene*, Science **328**, 213 (2010).
- [55] Z. Q. Wang et al., *Thermal Transport in Suspended and Supported Few-Layer Graphene*, Nano Lett. **11**, 113 (2011).
- [56] X. Xu et al., *Length-dependent thermal conductivity in suspended single-layer graphene*, Nature Commun. **5** (2014).
- [57] R. Bistritzer and A. H. MacDonald, *Electronic Cooling in Graphene*, Phys. Rev. Lett. **102**, 206410 (2009).
- [58] S. Das Sarma and E. H. Hwang, *Density-dependent electrical conductivity in suspended graphene: Approaching the Dirac point in transport*, Phys. Rev. B **87** (2013).

- [59] J. Crossno, X. M. Liu, T. A. Ohki, P. Kim, and K. C. Fong, *Development of high frequency and wide bandwidth Johnson noise thermometry*, Appl. Phys. Lett. **106** (2015).
- [60] J. K. Viljas and T. T. Heikkila, *Electron-phonon heat transfer in monolayer and bilayer graphene*, Phys. Rev. B **81** (2010).
- [61] K. S. Novoselov et al., *Two-dimensional atomic crystals*, Proc. Natl. Acad. Sci. USA **102**, 10451 (2005).
- [62] A. C. Ferrari et al., *Raman spectrum of graphene and graphene layers*, Phys. Rev. Lett. **97** (2006).
- [63] D. Graf et al., *Spatially resolved raman spectroscopy of single- and few-layer graphene*, Nano Lett. **7**, 238 (2007).
- [64] A. C. Ferrari and D. M. Basko, *Raman spectroscopy as a versatile tool for studying the properties of graphene*, Nature Nanotech. **8**, 235 (2013).
- [65] M. S. Dresselhaus, A. Jorio, M. Hofmann, G. Dresselhaus, and R. Saito, *Perspectives on Carbon Nanotubes and Graphene Raman Spectroscopy*, Nano Lett. **10**, 751 (2010).
- [66] O. Frank et al., *Raman 2D-Band Splitting in Graphene: Theory and Experiment*, ACS Nano **5**, 2231 (2011).
- [67] A. Eckmann et al., *Probing the Nature of Defects in Graphene by Raman Spectroscopy*, Nano Lett. **12**, 3925 (2012).
- [68] S. Z. Butler et al., *Progress, Challenges, and Opportunities in Two-Dimensional Materials Beyond Graphene*, ACS Nano **7**, 2898 (2013).
- [69] W. K. Tse and S. Das Sarma, *Energy relaxation of hot Dirac fermions in graphene*, Phys. Rev. B **79**, 235406 (2009).
- [70] S. S. Kubakaddi, *Interaction of massless Dirac electrons with acoustic phonons in graphene at low temperatures*, Phys. Rev. B **79**, 075417 (2009).
- [71] S. Berciaud et al., *Electron and Optical Phonon Temperatures in Electrically Biased Graphene*, Phys. Rev. Lett. **104**, 227401 (2010).

- [72] D. K. Efetov and P. Kim, *Controlling Electron-Phonon Interactions in Graphene at Ultrahigh Carrier Densities*, Phys. Rev. Lett. **105**, 256805 (2010).
- [73] A. C. Betz et al., *Hot Electron Cooling by Acoustic Phonons in Graphene*, Phys. Rev. Lett. **109**, 056805 (2012).
- [74] A. C. Betz et al., *Supercollision cooling in undoped graphene*, Nature Phys. **9**, 109 (2013).
- [75] M. W. Graham, S. F. Shi, D. C. Ralph, J. Park, and P. L. McEuen, *Photocurrent measurements of supercollision cooling in graphene*, Nature Phys. **9**, 103 (2013).
- [76] S. Das Sarma, S. Adam, E. H. Hwang, and E. Rossi, *Electronic transport in two-dimensional graphene*, Rev. Mod. Phys. **83**, 407 (2011).
- [77] K. Saito, J. Nakamura, and A. Natori, *Ballistic thermal conductance of a graphene sheet*, Phys. Rev. B **76**, 115409 (2007).
- [78] I. Jo et al., *Low-Frequency Acoustic Phonon Temperature Distribution in Electrically Biased Graphene*, Nano Lett. **11**, 85 (2011).
- [79] V. E. Dorgan, A. Behnam, H. J. Conley, K. I. Bolotin, and E. Pop, *High-Field Electrical and Thermal Transport in Suspended Graphene*, Nano Lett. **13**, 4581 (2013).
- [80] X. Du, I. Skachko, A. Barker, and E. Y. Andrei, *Approaching ballistic transport in suspended graphene*, Nature Nanotech. **3**, 491 (2008).
- [81] Y. K. Koh, M. H. Bae, D. G. Cahill, and E. Pop, *Heat Conduction across Monolayer and Few-Layer Graphenes*, Nano Lett. **10**, 4363 (2010).
- [82] M. Muller, M. Brauninger, and B. Trauzettel, *Temperature Dependence of the Conductivity of Ballistic Graphene*, Phys. Rev. Lett. **103**, 196801 (2009).
- [83] V. E. Dorgan, M. H. Bae, and E. Pop, *Mobility and saturation velocity in graphene on SiO₂*, Appl. Phys. Lett. **97**, 082112 (2010).
- [84] N. Vandecasteele, A. Barreiro, M. Lazzeri, A. Bachtold, and F. Mauri, *Current-voltage characteristics of graphene devices: Interplay between Zener-Klein tunneling and defects*, Phys. Rev. B **82**, 045416 (2010).

- [85] Q. Li and S. Das Sarma, *Finite temperature inelastic mean free path and quasiparticle lifetime in graphene*, Phys. Rev. B **87**, 085406 (2013).
- [86] Y. M. Zuev, W. Chang, and P. Kim, *Thermoelectric and Magnetothermoelectric Transport Measurements of Graphene*, Phys. Rev. Lett. **102** (2009).
- [87] E. H. Hwang, E. Rossi, and S. Das Sarma, *Theory of thermopower in two-dimensional graphene*, Phys. Rev. B **80** (2009).
- [88] M. Muller, L. Fritz, and S. Sachdev, *Quantum-critical relativistic magnetotransport in graphene*, Phys. Rev. B **78** (2008).
- [89] M. S. Foster and I. L. Aleiner, *Slow imbalance relaxation and thermoelectric transport in graphene*, Phys. Rev. B **79** (2009).
- [90] C. R. Dean et al., *Boron nitride substrates for high-quality graphene electronics*, Nature Nanotech. **5**, 722 (2010).
- [91] S. Heinze et al., *Carbon nanotubes as Schottky barrier transistors*, Phys. Rev. Lett. **89** (2002).
- [92] G. Giovannetti et al., *Doping graphene with metal contacts*, Phys. Rev. Lett. **101** (2008).
- [93] R. Ifuku, K. Nagashio, T. Nishimura, and A. Toriumi, *The density of states of graphene underneath a metal electrode and its correlation with the contact resistivity*, Appl. Phys. Lett. **103** (2013).
- [94] Z. Bian et al., *Cross-plane Seebeck coefficient and Lorenz number in superlattices*, Phys. Rev. B **76** (2007).
- [95] A. J. Minnich, M. S. Dresselhaus, Z. F. Ren, and G. Chen, *Bulk nanostructured thermoelectric materials: current research and future prospects*, Energy Environ. Sci. **2**, 466 (2009).
- [96] D. Spirito et al., *High performance bilayer-graphene terahertz detectors*, Appl. Phys. Lett. **104** (2014).
- [97] F. N. Xia, T. Mueller, Y. M. Lin, A. Valdes-Garcia, and P. Avouris, *Ultrafast graphene photodetector*, Nature Nanotech. **4**, 839 (2009).

- [98] T. Ohta, A. Bostwick, T. Seyller, K. Horn, and E. Rotenberg, *Controlling the electronic structure of bilayer graphene*, Science **313**, 951 (2006).
- [99] Y. B. Zhang et al., *Direct observation of a widely tunable bandgap in bilayer graphene*, Nature **459**, 820 (2009).
- [100] E. McCann, *Asymmetry gap in the electronic band structure of bilayer graphene*, Phys. Rev. B **74** (2006).
- [101] H. K. Min, B. Sahu, S. K. Banerjee, and A. H. MacDonald, *Ab initio theory of gate induced gaps in graphene bilayers*, Phys. Rev. B **75** (2007).
- [102] E. V. Castro et al., *Biased bilayer graphene: Semiconductor with a gap tunable by the electric field effect*, Phys. Rev. Lett. **99** (2007).
- [103] M. Mucha-Kruczynski, *Theory of Bilayer Graphene Spectroscopy*, Springer, 2012.
- [104] E. McCann and V. I. Fal'ko, *Landau-level degeneracy and quantum hall effect in a graphite bilayer*, Phys. Rev. Lett. **96** (2006).
- [105] A. Gupta, G. Chen, P. Joshi, S. Tadigadapa, and P. C. Eklund, *Raman scattering from high-frequency phonons in supported n-graphene layer films*, Nano Lett. **6**, 2667 (2006).
- [106] B. N. Szafranek, D. Schall, M. Otto, D. Neumaier, and H. Kurz, *High On/Off Ratios in Bilayer Graphene Field Effect Transistors Realized by Surface Dopants*, Nano Lett. **11**, 2640 (2011).
- [107] B. N. Szafranek, D. Schall, M. Otto, D. Neumaier, and H. Kurz, *Electrical observation of a tunable band gap in bilayer graphene nanoribbons at room temperature*, Appl. Phys. Lett. **96** (2010).
- [108] F. Schwierz, *Graphene transistors*, Nature Nanotech. **5**, 487 (2010).
- [109] J. Yan et al., *Dual-gated bilayer graphene hot-electron bolometer*, Nature Nanotech. **7**, 472 (2012).
- [110] M. H. Kim et al., *Photothermal Response in Dual-Gated Bilayer Graphene*, Phys. Rev. Lett. **110** (2013).

- [111] V. Ryzhii and M. Ryzhii, *Graphene bilayer field-effect phototransistor for terahertz and infrared detection*, Phys. Rev. B **79** (2009).
- [112] A. Laitinen et al., *Electron-optical phonon coupling in suspended bilayer graphene*, arXiv:1409.6140 (2014).
- [113] S. V. Morozov et al., *Giant intrinsic carrier mobilities in graphene and its bilayer*, Phys. Rev. Lett. **100** (2008).
- [114] X. Cai et al., *Sensitive room-temperature terahertz detection via the photothermoelectric effect in graphene*, Nature Nanotech. **9**, 814 (2014).
- [115] K. L. Grosse, E. Pop, and W. P. King, *Heterogeneous nanometer-scale Joule and Peltier effects in sub-25 nm thin phase change memory devices*, J. Appl. Phys. **116**, (2014).
- [116] A. Kou et al., *Electron-hole asymmetric integer and fractional quantum Hall effect in bilayer graphene*, Science **345**, 55 (2014).
- [117] V. I. Fal'ko, *Electronic properties and the quantum Hall effect in bilayer graphene*, Phil. Trans. R. Soc. A **366**, 205 (2008).
- [118] F. Freitag, J. Trbovic, M. Weiss, and C. Schonenberger, *Spontaneously Gapped Ground State in Suspended Bilayer Graphene*, Phys. Rev. Lett. **108** (2012).
- [119] J. O. Island, V. Tayari, S. Yigen, A. C. McRae, and A. R. Champagne, *Ultra-short suspended single-wall carbon nanotube transistors*, Appl. Phys. Lett. **99** (2011).
- [120] V. Tayari et al., *Tailoring 10 nm Scale Suspended Graphene Junctions and Quantum Dots*, Nano Lett. **15**, 114 (2014).